Title

Exploring the geometry of circumnuclear material in active galactic nuclei through X-ray spectroscopy

Author
Rivers, Elizabeth Scirocco

Publication Date
2012

Peer reviewed|Thesis/dissertation

UNIVERSITY OF CALIFORNIA, SAN DIEGO

Exploring the Geometry of Circumnuclear Material in Active Galactic Nuclei through X-ray Spectroscopy

A dissertation submitted in partial satisfaction of the
requirements for the degree
Doctor of Philosophy

in

Physics

by

Elizabeth Rivers

Committee in charge:

George Fuller, Chair
Richard Rothschild, Co-Chair
Kim Griest
Stefan Llewellyn Smith
Kevin Quest

2012

The dissertation of Elizabeth Rivers is approved, and it is acceptable in quality and form for publication on microfilm and electronically:

____

____

____

____
Co-Chair

____
Chair

University of California, San Diego

2012

TABLE OF CONTENTS

LIST OF FIGURES

LIST OF TABLES

ACKNOWLEDGEMENTS

I would like to thank the following people: Alex Markowitz for all his mentorship and hard work; Jörn Wilms and Katja Pottschmidt for invaluable advice; My office mates Slawo Suchy and Paul Hemphill for being my computer gurus and for being someone to laugh with; Mark Rafelski and Jonathon Whitmore for leading the way; Alex Diamond-Stanic and Alison Coil for being excellent role models; Mike Gollner, Agnieszka Cieplak, and Kevin and Tali Ball for moral support and the occasional (okay frequent) rides to the airport; Mom, Dad, Malia, and the rest of my family for setting me on this path and encouraging me the whole way; Chuck for the flowers and the pancakes and for making the whole thing bearable; And last, but not least, thank you Rick, for being the most understanding and patient advisor I could have asked for.

Chapter 2, in part, is a reproduction of material as it appears in the Astrophysical Journal, Rivers, Markowitz & Rothschild, ApJ, 2011a, and Rivers, Markowitz, Duro & Rothschild, ApJ, 2012; and in part has been submitted for publication to the Astrophysical Journal 2012, Rivers, Markowitz & Rothschild. The dissertation author was the primary investigator and author of this material.

Chapter 3, in part, is a reproduction of material as it appears in the Astrophysical Journal 2011, Rivers, Markowitz & Rothschild, ApJ, 2011a; and, in part, has been submitted for publication to the Astrophysical Journal 2012, Rivers, Markowitz & Rothschild. The dissertation author was the primary investigator and author of this material.

Chapter 4, in full, is a reproduction of material as it appears in the Astrophysical Journal 2011, Rivers, Markowitz & Rothschild, ApJ, 2011c. The dissertation author was the primary investigator and author of this material.

Chapter 5, in full, is a reproduction of material as it appears in the Astrophysical Journal 2011, Rivers, Markowitz & Rothschild, ApJ, 2011b. The dissertation author was the primary investigator and author of this material.

Chapter 6, in full, is a reproduction of material as it appears in the Astrophysical Journal 2012, Rivers, Markowitz & Rothschild, ApJ, 2012. The dissertation author was the primary investigator and author of this material.

Chapter 7, in part, has been submitted for publication to the Astrophysical Journal 2012, Rivers, Markowitz & Rothschild. The dissertation author was the primary investigator and author of this material.

VITA

2007–2012	Ph. D. in Physics from University of California San Diego, CA
2007–2009	M.S. in Physics from University of California San Diego, CA
2003–2007	B.A. in Physics (*Major*) Studio Art (*Minor*) from Wellesley College, MA

PUBLICATIONS

Rivers, E., Markowitz, A. & Rothschild, R., *"16 Year RXTE Spectral Survey of X-ray Bright Active Galactic Nuclei"*, in preparation

Rivers, E., Markowitz, A., Duro, R., & Rothschild, R., *"A Suzaku Observation of Mkn 590 Reveals a Vanishing Soft Excess"*, ApJ, 2012, 759, 63

Rivers, E., Markowitz, A. & Rothschild, R., *"An Occultation Event in Centaurus A and the Clumpy Torus Model"*, 2011c, ApJ, 742, L29

Rivers, E., Markowitz, A. & Rothschild, R., *"A Suzaku Observation of MCG–2-58-22: Constraining the Geometry of the Circumnuclear Material"*, 2011b, ApJ, 732, 36

Rivers, E., Markowitz, A. & Rothschild, R., *"Spectral Survey of X-ray Bright Active Galactic Nuclei from the Rossi X-ray Timing Explorer"*, 2011a, ApJS 193, 3

Rivers, E., Markowitz, A., Pottschmidt, K., Roth, S., Barragan, L., Fürst, F., Suchy, S., Kreykenbohm, I., Wilms, J., Rothschild, R.E., *"A comprehensive spectral analysis of the X-ray pulsar 4U 1907+09 from two observations with the Suzaku X-ray observatory"*, 2010, ApJ, 709, 179

Mankuzhiyil, N., Ansoldi, S., Persic, M., Rivers, E., Rothschild, R., & Tavecchio, F., *"Emitting Electrons and Source Activity in Markarian 501"*, 2012, ApJ, 753, 154

Chatterjee, R., Marscher, A.P., Jorstad, S.G., Markowitz, A., Rivers, E., Rothschild, R.E., McHardy, I.M., and 9 coauthors *"Connection Between the Accretion Disk and Jet in the Radio Galaxy 3C 111"*, 2011, ApJ, 734, 43

Rothschild, R.E., Markowitz, A., Rivers, E., Suchy, S., Pottschmidt, K., Kadler, M., Mueller, C., Wilms, J., *"Twelve and a Half Years of Observations of Centaurus A with RXTE"*, 2011, ApJ, 733, 23

ABSTRACT OF THE DISSERTATION

Exploring the Geometry of Circumnuclear Material in Active Galactic Nuclei through X-ray Spectroscopy

by

Elizabeth Rivers

Doctor of Philosophy in Physics

University of California, San Diego, 2012

George Fuller, Chair
Richard Rothschild, Co-Chair

I have studied the X-ray spectral properties of active galactic nuclei (AGN) in order to gain a better understanding of the nature of the circumnuclear material surrounding the central black hole in these objects. From the *RXTE* archive I constructed two survey samples of broad band X-ray spectra. The first was a bright sample of 23 AGN that had high quality spectra up to at least 100 keV, which provided constraints on the high energy rollover expected by models of inverse Comptonization of low energy photons. The average lower limit to $E_{\rm roll}$ was $\sim$225 keV for the majority of objects, implying a coronal electron temperature of $k_{\rm B}T_{\rm e} \gtrsim 75$ keV for these models. The second sample was an expanded survey of

$\sim$100 AGN for which spectral parameters could be well-determined. I compared Fe line equivalent widths with measured Compton reflection hump strengths and found that on average $\sim$40% of the Fe line emission comes from reflection off Compton-thick material, with the remainder likely arising in isotropic emission from Compton-thin gas. In the full sample, the distributions of photon indices for Seyfert 1's and 2's were consistent with the idea that Seyferts share a common central engine, however the distributions of Compton reflection hump strengths did not support the classical picture of absorption by a torus and reflection off a Compton-thick disk with type depending only on inclination angle. I have concluded that a more complex reflecting geometry such as a combined disk and torus or clumpy torus is likely a more accurate picture of the Compton-thick material. I have performed additional analyses of individual objects. An occultation event in Cen A, discovered through *RXTE* monitoring, revealed the clumpy nature of its torus and placed constraints on the amount of material in the vicinity of the black hole in this object. A *Suzaku* long-look observation of MCG–2-58-22 provided constraints on the location of Fe line emitting material to $\gtrsim 1200\mathrm{R_S}$, likely associated with the torus which was successfully modeled by the MYTorus reflection model. A *Suzaku* observation of Mkn 590 revealed a disappearing soft excess, possibly providing evidence that the soft excess is associated with thermal disk emission.

1 Introduction

The largest black holes in the universe reside at the centers of galaxies. They are difficult to study directly and the precise nature and behavior of matter in and around such extreme gravitational conditions are still the subject of intense investigation at all wavelengths. When gas is pulled into the gravity well of these supermassive giants, it must release its gravitational energy and shed its angular momentum. Frictional heating of this material causes it to glow brighter and brighter, until it outshines all the stars in the galaxy combined. When this happens it is called an Active Galactic Nucleus or AGN.

The story of the discovery of AGN is not a straightforward one. AGN were first seen in 1908 but were not identified as part of a distinct class of galaxies until 1943 by Carl Seyfert. Quasars were discovered in the late 1950's with the advent of radio surveys, but were not connected with Seyfert galaxies for many years. The most defining property of all AGN is that a large amount of energy, the equivalent to several trillion stars, is produced in a very confined volume less than a cubic parsec. For quasars in particular, it was determined early on that the most viable explanation was that this energy must be gravitational in origin. However, this led to the issue that enough mass to power a quasar confined to only a few parsecs would collapse in on itself, as no known mechanism could provide enough outward pressure to maintain an object of such high density (Fowler & Hoyle 1963). This eventually led to the theory that all AGN, regardless of classification, must share a common central engine: an accreting supermassive black hole (SMBH) with a mass of around $10^6 - 10^8 M_\odot$ (Peterson 1997).

According to modern estimations, roughly one in ten galaxies host an AGN (Ho et al. 1997). There are many classes, types and sub-types of AGN. This is partly due to the wide variety of behaviors that have been observed in AGN, making it difficult to place them neatly into categories. The most general classes of AGN are quasars, blazars, radio galaxies, Seyfert galaxies, and low-luminosity AGN (LLAGN).

Seyferts, radio galaxies and quasars tend to be brightest in the optical to X-ray range, shown in Figure 1.1, and show a multitude of strong emission and absorption lines from circumnuclear material. Seyferts are some of the most common and well studied AGN with typical luminosities of $L \sim 10^{44} - 10^{46}$ erg s^{-1}. Radio galaxies show many properties similar to Seyferts, but are much brighter at radio wavelengths than typical Seyferts. Quasars are very bright, with luminosities $\gtrsim$100 times the luminosities of their host galaxies ($L \sim 10^{46}$ erg s^{-1}), and are generally believed to be exceptionally luminous versions of Seyferts and radio galaxies (Weedman 1976). LLAGN, on the other hand, are at the opposite end of the luminosity spectrum with typical bolometric luminosities of $\lesssim 10^{42}$ erg s^{-1}), and seem to be low-luminosity cousins of Seyferts and radio galaxies. Often all that can be seen of these objects are the strong emission lines rising above the spectrum of the host galaxy. In these cases they are referred to as LINERS.

Blazars are a special category of AGN which tend to have much higher luminosities both at radio energies and at energies greater than $\sim$ 1 MeV, and generally featureless (i.e., lacking emission lines) spectra with a characteristic double-hump spectral energy distribution (SED) profile as shown in Figure 1.2. Roughly 10% of AGN are categorized as blazars, either as flat spectrum radio quasars (FSRQs) or as BL Lac objects. To understand the properties of these different classes we need to first discuss the physical model of AGN accretion and radiative processes.

1.1 Anatomy of an AGN

AGN tend to be highly luminous across the entire electromagnetic spectrum, from radio to gamma-ray. This has helped astronomers disentangle and isolate different regions of the AGN by performing detailed studies at different wavelengths. For instance, radio emission seems to arise mainly in hot jets of

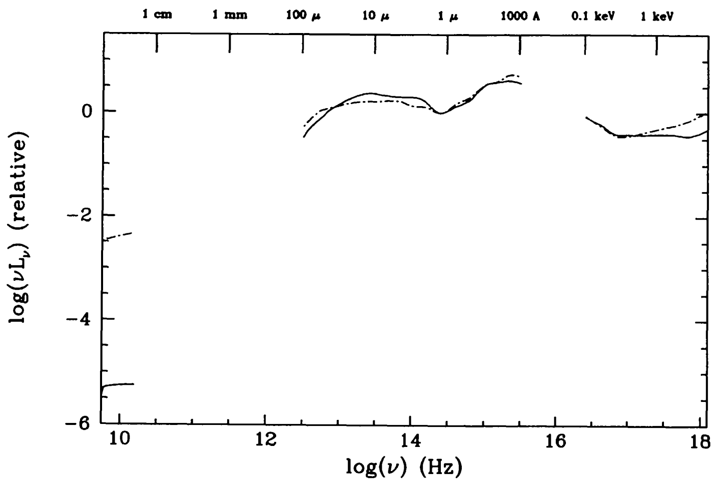

Figure 1.1: Mean SEDs for radio loud (*dotted line*) and radio quiet (*solid line*) quasars from Elvis et al. (1994).

plasma being ejected from the black hole out from the plane of the galaxy to distances of tens of Megaparsecs. Infrared emission comes from dust, and has been used to study the molecular torus surrounding the black hole. Optical and UV emission contains the "big blue bump" (BBB), which is thought to be thermal emission from an accretion disk, and Doppler-broadened optical lines, which are used for classifying different types of AGN. X-rays, which originate in a region very close to the central black hole, allow us to probe the inner parts of the accretion disk. Reprocessing of X-rays by by material surrounding the black hole can also give us vital information about the geometry and make-up of this circumnuclear material.

1.1.1 The Accretion Disk

It is believed that surrounding the SMBH, a compact disk of plasma rotates differentially, releasing gravitational energy through frictional heating in the

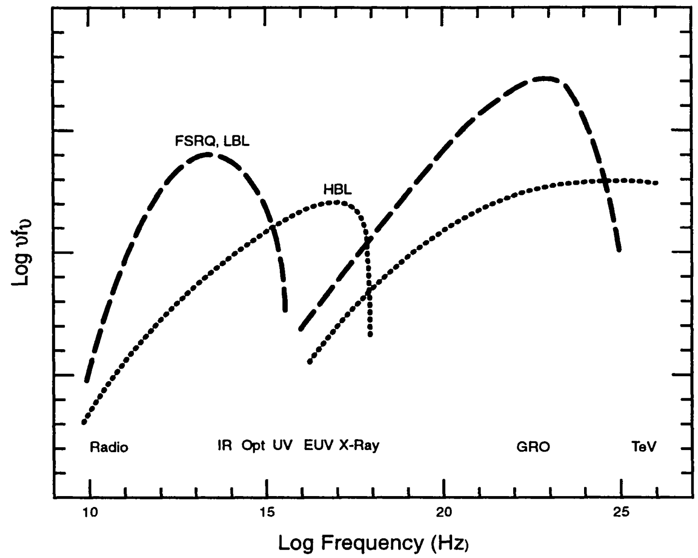

Figure 1.2: Characteristic double-humped blazar SEDs from Urry (1998). FSRQ and LBLs are flat spectrum radio quasars and low-frequency BL Lac objects, respectively, while HBLs are high-frequency BL Lac objects whose humps peak at higher energies. Note that LBLs tend to be intermediate between FSRQs and BL Lac objects.

viscous fluid. The commonly assumed geometrically thin (heigh $\ll$ radius), optically thick disk radiates as a multi-temperature black body (see, e.g., Kembhavi & Narlikar 1999). This theoretical model fits the observed BBB well, and it makes logical sense that the BBB, which contains a large fraction of the energy density being emitted, is a primary source of photons. The rapid flux variability of AGN on timescales of hours to days has led to the inference that the disk is likely not larger than a few light-hours; any larger and the variability would be smeared out on the observed timescales.

The accretion disk is thought to be present in all AGN, though in some cases the structure of the disk may differ. At very low accretion rates, such as those found in LLAGN, the disk may not form at all, instead matter may accrete in a spherically symmetric, radiatively inefficient manner. Advection dominated accretion flows (ADAFs) and thick disks (height $\sim$ radius) are another possible model and some disks may transition to this type of accretion at small radii. At very high accretion rates AGN approach their Eddington limit, the rate at which the pressure from infalling material is balanced by the outward radiation pressure. This limit is most often described by the Eddington luminosity ($L_{\rm Edd}$) for spherical accretion given by

$$L_{\rm Edd} = \frac{4\pi G c m_{\rm p}}{\sigma_{\rm T}} \times M_{\rm BH}, \tag{1.1}$$

where G is the gravitational constant, c is the speed of light, $m_{\rm p}$ is the mass of the proton, $\sigma_{\rm T}$ is the cross section for Thompson scattering, and $M_{\rm BH}$ is the mass of the black hole. Quasars are very bright, even for AGN, but while these objects may be accreting at high rates, they are likely not accreting close to their Eddington limits. Rather, it is believed that they are powered by more massive black holes ($\sim 10^8\ M_\odot$ or more).

1.1.2 The Broad and Narrow Emission Line Regions

Highly broadened optical lines are commonly seen in Seyferts and radio galaxies, and indicate the presence of material with orbital velocities exceeding $2000\ {\rm km\,s^{-1}}$. The broad line region (BLR), the region from which highly broadened optical lines arise, is thought to be clouds of material somewhere near the central source or perhaps even be part of the accretion disk itself. Khachikian & Weedman (1974) discovered that some Seyferts showed doppler broadened H emission lines in addition to narrow H emission lines while other Seyferts only had narrow lines in their optical spectra. They divided Seyferts into type 1 (with broad lines) and 2 (without broad lines). Seyfert 1/2 unification theories claim that this is because the BLR is obscured in Seyfert 2's while the narrow line region (NLR) is much further out and not subject to the same obscuration. This theory is supported by observations in optical spectra of some Seyfert 2's of polarized broad line emission scattered into the line of sight (e.g., Antonucci & Miller 1985).

Seyfert galaxies may be further broken down into sub-types based on ratios of broad to narrow line components in Hβ and Hα, and may be given a designation from 1 to 1.5 or from 1.8 to 2. Seyfert 1's are generally considered to encompass the former group while Seyfert 2's encompass the latter (although Seyfert 1.5's

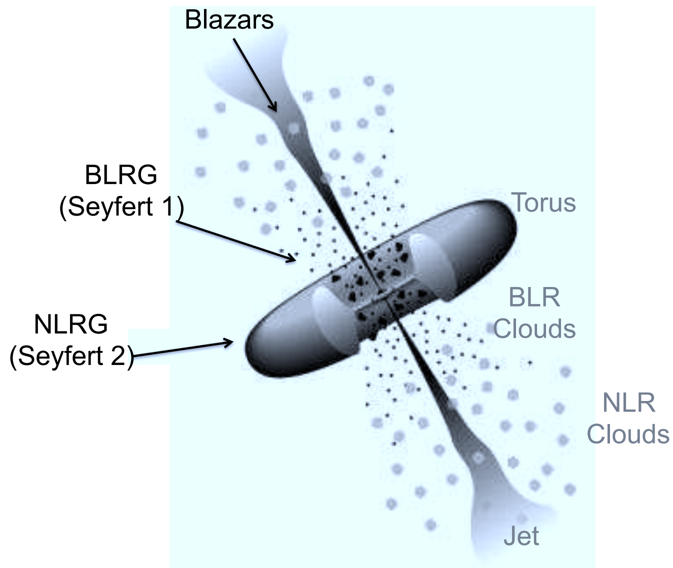

Figure 1.3: Unified AGN model from Urry & Padovani (1995) showing how viewing angle could determine AGN type.

are sometimes given their own designation of "intermediate" Seyferts). A special subset of Seyfert 1's are the so-called Narrow Line Seyfert 1's (NLSy1's), which display narrower broad emission lines than typical Seyfert 1's ($H\beta_{\rm FWHM} < 2000$ $\rm km\,s^{-1}$), and are thought to be relatively small SMBH's accreting very near the Eddington limit with very steep (i.e. soft) X-ray spectra (see, e.g., Pounds et al. 1995; Grupe et al. 1999).

Broad line radio galaxies (BLRGs) and narrow line radio galaxies (NLRGs) are radio-loud counterparts to Seyfert 1's and 2's, respectively. In this thesis radio-loud and radio-quiet sources will often not be differentiated; all broad line galaxies will simply be referred to as Seyfert 1's and all narrow line galaxies as Seyfert 2's.

1.1.3 The Dusty Torus

Antonucci & Miller (1985) were the first to produce the theory of unified AGN: a SMBH embedded in an optically thick, geometrically thin accretion disk, surrounded by an optically thick torus of material (Figure 1.3 from Urry &

Padovani 1995). This torus obscures the BLR whenever the line of sight to the nucleus is at an angle that passes through the torus, explaining why Seyfert 2's do not have broad optical emission lines in their spectra. Seyfert 1's, with a more "face on" view of the nucleus, have unobscured BLRs. A molecular torus provides extinction to optical emission, as well as absorbing UV and soft X-ray photons, likely re-emitting this energy thermally at infrared wavelengths. Classically, the torus has been thought to be located ~ 1 pc from the BH (e.g., Antonucci 1993) and has been modeled with a smooth distribution of material for simplicity. However, more recent models based on infrared observations of the dusty torus incorporate sub-pc scale Compton-thick clumps (e.g., Nenkova et al. 2008a; Elitzur & Shlosman 2006) which more accurately model radiation propagation and seem to match infrared observations much better. Two such models are shown in Figure 1.4 (Nenkova et al. 2008b). Other theories suggest that the torus may actually be the outer portion of the disk itself with a transition region at the dust sublimation radius. This transition region could also be the location of the BLR.

Clearly, the details of the size and geometry of the torus are not well known. Determining the size, shape and uniformity of torus properties in difference classes of AGN, and from object to object within a given class, could shed light on AGN unification schemes. Infrared observations are the most direct way of determining torus properties, but are limited to nearby objects. X-ray observations have two ways of exploring the torus: absorption by Compton-thick material in the line of sight and Compton reflection which could arise from the inner surface(s) of the torus.

1.1.4 Relativistic Jets

Jets are formed when hot plasma is ejected from the core of the AGN in narrow beams orthogonal to the accretion disk. This process is not well understood, though it is also seen in Galactic black holes on a much smaller scale. It is theorized that jets form due to the rapidly rotating magnetic fields around the black hole that funnel the plasma into diametrically opposed beams and that this process helps to shed angular momentum, which is necessary for accretion to occur. Blazars have

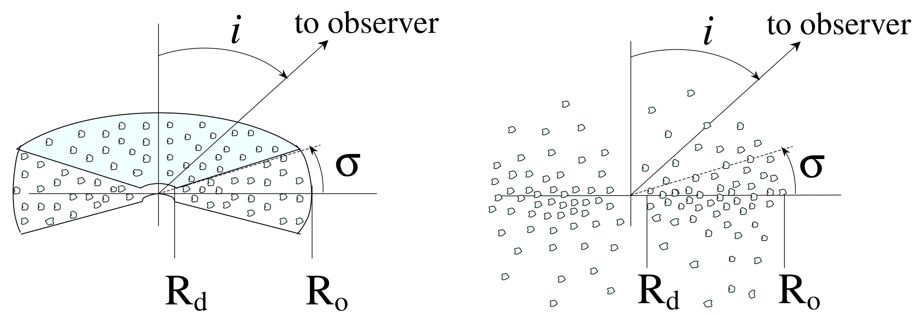

Figure 1.4: Clumpy torus model from Nenkova et al. (2008b). The model shown on the the left has sharp borders while the model on the right has a smooth distribution of clumps increasing in density from the pole to the equator. These models predict roughly 10–15 clumps along an equatorial ray to be consistent with infrared observations.

strong jet components that happen to be oriented along our line of sight. Emission from the beamed jet dominates over disk/coronal emission from the central region of the AGN, leading to typically featureless continua with high radio luminosities. AGN that have some radio emission from jets, but which are not dominated by them (i.e., the jets are not beamed directly toward us), are known as radio galaxies.

Jet emission arises primarily from synchrotron radiation by relativistic electrons caught in the strong magnetic fields of the beam. This creates what is known as the low energy synchrotron hump in blazar spectra and typically spans from radio to low X-ray energies. The high energy hump can be explained if the photons created by the synchrotron process (in BL Lac objects) or external photons such as from the disk or torus (in FSRQs) are scattered by the electrons in the jet plasma in an inverse Compton process that cools the electrons and boosts the energy of the photons. The peak frequencies of these two humps have been found to be correlated with each other (Fossati et al. 1998, Abdo et al. 2010), but are not fixed from object to object, as shown in Figure 1.2. This is likely due to higher photon fluxes cooling the electrons more rapidly, leading to lower electron temperatures.

1.2 X-ray Spectral Properties of AGN

X-ray emission is frequently seen in AGN and offers a wealth of information about the geometrical and physical make-up of the circumnuclear material. Since the central regions of AGN cannot be spatially resolved (only a handful of objects have had parsec to kiloparsec-scale structures resolved such as radio jets and the dusty torus), we must mainly rely on spectroscopy and timing in our study of these objects.

In Seyfert galaxies the primary X-ray continuum is thought to arise from the hot, Comptonizing electron or electron-positron pair corona close to the black hole (Haardt, Maraschi & Ghisellini, 1994). The exact geometry of the corona is not well known but may be in the form of an ionized outer layer of the inner accretion disk (Nayakshin et al. 2000) or the base of a launching jet (Markoff et al. 2005). It is expected that while the inverse Compton scattering off an ensemble of electrons will produce a power law in the X-ray regime, a high energy rollover may be seen at roughly three times the electron temperature in the corona (e.g., Haardt et al. 1994). Such rollovers have been observed in Galactic black holes (GBHs; e.g., Takahashi et al. 2007) and have been claimed in AGN using some early X-ray observatories such as *BeppoSAX* (e.g., Perola et al. 2002).

In contrast, blazar X-ray emission is usually completely dominated by the jet emission, either from the upper end of the Synchrotron hump or the lower end of the inverse Compton hump. Despite arising from different mechanisms, both Seyfert and blazar X-ray continua can usually be modeled as a power law with a photon index (Γ) of ~ 2. Sometimes it is necessary to model the bending of blazar spectra, for example using a broken power law with one photon index at low energies and a slightly steeper index at higher energies. While blazar X-ray spectra are usually featureless, in many Seyfert galaxies the continuum is reprocessed by the accretion disk or other circumnuclear material creating commonly seen features including absorption by circumnuclear material, ionized emission and absorption

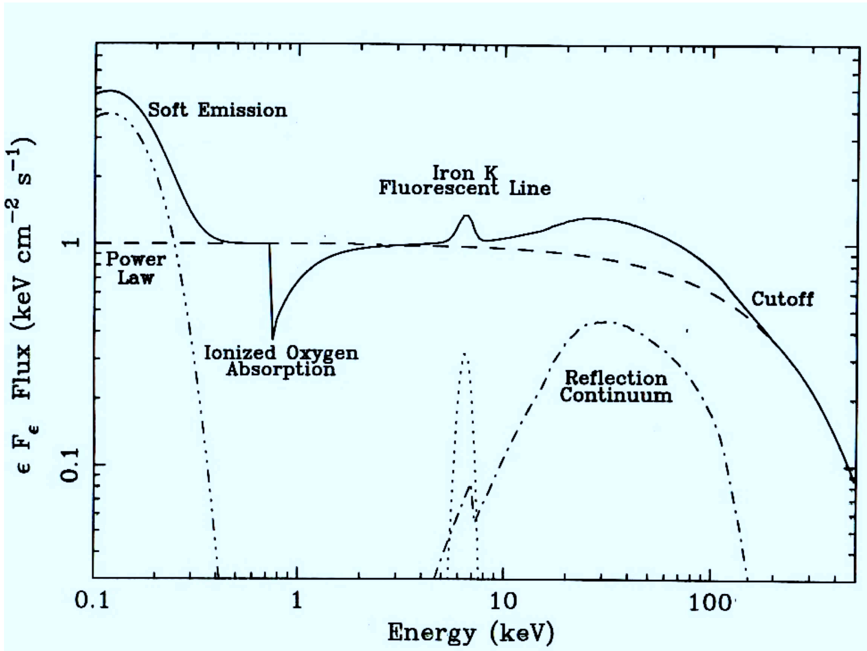

Figure 1.5: X-ray spectral components for Seyferts including the power law continuum, soft excess, absorption due to ionized O (warm absorber), the Fe Kα line, the CRH, and a high energy cutoff/rollover (from W.N. Brandt, private communication). The solid line is the sum of all the components shown.

lines below $\sim$ 2 keV, Fe K emission around 6–7 keV, and the Compton reflection hump (CRH) peaking around 20–30 keV (see Figure 1.5).

1.2.1 Absorption

Seyfert continua are commonly absorbed by material in our line of sight to the emitting source. Low energy X-rays are particularly subject to photoelectric absorption by atoms. The coefficient of photoelectric absorption, summed over all elements and ionization states (with appropriate relative abundances) can be approximated by

$$\alpha_{\rm photoelectric} = \left(\frac{Z_{\rm abund}}{Z_{\odot,\rm abund}}\right)\left(\frac{10keV}{\epsilon}\right)^{2.5}\sigma_{\rm T}, \tag{1.2}$$

where $Z_{\rm abund}/Z_{\odot,\rm abund}$ is the abundance of heavy elements relative to Solar abundances, ϵ is the photon energy, and $\sigma_{\rm T}$ is the cross section for Thompson scattering

(Kembhavi & Narlikar 1999).

Some of this material is in our own Galaxy and must be accounted for in our modeling. Absorption in addition to the Galactic column is likely from a region near the SMBH and is commonly characterized as either Compton-thin (equivalent Hydrogen column density $N_{\rm H} \lesssim 1 \times 10^{24}$ cm^{-2}) absorbing X-rays at energies $\lesssim$2–5 keV or Compton-thick ($N_{\rm H} \gtrsim 1 \times 10^{24}$ cm^{-2}) affecting X-rays at energies $\lesssim$5–10 keV. Many Seyfert 2's show strong absorption, which may be responsible for obscuring the broad optical lines in these objects in agreement with unification (Antonucci & Miller 1985). However, there is not a perfect correspondence of Seyfert type with level of X-ray obscuration (see, e.g., Akiyama et al. 2003), implying that other factors must be involved.

Infrared observations of AGN have recently shown that the dusty torus is likely comprised of a number of discrete clumps of material. If this is the case then we would expect that absorption by the torus could vary as clumps pass through the line of sight to the central source. This sort of activity is difficult to detect since it requires monitoring of sources over time periods of months and a relatively clean line of sight (aside from the torus) in order to see distinct events. I have analyzed such a campaign on Centaurus A (hereafter Cen A) which is explained fully in Chapter 4.

1.2.2 The Compton Reflection Hump

The CRH is a broad hump that peaks in the 20–30 keV range and is commonly seen in Seyfert spectra (e.g., Nandra & Pounds 1994) superimposed with the power law continuum. This hump arises when high energy photons are Compton scattered off neutral, optically-thick material. The energy of the scattered photon is dependent on the angle of scattering, losing more energy when scattered orthogonal to the incident direction of travel given by the equation for Compton scattering,

$$\epsilon = \frac{\epsilon_{\rm i}}{1 + \frac{\epsilon_{\rm i}}{\rm m_e c^2}(1 - \cos\theta)}, \tag{1.3}$$

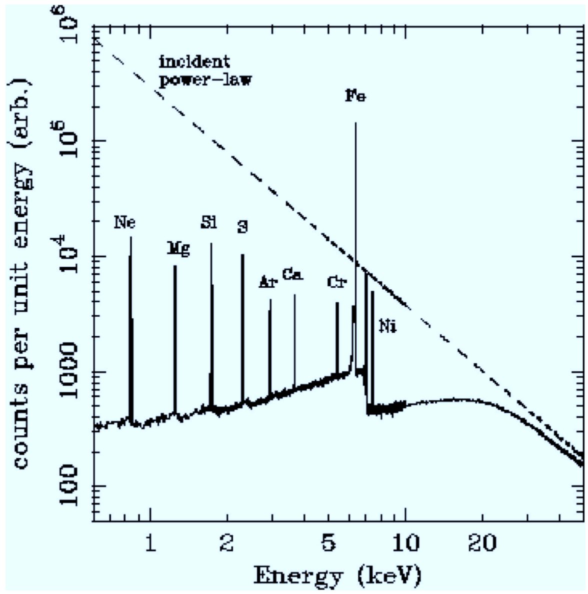

Figure 1.6: Compton reflection hump and fluorescent lines created by a power law of photon index 2.0 reflecting off a cold slab from Reynolds (1996).

where ϵ is the energy of the scattered photon, ϵ_i is the energy of the incident photon, m_ec^2 is the electron rest mass, and θ is the scattering angle. This has a number of effects, the first of which is that Compton reflection is anisotropic, with most of the radiation either forward scattered or reflected back anti-parallel to the incident photons. Photons that scatter at an appreciable angle will lose energy and are much more likely to be photoelectrically absorbed by atoms in the material, which fluoresce to create emission lines. Except in cases of Compton-thick absorbers in the line of sight, we expect to see photons which have been backscattered off the material close to anti-parallel, hence the term "reflection" when used to describe this phenomenon. Second, higher energy photons lose more energy to Compton recoil, an effect that becomes significant above $\sim$ 50 keV (George & Fabian 1991), while lower energy X-ray photons are more likely to be absorbed. This effectively attenuates both the soft and hard ends of an incident power-law and the result is a broad hump around 20–30 keV and a number of emission lines, particularly Fe Kα, which are shown in Figure 1.6.

The regions in which this is likely to occur are the geometrically thin, optically thick accretion disk or the Compton-thick molecular torus. Constraining the level of reflection relative to that of the illuminating power-law can, in principle, yield information on the sky-covering fraction of the reflecting material (as seen from the X-ray continuum source, assumed to be the central X-ray corona), thereby providing constraints on how much Compton-thick material is in the form of a torus or disk. In practice, however, this is not straightforward. In most Compton reflection models it is typically assumed that the reflector is seeing the same power-law continuum that we are. However, the illuminating X-ray continuum can be highly variable and since there is a non-zero light-travel time from the X-ray corona to the reflecting material, this can result in a discrepancy between the properties of the observed power-law continuum and the properties of the power-law continuum illuminating the reflecting material on short observational time-scales. Averaging over timescales much longer than the light-travel time from the source to the reflecting material eliminates this discrepancy.

An additional complication is the geometry of the reflecting material and its orientation relative to the observer. In this work, for simplicity, I have primarily used PEXRAV (Magdziarz & Zdziarski 1995), which assumes a semi-infinite slab, most applicable to a "lamppost" geometry wherein the illuminating X-ray source lies above an accretion disk. This model was created using Monte Carlo simulations and includes the Compton reflection hump and Fe K edge but no emission lines. It assumes a plane of Compton-thick material covering between 0 and $\sim 2\pi$ sterradians of the sky from the point of view of the illuminating source corresponding to R between 0 and ~ 1, with power law parameters, line-of-sight angle to the disk, abundances, and rollover energy as parameters. Torus reflection models are still in development, however I have tested MYTORUS by Murphy & Yaqoob (2009) which models the torus as a uniform doughnut-shape with a 60° opening angle. It self-consistently models absorption by the torus, the Compton-reflection hump, and Fe fluorescence, with the density of the torus and line-of-sight angle as the primary model parameters.

1.2.3 The Fe K emission complex

The Fe Kα emission line at a rest frame energy of 6.40 keV is commonly present in Seyfert X-ray spectra. Measurements of Doppler broadening of the Fe line (typical values of the FWHM are $\sim 10^5\,\mathrm{km\,s^{-1}}$) can provide information about the distance from the black hole of the accreting material, assuming Keplerian orbits. If the material is very close to the SMBH, then the emission can also undergo gravitational reddening, producing a broad red wing in the Fe line. Observation of a narrow Fe line only (FWHM $\sim 10^3\,\mathrm{km\,s^{-1}}$) could indicate a truncated accretion disk or a geometry in which the bulk of the material is farther from the black hole. If the material producing the Fe line is predominantly neutral, then we also expect to see Fe Kβ emission at 7.06 keV with roughly 13% the flux of the Fe Kα line and an Fe K edge at 7.11 keV. An example of an X-ray spectrum showing the Fe Kα, Kβ, and K edge are shown in Figure 1.7. Emission from highly ionized material, such as from Helium-like Fe XXV or Hydrogen-like Fe XXVI, can yield a line at a rest frame energy of 6.70 or 6.96 keV, respectively, but these lines are relatively rare and have been reported for only about a dozen Seyferts (Bianchi et al. 2005). The ionization level of material can place limits on the distance of material from the black hole, given the luminosity of the central source.

The strength of the Fe line (often measured as the equivalent width, EW, which is basically the flux of the line relative to the continuum) indicates an overall abundance of material surrounding the black hole that is being illuminated by the X-ray continuum. Combining knowledge of the Compton hump and Fe K line (see e.g., George & Fabian 1991 for disk reflection; Murphy & Yaqoob 2009 for torus reflection) can also yield estimates of the ionization states of Compton-thick material, and how much Fe K emission originates in Compton-thick versus Compton-thin material. For example, absent or weak Compton humps may indicate a truncated or optically-thin accretion flow, and in this case an Fe line would likely originate in Compton-thin material. Modeling the Fe line and Compton hump self-consistently, such as with the MYTorus model of Murphy & Yaqoob (2009), is a longterm goal, both to help refine these models and to test for a toroidal geometry of the circumnuclear reflecting material.

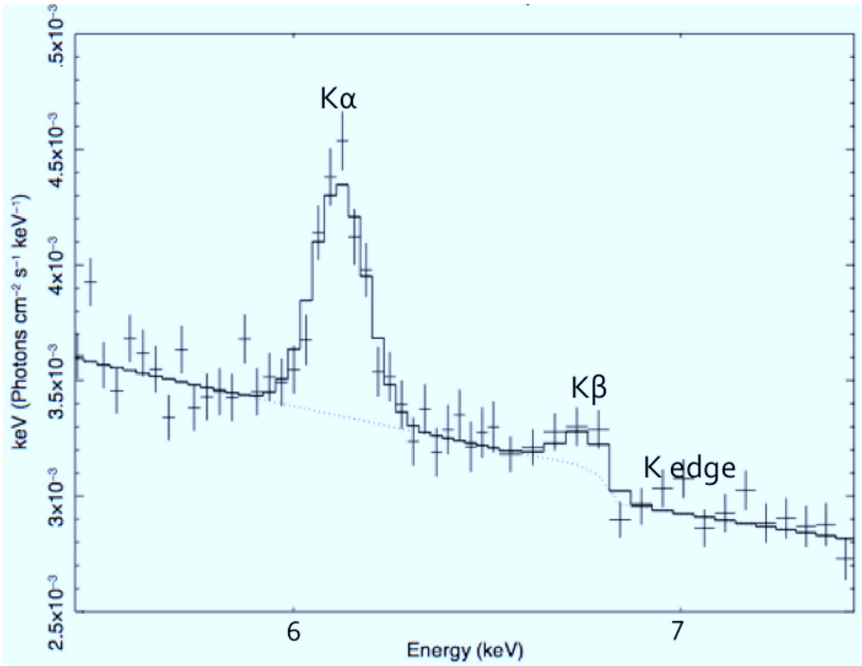

Figure 1.7: The Fe K emission complex including the Kα emission line, Kβ emission line, and K edge.

1.2.4 The Soft Excess

Excess emission above the continuum at soft X-ray energies ("soft" X-rays are usually defined as $\lesssim$2 keV)) is commonly seen in Seyferts (e.g., Arnaud et al. 1985), yet its origin is not understood. While a phenomenological blackbody component has generally been found to be a good fit, the invariance of the inferred temperature across a wide range of luminosities and black hole masses (see, e.g., Gierliński & Done 2004) has led to the general consensus that the soft excess is non-thermal in origin.

Reflection from an ionized medium is one possible explanation for this component. Modeling emission lines from ionized material that are blurred to form the soft excess has been shown to fit many Seyfert spectra well (Crummy et al. 2006). However, Gierliński & Done (2004) showed that absorption by partially ionized disk winds was indistinguishable from reflection off a similar medium, and that the wind velocities would cause the smearing of the lines. Emission lines from highly ionized Fe could provide evidence of the presence of ionized material in these objects, supporting these models. Recent work by Mehdipour et al. (2011)

provides an alternative hypothesis: that the soft excess is related to processes seen in the optical-UV, indicated by a correlation of the flux variability of the soft excess and UV components in Mkn 509. The soft excess could even be the high energy tail of the BBB.

1.2.5 Previous Surveys and the Advantages of Broad X-ray Spectral Analysis

AGN have been studied aggressively over the past several decades. Nandra & Pounds (1994) performed a spectral survey of 27 Seyferts observed with *Ginga* in the 1.5–37 keV range and found that Fe lines and CRHs were indeed common. Further work using the high resolution of the *Advanced Satellite for Cosmology and Astrophysics* (*ASCA*), *XMM-Newton* and *Chandra* observatories in the 2–10 keV range by Reynolds (1997), Yaqoob & Padmanabhan (2004), Nandra (2006), and Nandra et al. (2007), have yielded detailed Fe K complex parameters. However each of these instruments lacks broadband coverage above $\sim$ 10 keV, which makes it difficult to determine the level of reflection and therefore the precise shape of the underlying continuum. Perola et al. (2002) confirmed the presence of Fe lines and CRHs in broadband X-ray spectra with *BeppoSAX*. They also found evidence for high energy rollovers in the form of exponential cutoffs in the 100–300 keV range.

In the last decade the 20–100 keV sky has become more accessible, a development that is especially interesting for AGN because 20–100 keV AGN fluxes do not suffer from absorption by gas along the line of sight to the nucleus with $N_{\rm H} \lesssim 10^{24}$ cm^{-2}. *INTEGRAL* and *Swift*-BAT surveys are turning up large numbers of obscured AGN (including some that are rather bright above 20 keV), which are difficult to study in lower energy bands (e.g. Winter et al. 2009, Bird et al. 2007). These surveys yield detections and fluxes, and constrain AGN number densities and luminosity functions. However, for energy spectra in this band, the community has relied mainly on *Rossi X-ray Timing Explorer* (*RXTE*), *BeppoSAX* and *Suzaku*, and less recently, *High Energy Astronomy Observatory-1 (HEAO-1)* and the *Compton Gamma Ray Observatory's* Oriented Scintillation Spectrometer Experiment (*CGRO*-OSSE).

The primary goals of this thesis are to utilize the broad bandpass of *RXTE* and *Suzaku* to quantify the CRH, Fe line, and continuum parameters of AGN in order to better understand the nature of the accreting material surrounding AGN. These will be used to answer such questions as: How much of the Fe line arises in Compton reflection? How prevalent is the CRH? How common are rollovers in the 100–200 keV range? How should we be modeling the Compton-thick reflectors in Seyferts and radio galaxies? And what can be said about similarities and differences between the various classes of AGN?

2 *RXTE*, *Suzaku* and Data Reduction

2.1 The *Rossi X-ray Timing Explorer*

RXTE performed numerous observations of AGN over its 16-year lifespan with its two co-aligned pointed observation instruments, the Proportional Counter Array (PCA; Jahoda et al. 2006) and the High-Energy X-Ray Timing Experiment (HEXTE; Rothschild et al. 1998). The combined spectral energy range of the PCA and HEXTE was from 3–200 keV, ideal for quantifying the underlying continuum parameters as well as measuring the CRH, Fe Kα emission, and absorption by cold gas with column densities above $\sim 10^{22}$ cm^{-2}.

The sampling of AGN in the *RXTE* archive is highly inhomogeneous, as targets were proposed by various groups for a variety of reasons. This includes, for example, multi-timescale, continuous monitoring (numerous 1 ks snapshots evenly spaced hours or days apart for weeks to years) of Seyferts for power spectral density (PSD) measurements, long-look style observations for tens of kiloseconds at a time, and target of opportunity observations on flaring blazars as part of multi-wavelength campaigns. Figure 2.1 shows a sample of X-ray bright AGN from the *RXTE* archive. For many of these objects, the long-term monitoring data provides measurements of long-term baselines for spectral parameters.

We have analyzed all AGN in the *RXTE* archive for which high-quality spectra could be obtained. We began by analyzing a sample of 23 AGN from the archive with high quality HEXTE data out to at least 100 keV. This "broad" sample was intended find the prevalence of high energy rollovers in the 100–200 keV

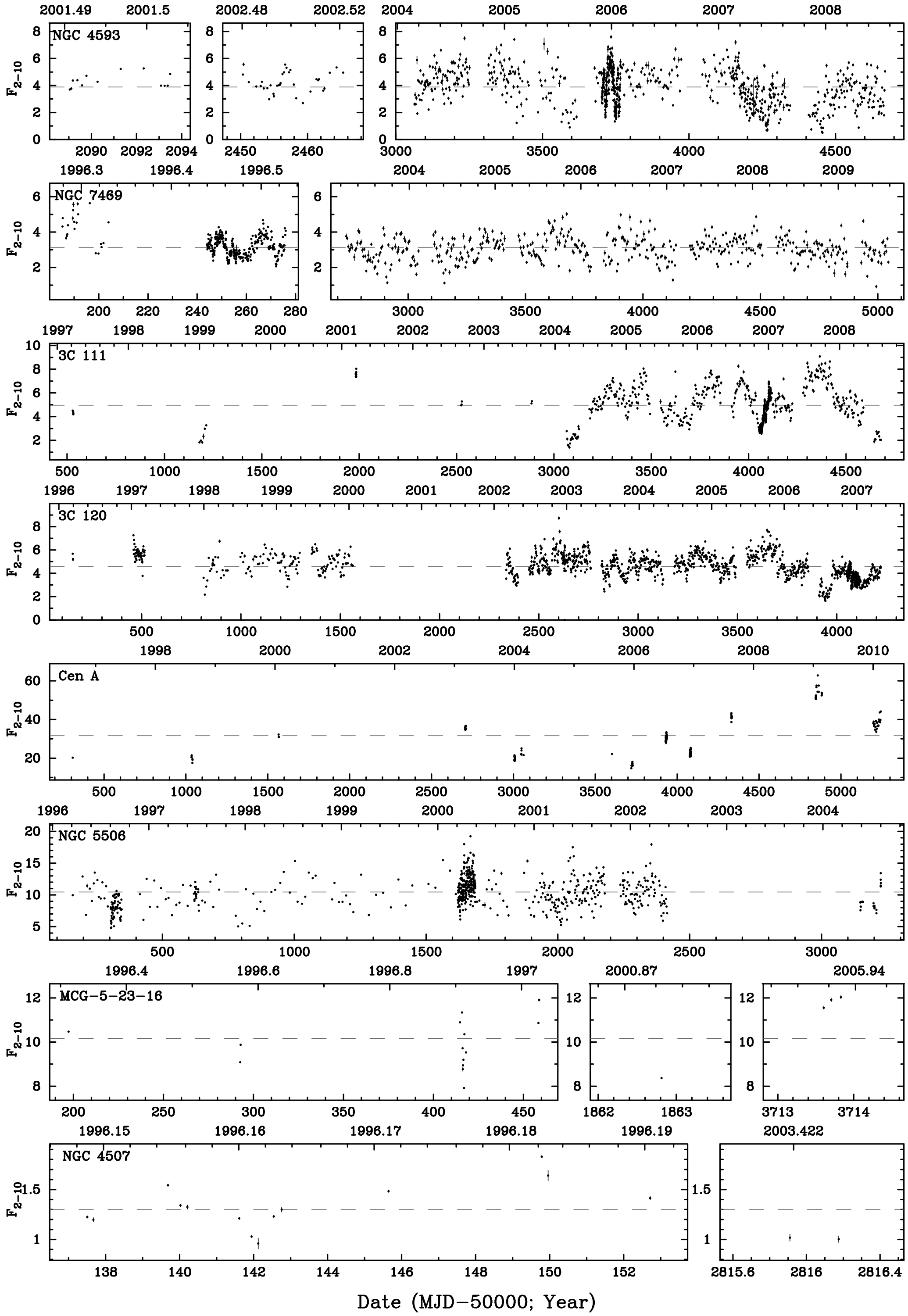

Figure 2.1: Sample lightcurves of several bright AGN from the *RXTE* archive. Note that some objects underwent long periods of monitoring while some were only visited on a handful of occasions.

range, quantify the prevalence of CRHs, and compare Fe line . We followed this up with a "full" sample of 100 objects that had high enough quality data to quantify spectral parameters. This expanded sample allowed us to perform tests on statistically large samples of different classes of AGN.

For all PCA and HEXTE data extraction and analysis we used HEASOFT software. For the broad band sample in Chapter 3 we used version 6.7 while for the full spectral sample in Chapter 3 and the time-resolved analysis of Cen A in Chapter 4 we used the more recent version 6.9.

2.1.1 The Proportional Counter Array

The PCA consisted of five large-area, collimated proportional counter units (PCUs) as shown in Figures 2.2 and 2.3. These gas chambers consisted of several layers of Xe and methane gas under a propane veto layer (for rejecting cosmic rays). An incoming X-ray interacting with the Xe gas created a number of ion pairs proportional to the energy of the photon.

Reduction of the PCA data followed standard extraction and screening procedures. PCA STANDARD-2 (i.e., not for high-resolution timing) data were collected from PCU's 0, 1 and 2 for observations prior to 1998 December 23; PCU's 0 and 2 for observations from 1998 December 23 until 2000 May 12; and PCU 2 only after 2000 May 12. PCU 0 lost its propane veto layer starting on 2000 May 12, PCUs 1, 3, and 4 have been known to suffer from repeated breakdown during on-source time, and PCU 1 lost its propane layer on 2006 December 25. PCU 2 is the best-calibrated of the PCU's and has maintained consistent functionality for the duration of *RXTE*'s mission (Jahoda et al. 2006).

To maximize signal to noise ratios we extracted events from the top Xe layer of the PCA only. Data were rejected if they were gathered less than 10° from the Earth's limb, within 20 minutes of satellite passage through the South Atlantic Anomaly (SAA), if the satellite's pointing offset was greater than $0^{\circ}.01$, or if the ELECTRON2 value (a measure of particle flux) was > 0.1.

For the broad sample, the PCA background was estimated using the "L7-240" background models, appropriate for faint sources when the total count rate

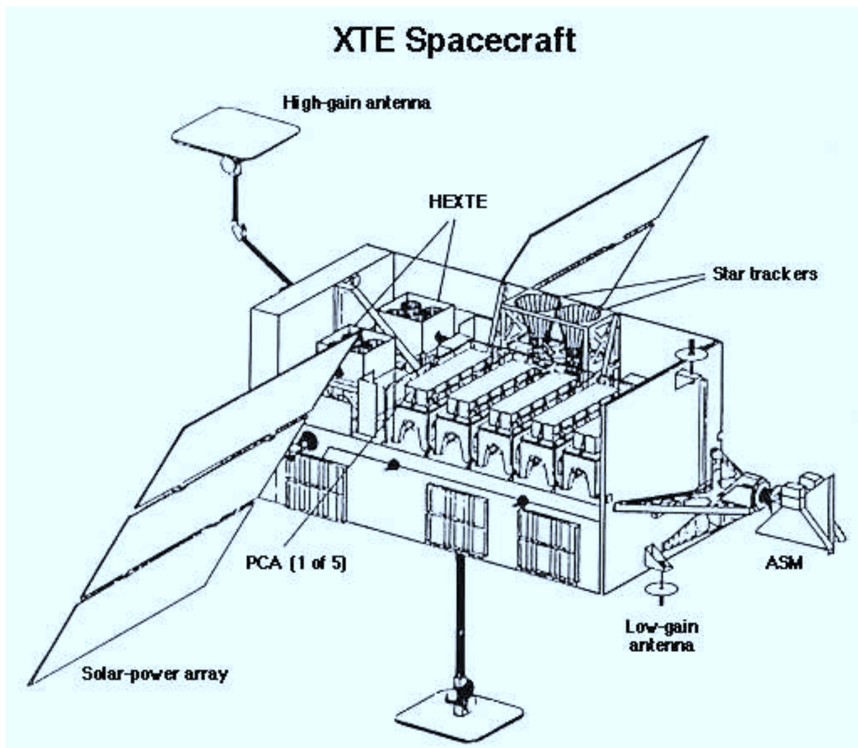

Figure 2.2: The *RXTE* spacecraft with the Proportional Counter Array (five units) and the High Energy Timing Experiment's two clusters in the central bus. Figure courtesy of NASA.

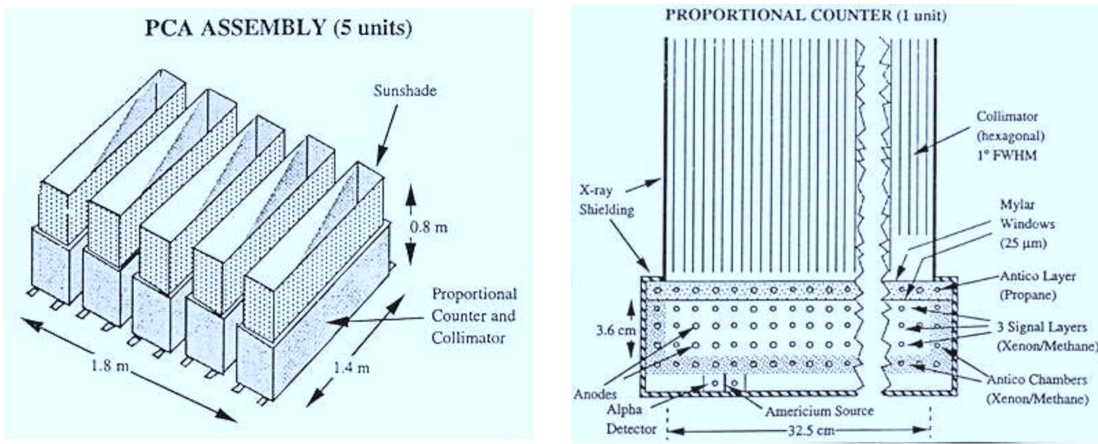

Figure 2.3: Proportional Counter Array assembly (left) and individual counter unit (right). X-rays enter through the collimator on top, go through the propane veto layer and into the series of Xenon/Methane detection layers. The entire unit is encased in anti-coincidence shielding. Figure courtesy of NASA.

was below 40 counts s^{-1} PCU^{-1}. For observations that fell above this flux threshold we used the Sky-VLE background model. See, e.g., Edelson & Nandra (1999) for details on PCA background subtraction, which is the dominant source of systematic uncertainty in these data. For the full sample, we used updated PCA background model files "pca_bkgd_cmvle_eMv20111129.mdl" for source fluxes brighter than ∼5 mCrab, and "pca_bkgd_cmfaintl7_eMv20111129.mdl" for source fluxes fainter than ∼5 mCrab. These updated models were obtained through private communication with Craig Markwardt.

Observations of 3C 454.3 were obtained using a pointing position $0^{o}.52$ to the southeast of the source in order to completely eliminate contributions to the spectrum from the cataclysmic variable, IM Peg, located about $0^{o}.72$ to the northwest of 3C 454.3 (see Jorstad et al. 2010). At this offset position, the PCA and HEXTE collimator efficiencies are both 45% (e.g., Jahoda et al. 2006); we corrected for this when generating the response matrices and during spectral fitting.

Objects which were deemed contaminated by other sources in the field of view were not analyzed. The three sources eliminated from analysis for this reason were 3C 84, which is embedded in a bright cluster, RGB J1217+301, which is very close to Mkn 766 on the sky and far fainter, and NGC 6814 which has the cataclysmic variable V1432 Aql in the field of view.

Source and background spectra were extracted for each observation and added using the HEASOFT fits file manipulation tool (FTOOL), SUMPHA, to create time-average source and background spectra. Source spectra were binned to a minimum of 50 cts bin^{-1} to ensure usefulness of the χ^2 statistic in determining significance and goodness of fit, although for nearly all energy bins the systematic uncertainties dominate over the statistical uncertainties. A systematic uncertainty of 0.2–0.5% was added to the source PCA spectra for some sources in order to place χ^2 into the range of 1–2 for the best fit model. Since the response of the PCA hardened slowly over time due to the gradual leak of Xe gas into the propane layer in each PCU, response files were generated for each separate observation using the FTOOL, PCARMF, and the latest calibration files available as of 2009 October. A time-averaged response file was generated by summing the individual response files and weighting them by their good exposure time and number of active PCU's.

2.1.2 The High Energy X-ray Timing Experiment

HEXTE consisted of two independent clusters (A and B), each containing four NaI(Tl)/CsI(Na) phoswich scintillation counters as shown in Figures 2.2 and 2.4 (Rothschild et al. 1998) that shared a common 1° FWHM field of view co-aligned with the PCA field of view. Each of the eight detectors had a net open area of about 200 cm^2. When an X-ray entered the detector it would deposit its energy in the NaI crystal, creating a pulse of energy that was picked up by the pulse height analyzer (PHA) and sorted into one of 256 energy bins. Incomplete deposits and cosmic rays (charged particles) created an additional pulse in the CsI scintillator and these events are rejected.

We extracted source and background spectra from each individual *RXTE* observation using Science Event data and standard extraction procedures. Data were rejected if they were gathered less than 10° from the Earth's limb, within 20

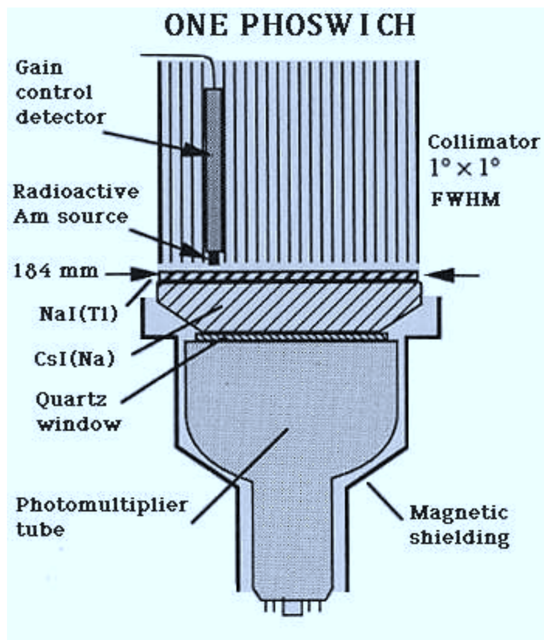

Figure 2.4: Diagram of a phoswich used in HEXTE with the collimator on top of the NaI scintillator and CsI scintillator (for vetoing cosmic rays). Figure courtesy of the HEXTE instrument team.

minutes of satellite passage through the SAA, or if the satellite's pointing offset was $> 0^{o}.01$.

To measure the background in real time, the two HEXTE clusters each underwent two-sided, orthogonal rocking to offset positions $1^{o}.5$ off-source (see Figure 2.5), with default switching every 16 s before 1998 January 8 and every 32 s thereafter. We used the online resources HEXTErock[1] and HEASARC's skyview tool[2] (looking at *Swift*-BAT and *RXTE* all-sky slew survey images) to ensure that there were no possible contaminating sources within 2^{o} of each source which were sufficiently bright above 20 keV to dominate the target.

Cluster A data taken during the following times were excluded, as the cluster did not rock on/off-source: 2004 December 13 – 2005 January 14, 2005 December 12 – 2006 January 4, during 2006 January 25, and after 2006 March 14. Detector 2 in cluster B lost spectral capabilities in 1996; spectra were derived from the other three cluster B detectors only. Deadtime corrections were applied to account for cluster rocking, pulse analyzer electronics, and the recovery time following scintillation pulses caused by high-energy charged particles. Typically, the HEXTE deadtime was around $30-40\%$.

We did not combine cluster A and B data. For observations after spring of 2006 we used only cluster B data and many of our sources have data from this period. We used standard response matrices and ancillary response files, hexte_97mar20c_pwa.rmf, hexte_97mar20c_pwb013.rmf, hexte_00may26_pwa.arf, and hexte_00may26_pwb013.arf.

2.1.3 HEXTE Background Considerations

The HEXTE background was sufficiently bright that it dominated over the source spectra for typical AGN fluxes. The HEXTE background subtraction is well-understood for source fluxes down to approximately 1% of the background (Gruber et al. 1996). Sources with 20–100 keV fluxes fainter than approximately 1% of the background and/or with insufficient exposure time had very large error

[1]http://mamacass.ucsd.edu/cgi-bin/HEXTErock.html
[2]http://skyview.gsfc.nasa.gov/

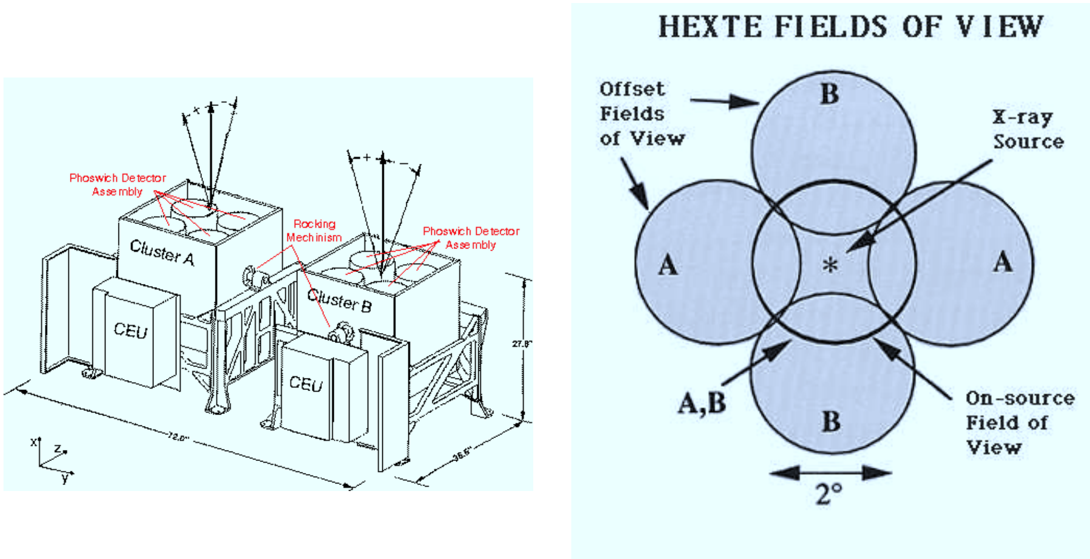

Figure 2.5: HEXTE clusters A and B rocking patterns and field of view. The offset fields of view provide the quasi-simultaneous background for A and B as shown. Figure courtesy of the HEXTE instrument team.

bars in their net spectra near 30 and 70 keV, the energies of the strongest activation lines that comprise the HEXTE background.

The average HEXTE background rate dropped by ∼50% (from ~ 12 to $6 \times 10^{-9}\,\mathrm{erg\,cm^{-2}\,s^{-1}}$) over a decade as the altitude of the *RXTE* spacecraft decreased, thus intercepting smaller regions of the SAA (Fürst et al. 2009), resulting in a smaller particle flux through the spacecraft and thus less nuclear activation of the iodine in the detectors. See Appendix A of Rivers et al. (2011b) for further details of the composition and long-term variability of the HEXTE background.

We combined observations with 16 s and 32 s rocking within each cluster, however this proved to be non-trivial because SUMPHA does not take into account the difference in background exposure time relative to on-source time (3/4 for 16 s and 7/8 for 32 s). The simplest solution to this problem was to perform background subtraction on the 16 s and 32 s separately before summing the spectra. We also created summed background files to use as correction files during fitting. This allowed the fit routines to adjust the level of background subtraction minutely (usually less than a few percent correction) to account for slight imperfections in the deadtime and ratio of background to on-source time.

2.2 Suzaku

In contrast to *RXTE*, many prominent modern X-ray observatories (*Chandra*, *XMM-Newton*, *Suzaku*) are not capable of performing numerous, evenly spaced observations of a given object because they do not have rapid slewing capabilities. Such observatories mainly perform single-epoch long-look observations and rarely visit a given source more than a few times. However, these observatories have advantages over *RXTE* with respect to energy resolution and soft X-ray energy coverage, so these individual snapshots are useful for quantifying Fe line parameters, warm absorption, and detecting the presence of a soft excess. I have analyzed two long-look *Suzaku* observations as part of my thesis work: MCG –2-58-22 and Mkn 590.

The Japanese X-ray observatory *Suzaku* is comprised of two main pointed instruments, the X-ray Imaging Spectrometer (XIS; Koyama et al. 2007) and the Hard X-ray Detector (HXD; Takahashi et al. 2007). All data were processed with the standard *Suzaku* pipeline with the recommended screening criteria (as per the *Suzaku* Data Reduction Guide[3]). All *Suzaku* extractions were done using HEASOFT version 6.9.

2.2.1 The X-ray Imaging Spectrometer

The XIS was originally comprised of one back-illuminated (BI) and three front-illuminated (FI) CCD cameras, however one CCD camera ("XIS2") has been inoperative since 2006 November (see the *Suzaku* ABC Guide for details). Each CCD camera (shown in Figure 2.6) is placed in the focal plan of the X-ray Telescope (XRT) module with a field of view $18' \times 18'$ square. The energy range of the XIS is nominally from 0.4 to 12 keV, however the effective area of the BI drops significantly above 10 keV and data are often ignored above this energy. The BI

[3]http://heasarc.gsfc.nasa.gov/docs/suzaku/analysis/abc/abc.html

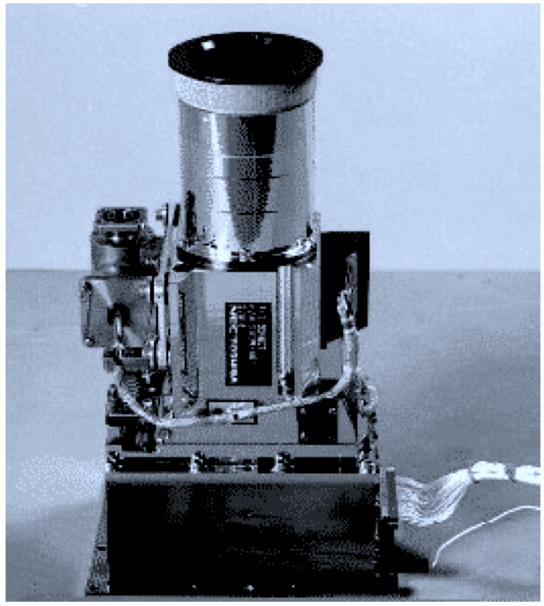

Figure 2.6: A single XIS CCD camera. Figure courtesy of NASA.

has a larger effective area at low energies than the FI, however time-dependent calibration issues (significant after ∼2006) of the instrumental O K edge at 0.5 keV due to build-up of contaminants on the optical blocking filters covering the CCDs have necessitated ignoring data below ∼0.7 keV for the BI and ∼1.0 keV for the FI. Additionally, the XIS data contain known calibration uncertainties between 1.5 and 2.4 keV due to the Si K complex and Au M edge arising from the detector and mirror system. To account for this, additional Gaussian components in the model fitting may be used to reduce the residuals, or one may simply omit this energy range (see Chapters 5 and 6 for examples of each method).

The screened XIS events data were cleaned and data from different editing modes were summed to create image files for each XIS. From these we extracted source and background lightcurves and spectra using a standard extraction radius of 2' for the source and four background regions of equivalent area. We then used XISRMFGEN and XISSIMARFGEN to create the response matrix and ancillary response files. We co-added data from the two working front-illuminated CCDs after confirming that the spectra were consistent with each other.

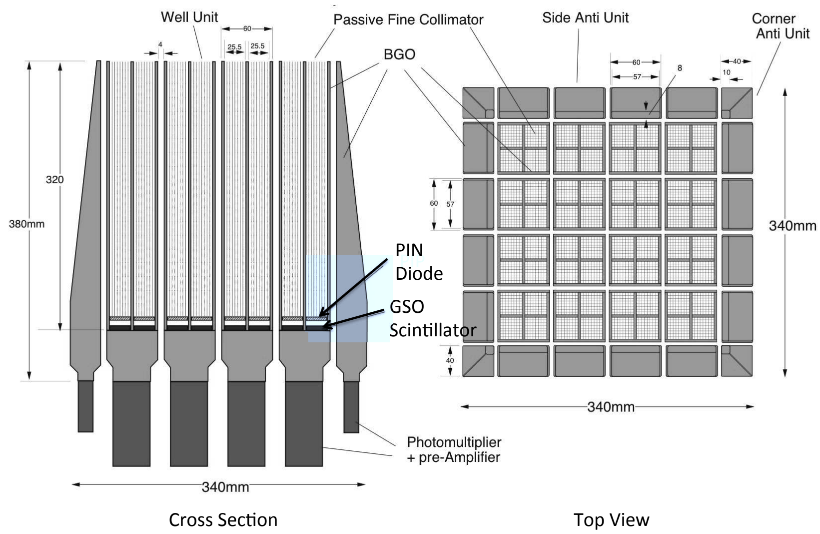

Figure 2.7: The HXD instrument showing the fine collimator and the BGO anti-coincidence active shields (and coarse collimator) above the PIN diodes and GSO scintillators. Figure courtesy of NASA.

2.2.2 The Hard X-ray Detector

The HXD consists of two detectors, the PIN diodes and the GSO scintillators, placed one on top of the other as shown in Figure 2.7. The passive fine collimator gives the HXD a field of view that is $34' \times 34'$ square below 100 keV and $4^{o}.5$ square above that. Each PIN diode consists of a p-type and n-type doped semiconductor with a non-doped, "intrinsic" semiconductor sandwiched in between. An incoming X-ray deposits energy in the intrinsic semiconductor creating a current through the diode which is then read out. We did not analyze the GSO data for either of our sources due to the faintness of the sources relative to the instrument background in the GSO band. The PIN energy range nominally is from $\sim$ 10–76 keV, however thermal noise at the low end required ignoring data below 13–17 keV and since the effective area falls dramatically above 60 keV, no data were used above this energy. The HXD is a non-imaging instrument and the instrument team provides non-X-ray background (i.e., Cosmic ray/particle background) model event files for each observation. Instrument background estimates yield $\lesssim 1.5\%$ systematic uncertainty at the 1σ level (Fukazawa et al. 2009). We simulated the Cosmic X-ray Background in XSPEC v.12.6.0 (Arnaud et al. 1996) using the form of Boldt (1987) as recommended in the Suzaku ABC Guide and created a combined CXB and non-CXB background file for each observation.

2.3 Methodology

Once the spectra were reduced, we needed to compare them to models including the power law continuum, neutral absorption, Fe line emission, a CRH, and in some cases either a warm absorber or a soft excess component. All spectral fitting was done using the software package XSPEC to perform χ^2 fitting. We assumed cross-sections from Verner et al. (1996) and used solar abundances of Wilms et al. (2000). Uncertainties were calculated at the 90% confidence level ($\Delta\chi^2 = 2.71$ for one interesting parameter) unless otherwise stated. All spectra were modeled with cold galactic absorption ($N_{\rm H,\,Gal}$) with values taken from the LAB survey (Kalberla et al. 2005).

2.4 Acknowledgements

Chapter 2, in part, is a reproduction of material as it appears in the Astrophysical Journal, Rivers, Markowitz & Rothschild, ApJ, 2011a, and Rivers, Markowitz, Duro & Rothschild, ApJ, 2012; and in part has been submitted for publication to the Astrophysical Journal 2012, Rivers, Markowitz & Rothschild. The dissertation author was the primary investigator and author of this material.

3 The *RXTE* Active Galactic Nuclei Survey

3.1 The 23 Brightest AGN in the *RXTE* Archive

To begin our analysis we have taken advantage of the large quantity of AGN data in the *RXTE* archive to investigate the nature of accreting material in SMBH's using broad band X-ray spectral data. We concentrated on quantifying the strengths of Compton reflection components which will tighten constraints on the quantities of Compton-thick circumnuclear gas, and searching for cut-offs or rollovers in the high energy power-law continuum, which could place constraints on thermal Comptonization processes in the corona (Haardt et al. 1994). We have closely examined *RXTE* archival data for 23 of the X-ray brightest AGN and we were able to construct spectra summed over the last 14 years covering from 3 to above 100 keV. Our analysis has taken advantage of the fact that the two pointed-observation instruments, the PCA and HEXTE, always operated simultaneously, removing ambiguity due to source variability inherent in splicing non-simultaneous < 10 and >10 keV data sets from different missions as is commonly done to achieve broadband coverage.

RXTE has been commonly used for continuous and sustained long-term monitoring and many of the X-ray brightest AGN have been monitored for at least 5–10 years. For many of the objects in this sample, the spectra are time-averaged over timescales of years, and thus these results serve as a reference for long-term average spectral properties in the hard and very hard X-ray bands. This investigation also serves to support the legacy of *RXTE* by maximizing the AGN science return from HEXTE.

3.1.1 Selection Criteria

Our goal was to obtain high-quality spectra out to at least 100 keV for each source. This required a combination of the source being sufficiently X-ray bright in the 20–100 keV range and having been observed with a sufficiently long total exposure time. For each source, we simply used all data available in the public archive regardless of sampling. We used data up to 2008 July (plus proprietary data up to 2009 July for NGC 7469 and proprietary data in 2009 January and February for Cen A). We did not make any effort to isolate a particular class of AGN. The decision to include an object from the archive in this sample was guided by HEXTE data quality alone. We required a 3σ detection of the source at 100 keV in order for a source to be included. The limiting 20–100 keV flux was roughly $\gtrsim 5 \times 10^{-11}$ erg cm^{-2} s^{-1}, depending on exposure time and the long-term trends in the HEXTE background. For sources whose net fluxes were in the range 0.7–1.2%, 1.2–1.5%, and 1.5–2.0% of the background, the good exposure times per HEXTE cluster after screening required to yield acceptable-quality spectra were approximately 250, 100, and 50 ks, respectively.

These criteria for target selection bias this sample towards objects with flat spectra, except in the case of objects which happened to have very high fluxes and/or extremely long total exposure times. Hence this sample is not statistically complete, specifically we are biased against selecting NLSy1's. The final sample of 23 AGN contains a variety of AGN subclasses, including 17 Seyferts, 2 BLRGs, 2 FSRQs and 2 BL Lac objects. Some objects had PCA + HEXTE spectra already published, but in most cases we have updated these spectra by including additional data. Selected sources are listed in Table 3.2; inclusion in the broad sample is indicated by bold source names.

3.1.2 The 20–100 keV Bandpass

The PCA was usually considered the primary instrument when observing. Since HEXTE only extended down to 17 keV it has been commonly overlooked for faint sources such as AGN, especially for short observations. This investigation demonstrates that accumulation of data over long time scales can indeed yield high quality HEXTE spectra for the brightest AGN.

To explore target properties in the 20–100 keV bandpass we fit a simple power law to HEXTE-only data. We fit HEXTE-A and B spectra with the power law normalizations untied due to the fact that for several sources, the HEXTE-B data covered a longer time span than HEXTE-A. We kept the photon indices tied between A and B since untying the photon indices did not yield a significant improvement in the fit for most sources. The only exception to this was 3C 273, for which untying the photon indices and power law normalizations led to an improvement in fit of $\Delta\chi^2/\mathrm{dof} = -8/2$ with photon indices of 1.79 ± 0.02 and 1.71 ± 0.02 for cluster A and B respectively. Tied photon indices, absorbed fluxes, and goodness of fits are listed in Table 3.3. Brightness level as a percent of background in the 20–100 keV band is also listed. Notice that there are about a half dozen sources where a simple power law is a bad fit, due to extra curvature possibly indicating a Compton reflection hump or a high energy rollover.

3.1.3 Model Fitting of the 23 AGN Broad Sample

One of our primary goals with this subsample was to make use of the 3–100 keV spectra to test for the presence of Compton humps and high-energy cut-offs. To begin, we created a baseline model consisting of a primary power law with Galactic absorption plus an Fe line but with no Compton reflection or high energy cut-off of the continuum. This alone was a suitable baseline for most of the Seyfert 1's. In the case of both Compton-thin and Compton-thick Seyfert 2s, the baseline model additionally included a "ZPHABS" component to model cold absorption in excess of $N_{\mathrm{H,\,Gal}}$. In the case of the Compton-thick Seyfert 2s, Circinus and NGC 4945, we also included a soft power-law absorbed only by $N_{\mathrm{H,\,Gal}}$, to model e.g., scattered nuclear X-ray continuum emission, thermal emission from diffuse plasma or other unresolved X-ray sources in the host galaxy, and/or "leaked" continuum emission in the case of a partial-covering absorber.

The Fe K emission complex is virtually ubiquitous in Seyfert spectra, however the PCA could not deconvolve broad and narrow Fe lines, nor Fe Kα and Kβ lines. In addition, the PCA could not resolve an Fe line except in cases of extreme relativistic broadening. We have therefore used a single Gaussian to fit the Fe K emission complex. The reader is referred to results from instruments with superior energy resolution at 6 keV, namely *XMM-Newton*, *Chandra*-HETGS, or *Suzaku*, to determine if the Fe line we model is dominated by a broad or a narrow Fe component, or a blend of both in each object.

For each object, we included warm absorber components as needed by searching through publications relying on *Chandra*-HETGS and/or *XMM-Newton*-RGS data. The PCA was not highly sensitive to discrete narrow absorption lines. However if a warm absorber phase's spectral signature was to induce low energy continuum curvature below 5 keV of more than 1–2%, then we modeled it with an XSTAR table component, keeping the parameters frozen at the column density and ionization parameter specified in the literature (for references see Table 3.2.

Next we added a Compton reflection component using PEXRAV (Magdziarz & Zdziarski 1995) with all abundances set to solar and no high energy rollover. The inclination was set to 30^o for Seyfert 1-1.5's and 45^o for Seyfert 2's. Significant improvement in fit was found for all objects except MR 2251–178, 3C 111, and Cen A. Best fit models including PEXRAV are shown in Figures 3.1–3.3 for select sources. Best fit model parameters for all sources are listed in Table 3.4 including fluxes and luminosities for the 2–10 keV and 20–100 keV ranges. Luminosities were calculated following, e.g., Alexander et al. (2003, their Eqn. 1), correcting for all absorption in the line of sight (including warm absorbers and cold Galactic absorption). Luminosity distances were taken from the NASA Extragalactic Database (NED). For each object, the mean of the available redshift-independent estimates was used if available, otherwise the luminosity distance based on redshift (using the 3K cosmic microwave background radiation as a reference frame) was used.

Next we tested for the presence of high energy continuum cut-offs. We

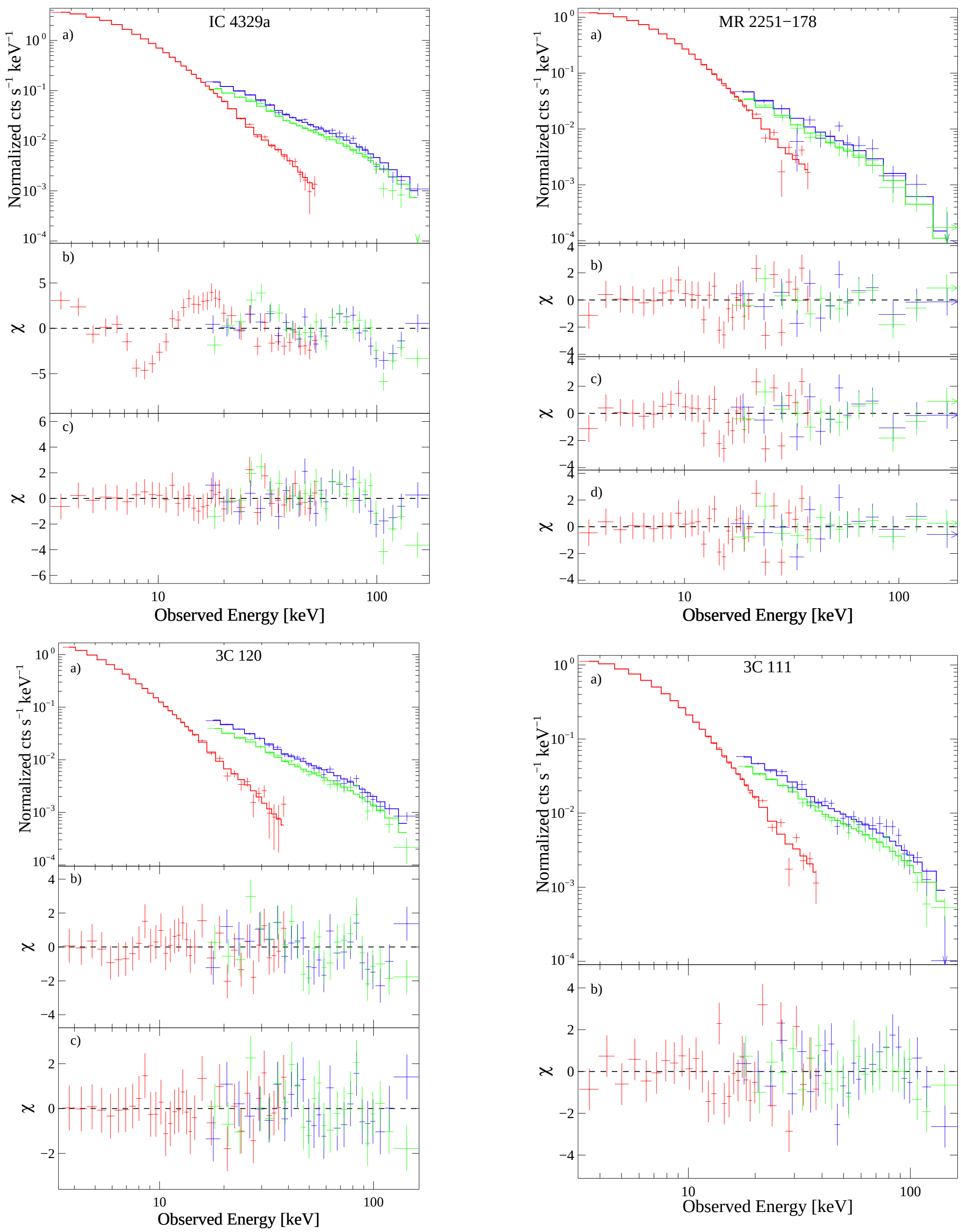

Figure 3.1: Data, model and data–model residuals for four Seyfert 1's in the broad sample. Panel (a) shows the PCA and HEXTE data along with the best-fit model (solid line); panel (b) shows residuals for the baseline model without Compton-reflection; panel (c) shows residuals with Compton-reflection if it was significant to include; and panel (d) shows residuals with a rollover if a rollover was significant to include.

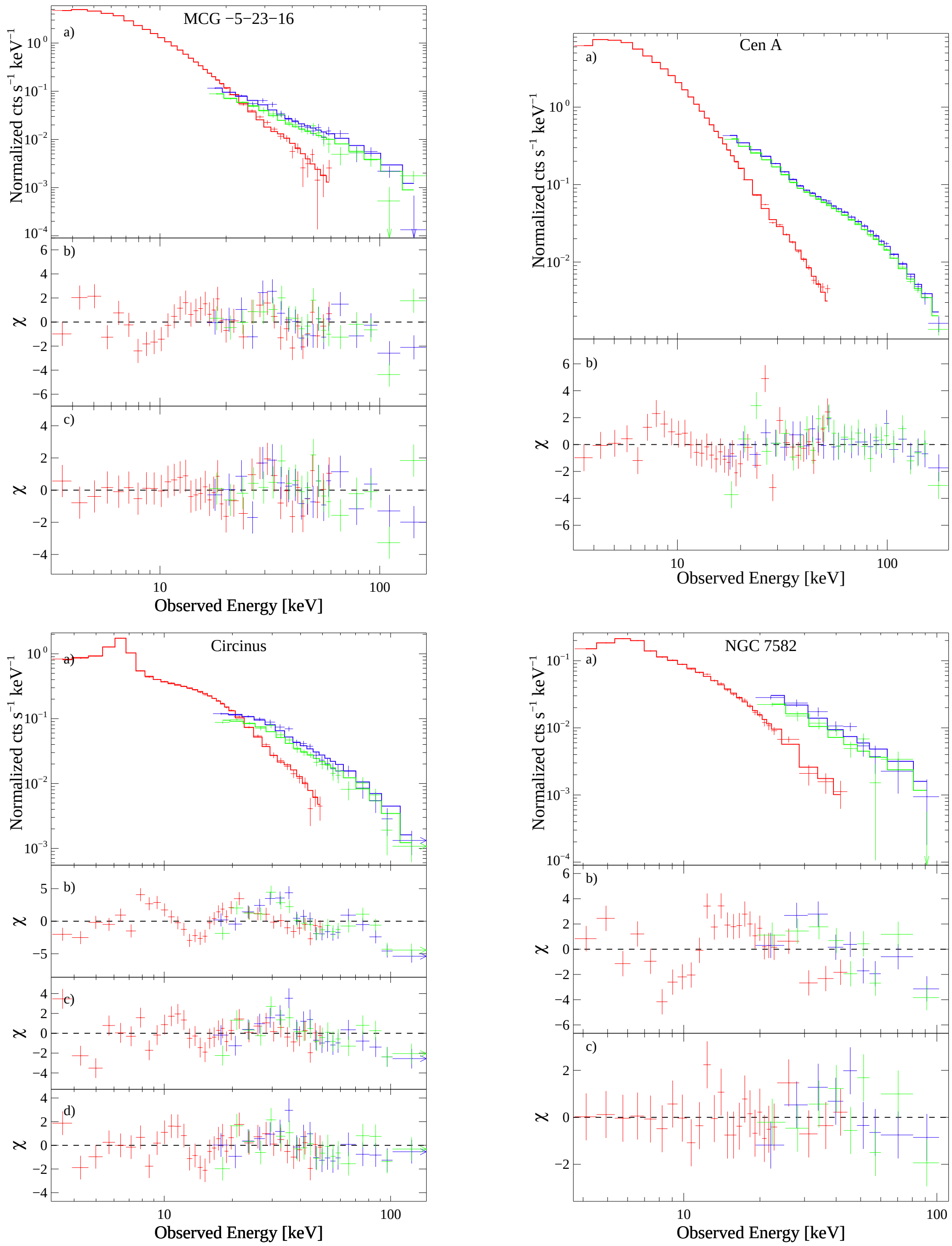

Figure 3.2: Data, model and data–model residuals for four Seyfert 2's in the broad sample. Panel (a) shows the PCA and HEXTE data along with the best-fit model (solid line); panel (b) shows residuals for the baseline model without Compton-reflection; panel (c) shows residuals with Compton-reflection if it was significant to include; and panel (d) shows residuals with a rollover if a rollover was significant to include.

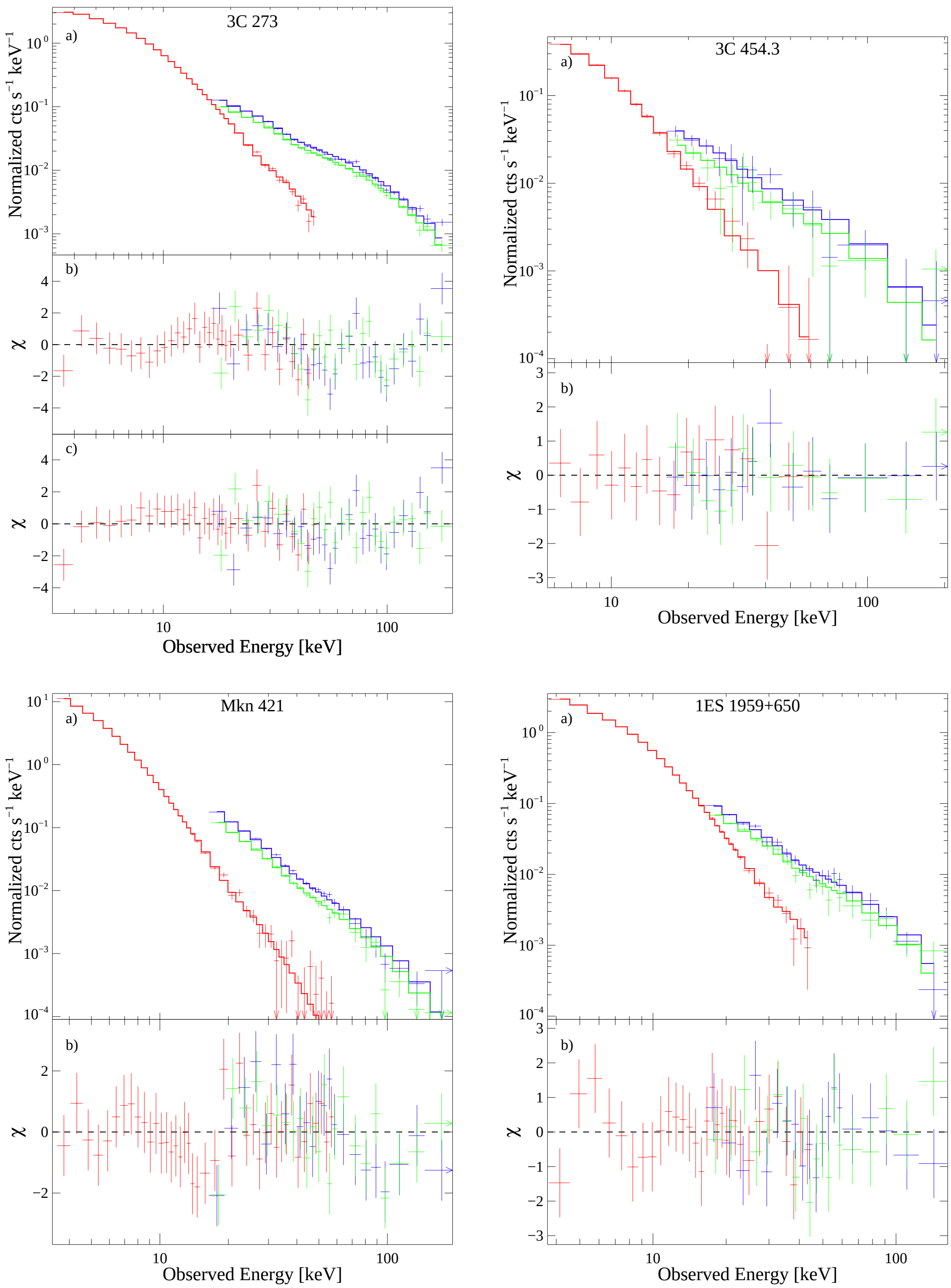

Figure 3.3: Data, model and data–model residuals for the four blazars in the broad sample. Panel (a) shows the PCA and HEXTE data along with the best-fit model (solid line); panel (b) shows residuals for the best-fit model.

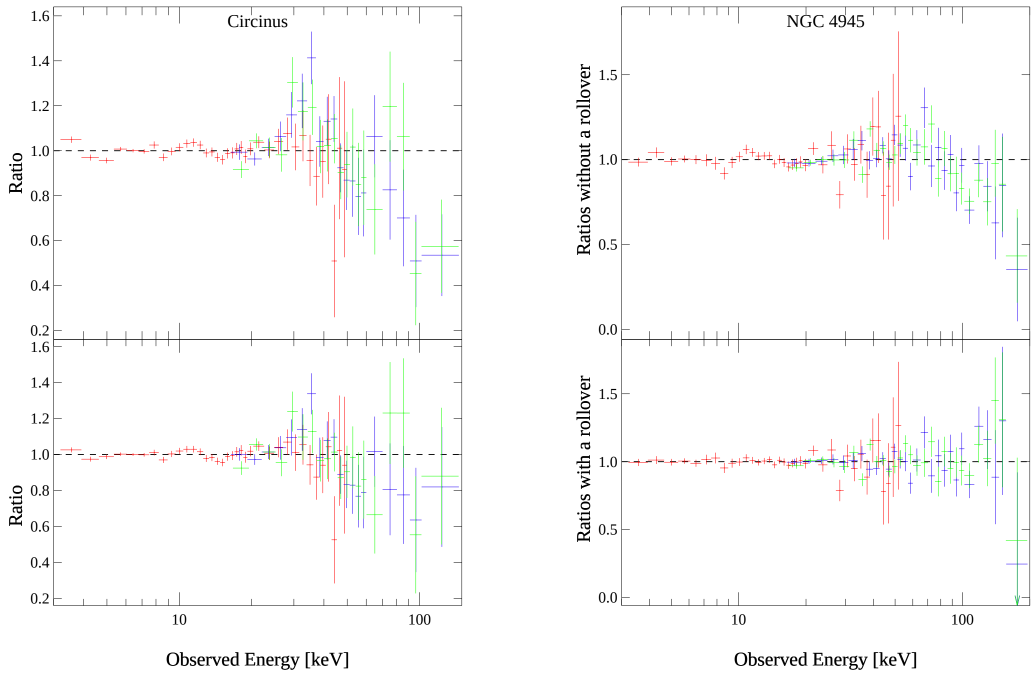

Figure 3.4: Data to model ratios for Circinus (*left*) and NGC 4945 (*right*) for the best-fit reflection models (*top*) and best-fit rollover models (*bottom*). Parameters are given in Tables 3.4 and 3.5 for the different models.

tested two forms for the cut-off, "CutoffPL" and "HighEcut". CutoffPL (which is a bit of a misnomer) has a slow rollover where the continuum at E_{roll} is $1/e$ times the initial value. HighEcut has a much more abrupt cut-off governed by the following equations: $\mathrm{A(E)} = e^{(\mathrm{E_{cut}} - \mathrm{E})/\mathrm{E_{fold}}}$ for $\mathrm{E} > \mathrm{E_{cut}}$; $\mathrm{A(E)} = 1$ for $\mathrm{E} < \mathrm{E_{cut}}$. Since we did not see evidence for such abrupt cut-offs in the data, results found using this model are not presented in this paper. E_{roll} was limited to a hard lower bound of 50 keV in all cases with the exception of Circinus which shows evidence for a rollover at slightly lower energies (∼40 keV).

Best fit CutoffPL results are listed in Table 3.5. We found significant improvement in fit ($\Delta\chi^2 > 50$) for two objects, Circinus and NGC 4945 and marginal evidence ($\Delta\chi^2 \sim 10$) for a rollover in MR 2251–178. Data to model ratios for the best-fit reflection and rollover models that demonstrate the extra curvature in Circinus and NGC 4945 that indicates the presence of a high energy rollover are shown in Figure 3.4. In all other cases, we found only lower limits for rollovers as χ^2 did not improve, nor was there marked improvement in data to model residuals

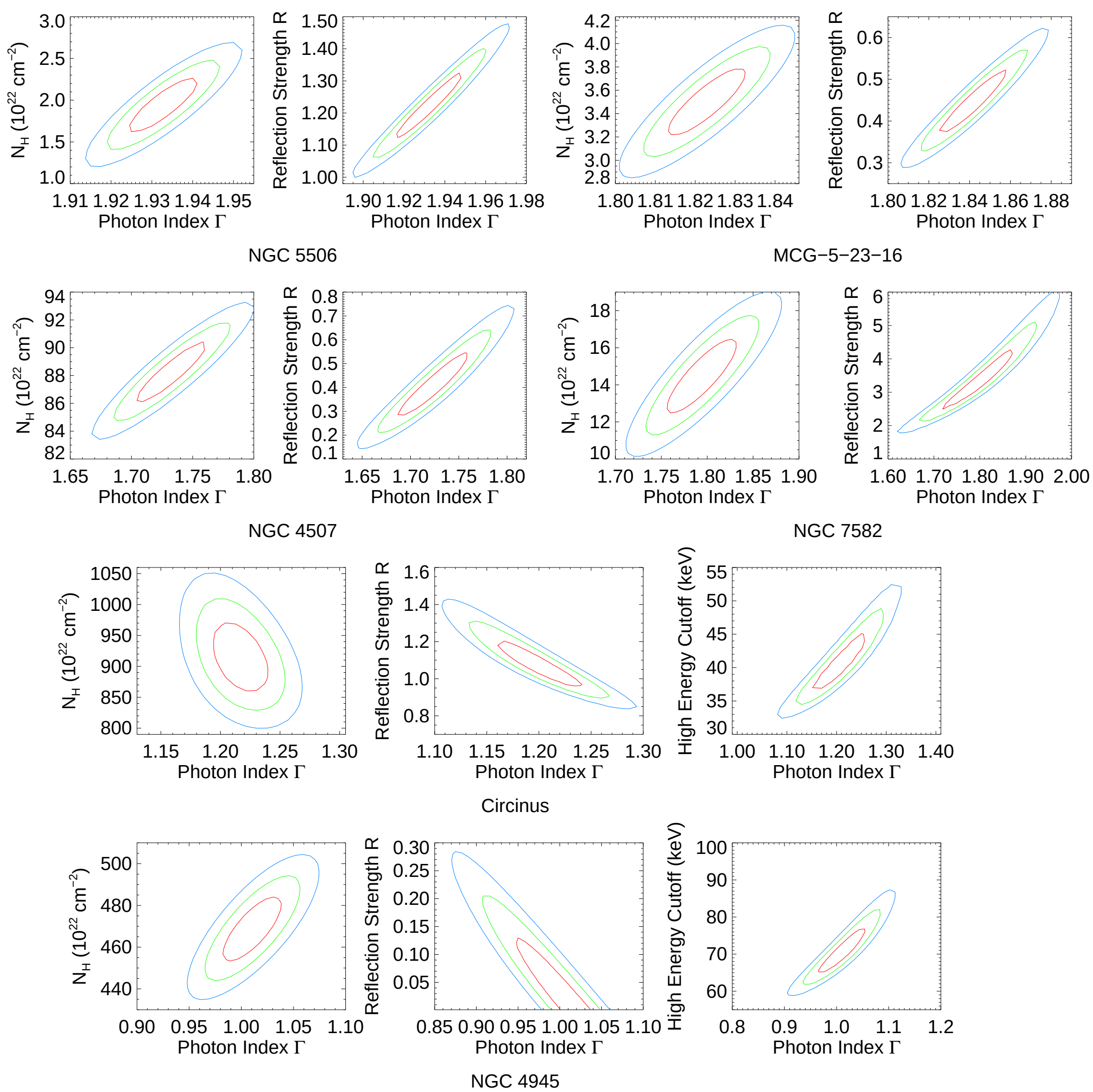

Figure 3.5: Contour plots of various parameters for Seyfert 2's in the broad sample, illustrating the degree of statistical degeneracy seen in these objects.

at high energies (as seen in Figure 3.4).

Unfortunately, for the two cases (both Compton-thick Seyfert 2's) where the rollover substantially improved the fit, systematic degeneracies present between Γ, $E_{\rm roll}$ and R lead to unrealistically low values of the photon index when a rollover is modeled. We include contour plots of $N_{\rm H}$ vs. Γ, R vs. Γ and $E_{\rm roll}$ vs. Γ (in instances where a rollover was detected) in Figure 3.5 for Seyfert 2's to identify potential model degeneracies. In nearly all cases statistical degeneracies are minimal, the one exception being NGC 7582, for which the reflection strength is very poorly constrained.

3.2 Full Spectral Survey

As a followup to the broad survey, we analyzed every AGN in the *RXTE* archive with high enough data quality to accurately measure Γ to within 10%, as well as to quantify the CRH and Fe Kα line equivalent width (EW) in most cases. This quadruples our sample size compared to the broad sample. The energy range for these spectra was from 3.5 keV up to at least 20 keV and as high as 200 keV for some objects. This sample will allow us to analyze the spectral components discussed above with an emphasis on bulk properties of different types of AGN, providing a test of the unified model.

3.2.1 Selection Criteria

In 16 years *RXTE* observed 153 AGNs: 54 Seyfert 1's, 47 Seyfert 2's, and 52 Blazars, many of them multiple times. The sampling of these objects has been highly inhomogeneous since different viewing schemes were proposed for each object at various times and for various scientific goals. As before, we have included in our analysis all data for each object, regardless of sampling, in order to construct our overall averaged spectra.

We wanted to construct energy spectra of as many of these AGNs as possible, however several of these object were observed only once or twice for a handful of kiloseconds. It was therefore important for us to find the necessary conditions required to construct useful spectra. We decided to include a source in our sample if fitting the PCA data in the range 3–30 keV with a simple absorbed power law gave errors on the photon index of $\lesssim$ 10%. We included HEXTE data if the source was detected by HEXTE at the 3σ level at 50 keV, otherwise only the PCA data were used. For the PCA we found that approximately 40,000 total net counts was sufficient to give error bars of $\lesssim$ 10% on Γ. For HEXTE we found that roughly 5,500 counts was necessary to detect the source at the 3σ level at 50 keV, however the steepness of the spectrum was also a factor.

Using these selection criteria, we constructed time-averaged spectra for 100 AGN in total with 34 blazars and 66 Seyferts including 29 Seyfert 1's/BLRGs, 11 NLSy1's, and 26 Seyfert 2's/NLRGs, 7 of which were Compton-thick. The names, redshifts and exposure times for each object in our sample are listed in Table 3.2. Approximately 60 AGN were observed in the lifetime of *RXTE* which are not included in our sample. Most of them were very faint and/or were not observed for very long. These AGN are listed in Table 3.11 including their type as determined by NED, PCA exposure time, F_{2-10}, and Γ where it was possible to constrain.

3.2.2 Methods and Analysis

In our model fitting we included free normalization constants for HEXTE-A and B with respect to the PCA. This accounts for cross-instrument calibration as well as differences in observing epochs for HEXTE-A and B. Additionally we included the RECORN component in all our models which renormalizes the background level to account for slight imperfections in background subtraction. This was done separately for the PCA, HEXTE-A, and HEXTE-B data sets and the adjustment was usually less than $\sim$2% percent for any one set of data. Band-passes used for each object were determined on an ad hoc basis, excluding data above a certain energy if the error bars for the data became too large to add any information. For most objects the range used was 3.5–50+ keV for the PCA or PCA+HEXTE, though some of the very faint or very steep objects (NLSy1's for example) only had usable data up to $\sim$20–30 keV (these objects had PCA data only).

For all Seyferts our most basic model included an absorbed power law continuum plus Fe Kα emission modeled by a simple Gaussian and the Compton reflection hump modeled with a disk geometry by PEXRAV (Magdziarz & Zdziarski 1995). Galactic absorption was included for all sources (Kalberla et al. 2005) with warm absorbers included where well-determined values were found in the literature and had the potential to affect the spectrum curvature below 5 keV, as was done in the broad sample. Additional cold absorption in the line of sight was included for many Seyfert 2's, however for most Seyfert 1's and some Seyfert 2's cold absorption in addition to the Galactic did not cause a significant change in χ^2 and was not included in the final base model for a given source. Normalization and photon index in the PEXRAV model were tied to those of the continuum power law, abundances were set to solar, and the inclination angle (cos$i$) was frozen at 0.866 (30°), leaving only the reflection fraction R as a free parameter. Our best fit values for Γ, $N_{\rm H}$ (the column density of cold material in addition to the Galactic), R, and the Fe line equivalent width (EW) are given in Tables 3.6 and 3.7 for Seyfert 1's and 2's respectively.

In a few cases more complex models were required, specifically either partial covering absorption or scattered nuclear emission were necessary in a handful of sources. Best fit parameters for these models are shown in Table 3.8. The majority of these sources are Compton-thick Seyfert 2's, with the exception of NGC 4151. NGC 7582 and NGC 1068 may be reflection dominated source (i.e., the CRH component is as strong or stronger than the power law), however it was not possible to disentangle the absorbed power law and the CRH for these sources and modeling either partial-covering Compton-thick absorption or a dominating CRH provided a good fit. Mkn 3 and NGC 6240 have scattered nuclear emission that has been identified by Chandra (Sako et al. 2000; Lira et al. 2002). NGC 4945 was best fit by a hard X-ray power law with a Compton-thick absorber and an additional power law visible below about 10 keV due to nuclear starburst activity (see, e.g., Schurch et al. 2002 and references therein). NGC 4945 also required a high energy rollover for a good fit as discussed earlier.

Circinus is a bright, well-studied, reflection-dominated source with a very strong CRH and a Compton-thick absorber, and a soft power law component either from leaked or scattered emission. A rollover was detected in this source around ∼40 keV in our initial investigations, however using PCFABS (an XSPEC model with the covering fraction f or optical depth τ as a free parameter in addition to the column density) to model the partial covering in this source we discovered that the presence of a rollover is dependent on whether the Compton-thick absorber is modeled to cover the Compton reflection component as well (i.e., the Compton-thick absorber lies in the line of sight to the reflector). This would be the case if the reflection is arising from the disk or the inner part of the far side of the torus with the absorber further out, possibly part of the near side of the torus. Modeling the source in this manner leads to no significant detection of a rollover ($\Delta\chi^2$/dof $<$ 10 with $E_{\rm roll}$ $=120^{+220}_{-20}$). Therefore we do not include the rollover in our best fit model for this source in Table 3.8.

For Blazars our basic model was a simple power law. The best fit values for Γ and the power law normalization are listed in Table 3.9. We also tried a broken power law model for all blazars but it was only a significant improvement in fit for four objects, 1ES 1101–232, 1ES 1959+650, Mkn 421 and Mkn 501. Best fit parameters for the broken power law model for these objects are given in Table 3.10.

For almost all of the blazars in our sample a simple or broken power law gave a good description of the spectrum, however 3C 273 is something of a special case with an Fe line and Compton hump having been detected previously in this source (e.g., Grandi et al. 1997, Kataoka et al. 2002). A Compton reflection component was significant to include at the 96% confidence level but with a very low R value (0.04 ± 0.03). It was significant to include an Fe line at only the 86% confidence level with an EW of 50 ± 40 eV. This is consistent with a Seyfert-like source being diluted by the jet component in the X-ray band.

Table 3.1: Averages by Source Type

Type	Γ	R
All Seyferts	1.94	0.57
Narrow Line Seyfert 1's	2.24	0.89
Seyfert 1's	1.86	0.27
Compton-thin Seyfert 2's	1.85	0.24
Compton-thick Seyfert 2's	1.52	1.83
Blazars	2.1	-
BLLAC	2.3	-
FSRQ	1.8	-

Note – Average model parameter values for sources in our sample by type. Objects with poorly constrained parameters have been omitted when calculating these averages. Note that the high average R value for all Seyferts is due in large part to the contribution from the steep NLSy1's and reflection dominated Compton-thick sources. For typical Seyfert 1's and 2's the average R is 0.3.

3.3 Results for the Seyfert Sample

Our excavation of the *RXTE* archive has produced a unique sample of 100 AGN with spectral data from 3.5 keV to $\gtrsim$20 keV. The breadth of this energy range has allowed us to explore key spectral components that have not been well-studied to date. Most significantly, quantifying the Compton reflection hump requires sensitivity over a broad energy range which other modern X-ray observatories lack (*Chandra*, *XMM-Newton*). *RXTE*'s ability to observe the very hard X-ray properties of AGN simultaneously with their mid-range (2–10 keV) X-ray properties eliminates problems associated with non-simultaneous observing which can be particularly severe in highly variable objects.

Making use of the large sample provided by the *RXTE* archive we can examine spectral properties of different types of AGN. We have divided our sample into optically classified (per NED) Seyfert 1's, Seyfert 2's, NLSy1's, Compton-thick Seyfert 2's and blazars (which will be discussed in a following section). Average parameter values for the various Seyfert sub-types are given in Table 3.1. The distribution of Γ by object type is given in Figure 3.6 and the distributions of R and FR by type are given in Figure 3.3.

The average photon index for our entire sample of Seyferts was 1.94. For Seyfert 1's and Compton-thin Seyfert 2's the average photon indices were 1.86 and 1.79 respectively with standard deviations of $\sim$0.12. The similarity in Γ between these two classes of objects supports the Seyfert 1/2 unification schemes since we would expect the intrinsic photon indices to be unrelated to the viewing angle. They are also consistent with the values of $\sim$1.8–1.9 generally accepted to be the average range of power law photon indices in Seyferts. The Compton-thick Seyfert 2's had an average photon index of 1.77 with a standard deviation of 0.26, although for these sources it is very difficult to measure the intrinsic photon index accurately since the extreme curvature of the spectrum gives little leverage for measuring Γ.

NLSy1's had an average photon index of 2.24 (with a standard deviation of 0.24), significantly higher than other Seyferts and consistent with the idea that these objects are in a different regime of accretion (Pounds et al. 1995). If Seyfert 1's and 2's share a common central engine, we would expect to see Seyfert 2's with similar properties to NLSy1's which could not be identified optically (since the BLR is obscured in Seyfert 2's). IRAS 18325-5926 and IRAS 04575–7537 are Seyfert 2's which show very soft power laws with Γ of 2.71$\pm$0.23 and 2.48$\pm$0.22, respectively. These sources resemble NLSy1's in their X-ray spectra, and may be part of class of object that have been a missing piece in the Seyfert 1/2 unification puzzle.

We detected a strong CRH ($R \gtrsim$0.2) significant at the 5σ level in 28 of the 66 Seyferts in our sample. Only 5 showed no contribution from the CRH at all ($R < 0.1$). Thus, of the 33 sources which had enough counts enough to measure R with high significance, $\sim$85% showed at least some contribution from the CRH. The remaining 33 Seyferts did not have well measured CRH's due to a lack of counts above 10 keV and/or a weak reflection hump. Averages were calculated excluding

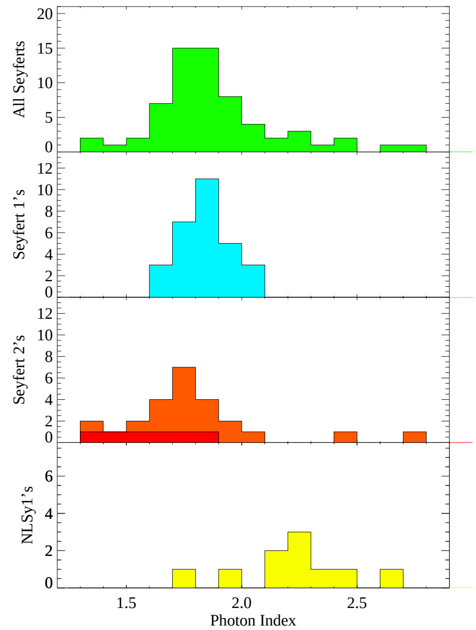

Figure 3.6: Γ distribution by Seyfert type. Seyfert 2's are divided into Compton-thin (orange) and Compton-thick (red). Note that two Seyfert 2's, IRAS 18325-5926 and IRAS 04575-7537 have X-ray characteristics similar to NLSy1's: very steep continuum, $N_{\rm H} \leq 10^{22}$ cm^{-2}, and a poorly constrained CRH. NGC 4945 is an extreme outlier and is not shown on this plot.

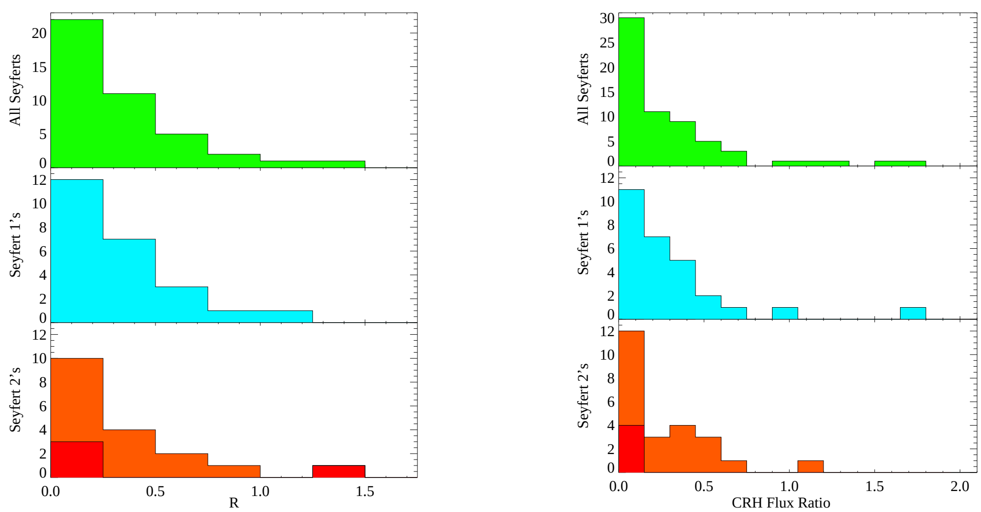

Figure 3.7: R and FR distributions by Seyfert type. Seyfert 2's are divided into Compton-thin (orange) and Compton-thick (red). NLSy1's are not included with the Seyfert 1's. Sources with only upper limits are located in the far left bin and sources without well-determined R values or with upper limits ≥0.5 are left off both plots. IRAS 18325-5926, Circinus, and NGC 7582 are extreme outliers and are not shown in these plots.

sources with poorly constrained R values, i.e., those with only upper limits that were greater than 0.5. The average reflection strength for all Seyferts was 0.57 but with a large standard deviation of 1.1. Excluding the reflection-dominated Circinus galaxy led to an overall average of 0.45 and a standard deviation of 0.76. Seyfert 1's had an average R value of 0.27 and Compton-thin Seyfert 2's had an average of 0.24, and standard deviations of 0.28 and 0.26 respectively, consistent with Seyfert 1's and 2's having on average the same amount of reflected flux.

We have also created stacked spectra for Seyfert 1's, Compton-thin Seyfert 2's and Narrow Line Seyfert 1's, including all objects weighted by exposure (excluding Cen A which dominates the Seyfert 2 stacked spectrum otherwise). Combining these into an overall X-ray SED with the correct relative abundances of different source types could give a good idea of the contribution of AGN to the cosmic X-ray background (CXB; see, e.g., Gilli et al. 2007). In particular, the distribution of NLSy1 parameters, Compton reflection strengths, and dispersion of Γ values across a sample of Seyferts could be used to fine-tune CXB models. The individual spectra used to create the stacked spectra were not put into local reference frames, however blurring of the Fe line and edge due to our including sources spanning a range of redshifts was less than the energy resolution of the PCA. These stacked spectra are shown in Figure 3.3 as νF_ν plots, giving the X-ray portion of the spectral energy distribution (SED) and clearly showing the difference in spectral shape between NLSy1's and other Seyferts.

Results of fitting the base model to these spectra yielded average photon indices of 1.85 ± 0.02, 1.77 ± 0.03 and 2.18 ± 0.08 for Seyfert 1's, 2's and NLSy1's respectively. Values of R from the stacked spectra were found to be 0.5 ± 0.1, 1.1 ± 0.1, and 1.5 ± 0.7. Note that these are significantly higher than our average values. We did not create similar stacked spectra for Compton-thick Seyfert 2's because small number of sources combined with the extreme differences in spectral shapes made them too muddled to fit with a reasonable model. Absorption in the line of sight was not significant to include in any of the sub-sets. Even though many Compton-thin Seyfert 2's show significant absorption $>10^{22}$ cm^{-2}, the soft end of the Compton-thin Seyfert 2 stacked spectrum seems to be dominated by

NGC 5506, which has a relatively high flux, long exposure time, and a very low column density. Note that we will base the remainder of our discussion on our sample averages from Table 3.1 which give equal weight to all objects and are therefore not dominated by the most-observed or brightest sources.

Figure 3.3 show the relationship between luminosity and photon index for our Seyfert sample. We do not find a significant correlation between Γ and L_{2-10} or Γ and $L_{\rm Bol}/L_{\rm Edd}$. Sobolewska & Papadakis (2009) analyzed *RXTE* monitoring data of 10 AGN and found that for a given AGN, Γ is correlated with both F_{2-10} and the mass accretion rate, $\dot{m}_{X,E}$ ($L_{2-10}/L_{\rm Edd}$), and that across their sample there was a positive correlation between Γ and $\dot{m}_{X,E}$. We do not see this trend across our entire sample of AGN. This could be due to a number of factors, for instance their objects were all quite bright and one of them, Ark 564, lies at one extreme corner of the Γ versus Eddington ratio plot in Figure 3.10. We do not find a correlation between Γ and $L_{\rm Bol}/L_{\rm Edd}$ for the other nine objects in their sample (note that our black hole masses were not identical to theirs and the happens to lessen the observed correlation as well).

3.3.1 Comparisons to Previous Surveys

Several AGN studies at high X-ray energies ($\gtrsim$10keV) have been performed recently with *BeppoSAX*, *CGRO*-OSSE, *Swift*-BAT, *INTEGRAL*-ISGRI, and *Suzaku* (Dadina 2007, Zdziarksi et al. 2000; Tueller et al. 2008; Ricci et al. 2011; and Patrick et al. 2012, respectively), particularly focusing on Seyferts.

A survey of Seyferts at high X-ray energies was done by Ricci et al. (2011) using stacked *INTEGRAL*-ISGRI data in the 17–250 keV range for different classes of Seyferts to obtain bulk spectral properties. Their average Γ and R for Seyferts 1's was 1.8 and 0.1, for Compton-thin Seyfert 2's 1.6 and 0.4, for Compton-thick Seyfert 2's 1.9 and 1.4, and for NLSy1's 2.3 and 4.2. Discrepancies between their results and ours may be due to lack of coverage below 17 keV, making it difficult to quantify the underlying power law in sources with strong Compton reflection, and modeling of the CRH (assumptions about inclination angle can change measured R values). In addition, they included high energy rollovers in most of their best-fit

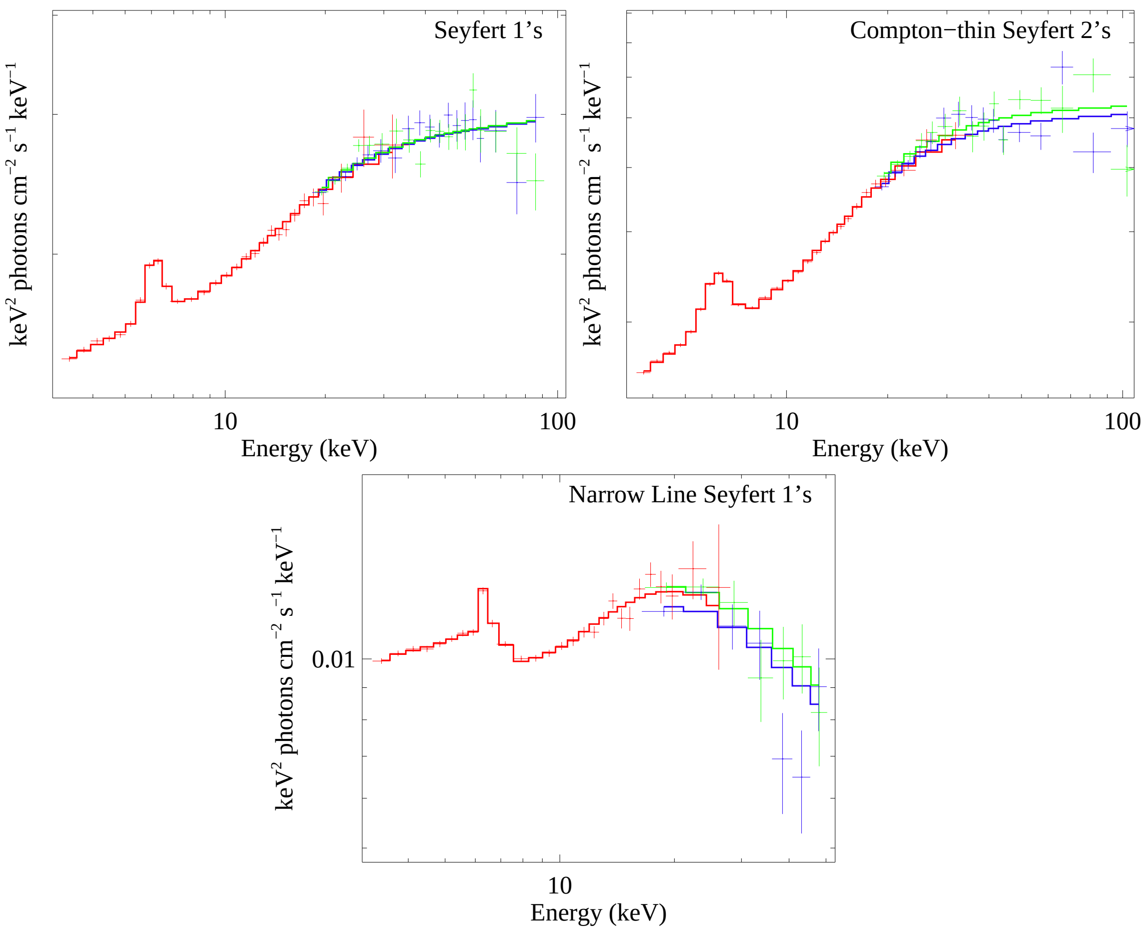

Figure 3.8: Stacked X-ray νF_ν spectra for Seyfert 1's (*top left*), Compton-thin Seyfert 2's (*top right*; excluding Cen A which is bright enough to dominate a stacked spectrum) and Narrow Line Seyfert 1's (*bottom*). The peak around 20 keV in the NLSy1's is the CRH which shows up clearly above the downward sloping power law. Red is for the PCA, blue for HEXTE-A, and green for HEXTE-B.

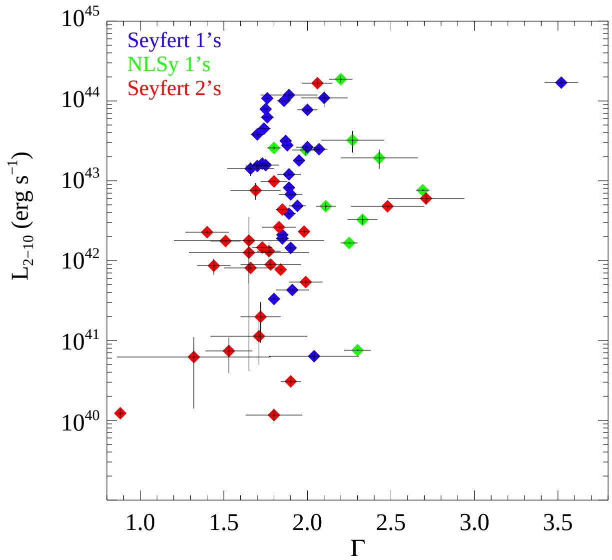

Figure 3.9: L_{2-10} vs Γ for all Seyferts. The 2–10 keV unabsorbed X-ray luminosity showed no significant correlation with the photon index.

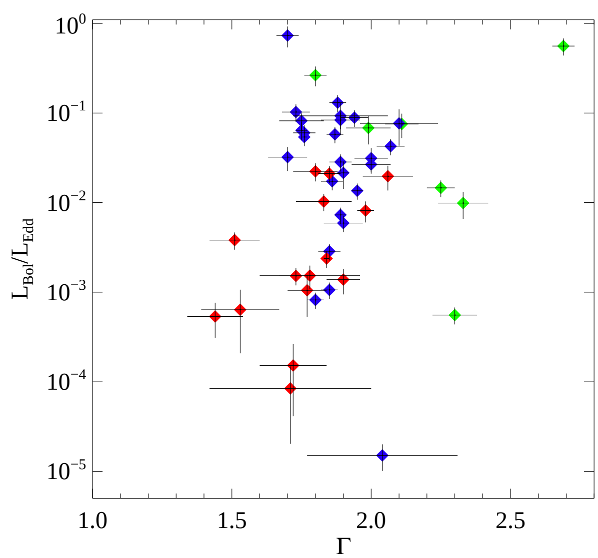

Figure 3.10: Eddington ratio versus photon index showed no significant correlation. Black hole masses were obtained for 49 sources from Vestergaard & Peterson 2006, Winter et al. 2009, and Merloni et al. 2003. Converting our X-ray luminosity to bolometric luminosity we used a rough, luminosity-dependent scaling factor, see for example Marconi et al. 2004

models, though they mainly only obtained lower limits to $E_{\rm roll}$. We did not do an extensive search for high energy rollovers in this sample since previous work has already been done with the highest quality HEXTE data (Rivers et al. 2011b) which ruled out the presence of a rollover below 200 keV in most cases.

Nandra & Pounds (1994) analyzed *Ginga* data of 27 Seyferts in the 1.5–37 keV range and found average Γ and R values of 1.95 and 1.60. Gondek et al. (1996) produced stacked spectra using combined *CGRO*-OSSE, *Ginga* and *EXOSAT* data with average values for Γ and R of 1.90 ± 0.05 and 0.76 ± 0.15. Both these samples are consistent with our average value of Γ for the entire sample of 1.9, though both showed higher values of R than our 0.54. Winter et al. (2009) found an average Γ of 1.78 with a standard deviation of 0.24 for a sample of 102 *Swift*-BAT selected AGN, however they did not model any Compton reflection.

Our *RXTE* results are consistent with previous analyses and our sample has a number of advantages over previous surveys in the medium–hard X-ray bandpass. Since the PCA and HEXTE have always operated simultaneously, we do not have the ambiguity from source variability that comes from combining non-simultaneous soft and hard X-ray data sets from different missions as is commonly necessary to obtain broadband coverage (e.g., Gondek et al. 1996). Additionally, many of these sources were monitored over long periods of time and for these sources the spectral parameters can be taken as good longterm average baselines for time-resolved spectral analysis.

3.3.2 The Circumnuclear Material

There are a number of factors that affect the shape and relative strength of the CRH: the photon index of the incident power law, the inclination angle, the covering fraction of the material relative to the illuminating source, elemental abundances, and the geometry of the reflecting material. Unfortunately, the changes in shape are very subtle and high energy spectrometers are not sensitive enough to these subtle differences to deconvolve all of these effects through spectral modeling. We therefore must make a number of assumptions and use other techniques to discern the geometry of the Compton thick material.

The PEXRAV model has been widely used to model reflection off a disk of Compton thick material such as the accretion disk. It assumes a plane of Compton-thick material covering between 0 and $\sim 2\pi$ sterradians of the sky from the point of view of the illuminating source corresponding to R between 0 and $\sim$1. However, a number of objects in our sample have reflection fractions much greater than 1, which is unphysical in this model, as is freezing the inclination angle to 30° for all objects. It may seem tempting at this point to choose more accurate inclination angles on an object by object basis, however accurate measurements are very difficult to come by. It is sometimes assumed, based on Seyfert 1/2 unification schemes, that Seyfert 1's will have smaller inclination angles (i.e. "face on" to the observer) while Seyfert 2's will have larger angles (i.e. "edge on" to the observer), but this poses a number of problems. The first is that if we assume these objects have inherent differences we will inevitably find that we are correct. For example assuming Seyfert 2's are on average at an angle of 60° will inflate the value of R by a factor of 1.2–1.5, leading to the erroneous conclusion that there is more Compton thick material surrounding (and being illuminated by) Seyfert 2's.

Additionally, this does not take into account what effect a torus may have if present. We attempted to apply the torus model MYTORUS (Murphy & Yaqoob 2009) to our data. Their model is a simple donut shape of uniform density with an opening angle of 60°. Unfortunately, the model's assumption that the torus has a uniform density leads to a steep change in the line-of-sight absorption at the edge of the donut-shaped torus, causing all Compton-thin sources to have inclination angles close to 60°. Most sources also required additional Fe line emission from Compton-thin material, which meant that the Fe line could not be used to constrain the amount of Compton-thick material in these sources. For the majority of our sources this led to two parameters, angle and torus density, to characterize only one measurable quantity: the flux of the CRH. Future spectrometers could be more sensitive to the shape of the CRH component which would allow for more thorough testing of torus models.

We concluded that the best way to proceed was with the results of the PEXRAV model, but to utilize it in a predominantly phenomenological way. Since

PEXRAV is not the only CRH model in use, we also report the flux ratios in Tables 3.6 – 3.8, the relative flux of the CRH to the underlying power law near the peak of the CRH between 15 and 50 keV, which we can use to compare to results using other models, including ionized reflectors such REFLIONX or torus models such as MYTORUS. We calculated this flux ratio (FR) by finding the 15–50 keV flux for the continuum and for the CRH, then defining $FR = F_{\mathrm{CRH}}/F_{\mathrm{Powerlaw}}$. There is a linear proportionality between FR and R for fixed values of cos$i$ and Γ. At 30$^{\mathrm{o}}$ with $\Gamma = 1.9$, we find that $FR = 0.8R$. Patrick et al. (2012) analyzed a sample of 46 Seyfert 1's observed with *Suzaku* and *Swift*-BAT and reported FR values modeled by REFLIONX. Comparing their distribution of Reflection fraction (their Figure 12) with ours shown in Figure 3.3 we see a very similar smooth distribution with the majority of objects falling below R=1 (FR=0.8) but with a long tail towards higher values. These distributions are likely not consistent with the simple disk geometry and the standard Seyfert 1/2 unification since we would expect to see more Compton reflection in face-on Seyfert 1's than in side-view Seyfert 2's which we do not observe.

Another way to probe the circumnuclear material is to try to quantify how much of it is Compton-thick material and how much is Compton-thin. We can do this by comparing the strength of the Fe line (which traces all material) with the strength of the Compton hump (which traces only Compton-thick material). George & Fabian (1991) calculated the expected flux of the Fe line produced by reflection off a Compton-thick disk with respect to the flux of the Compton hump; it's expected that the Fe line EW will be $\sim$150 eV for $R \sim 1$ at an angle of 30$^{\mathrm{o}}$. In Figure 3.3.2 we show the strength of the CRH plotted versus the EW of the Fe line for all Seyferts. Compton-thick material accounts for $\sim$40% of the Fe line flux average, however the variation is quite large. Approximately three quarters of Seyfert 1's and Compton-thin 2's show more Compton thin material than Compton thick.

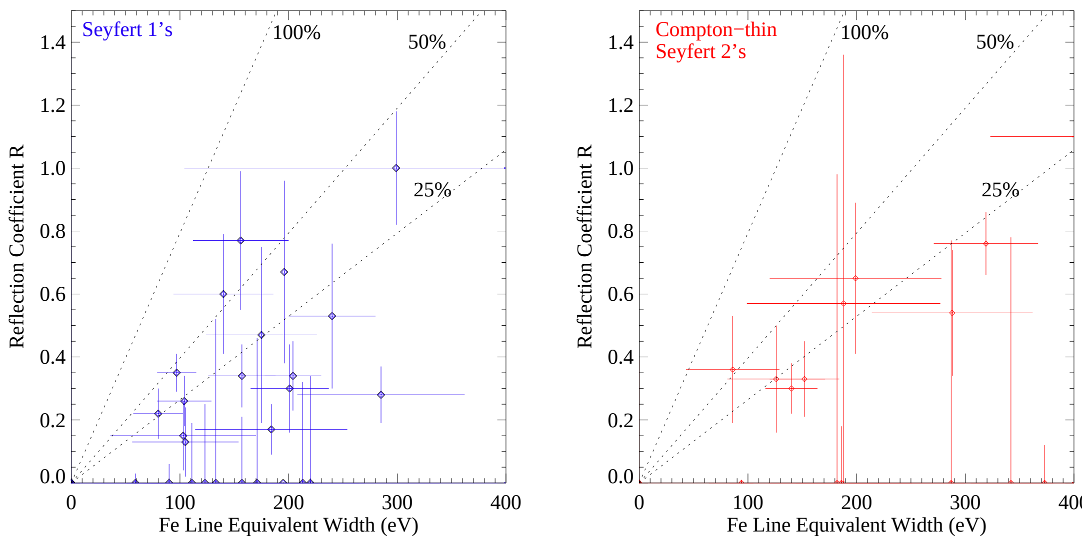

Figure 3.11: Comparing the amount of reflection, R, to the EW of the Fe Kα line for Seyfert 1's (left) and Seyfert 2's (right). The left-most dashed line is the predicted amount of Fe emission associated with reflection off Compton-thick material in a disk. Points falling the right of this line must have additional contribution from Compton thin material. The dashed lines indicate the relative amount of Fe line flux contributed by Compton-thick material.

3.3.3 High Energy Rollovers

High-energy rollovers in the power-law continua of Seyferts are expected if the power law is generated via thermal Componization of soft seed photons, most likely blackbody emission from the accretion disk, (e.g., Haardt et al. 1994, Titarchuk 1994, Poutanen & Svensson 1996, and references therein). In the simplest models, if all the electrons in the corona are at the same temperature, $T_{\rm e}$, a high-energy continuum rollover can be expected in the spectrum near an energy $\sim$3 times $k_{\rm B}T_{\rm e}$ (assuming an optical depth near unity).

Such rollovers have been detected in the X-ray spectra for many accreting Galactic black hole systems (e.g., Takahashi et al. 2008, Wilms et al. 2006, Kalemci et al. 2005, Yamaoka et al. 2005, Frontera et al. 2001). As Seyferts are generally X-ray fainter than Galactic black hole (GBH) systems, constraining rollovers their has been observationally challenging, however for sources with $\Gamma < 2$, rollovers are expected in order to prevent divergence of the total energy. In general, the rollovers found in *BeppoSAX* spectra of Seyferts reported in the literature span the range $\sim 50 - 400$ keV, with uncertainties anywhere from tens to a few hundred keV (e.g., Perola et al. 2002, Quadrelli et al. 2003) and have proven to be highly model-dependant In our *RXTE* sample, adding high-energy rollovers to our spectral models yielded mostly only lower limits to $E_{\rm roll}$, in contrast with the *BeppoSAX* results.

We detected a rollover in NGC 4945 around 70 keV, depending on the model used in Circinus around 40 keV, and, tentatively, in MR 2251–178 around 100 keV. Extra curvature in the data/model residuals when no rollover is modeled suggest that the rollovers detected in Circinus and NGC 4945 are not spurious. However, problems encountered with model degeneracies during fitting led to unexpectedly low (and likely unrealistic) values for the photon index $\Gamma_{\rm HX}$ of the absorbed hard X-ray power-law in each case. Given the extreme amount of absorption and the requirement to model an additional power-law component below $\sim$10 keV in each object, Circinus and NGC 4945 have two of the most complex spectra in our sample. Successfully deconvolving all components, and accurately constraining rollovers and Compton reflection strengths in these objects may be possible in

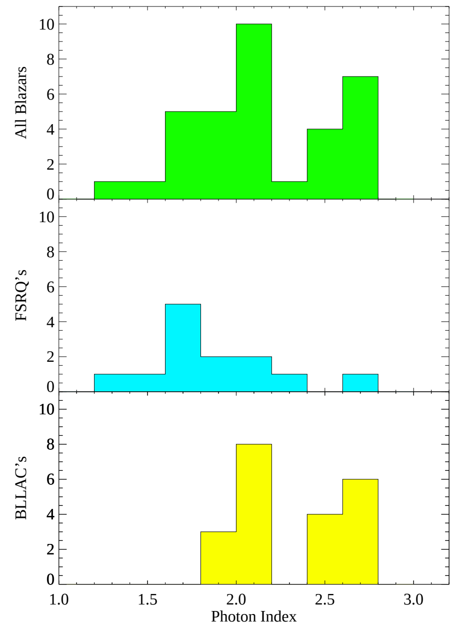

Figure 3.12: Γ distribution by blazar type. BL Lac objects tend to have higher photon indices than FSRQs.

the future via observations spanning a broad energy range and having sufficient energy resolution in the Fe K bandpass. For the purposes of this paper we have simply presented the results of model fits with and without rollovers, with the understanding for the reader that for the models with rollovers, best-fit values may have large systematic uncertainties.

For objects in which a rollover was not detected, we can be reasonably certain that the quality of our data precludes rollover energies below $\sim$ 100 keV. Excluding Cen A (which has X-ray emission likely including significant contribution by emission from a relativistic jet), the lower limits on $E_{\rm roll}$ for our objects range from 120 to 350 keV, with an average lower limit of 225 keV, which is very close to the upper limit of the HEXTE energy range. This would suggest that, on average, the electron temperatures in our Seyfert coronae must be at least $\gtrsim$75 keV.

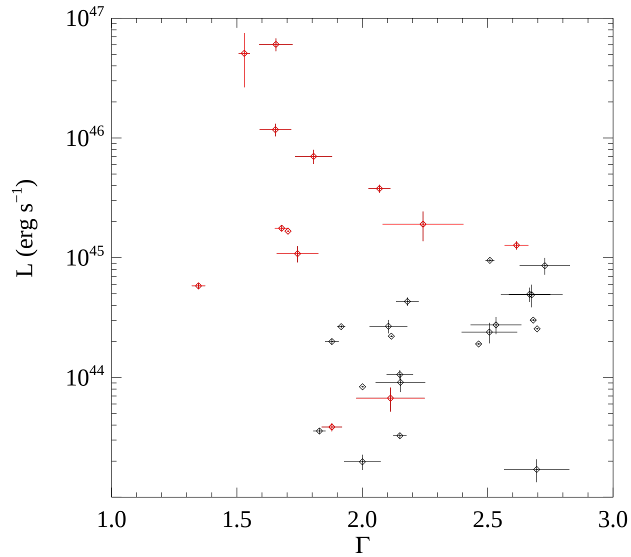

Figure 3.13: Luminosity versus photon index for the blazars in our sample. Red data points are FSRQs; black data points are BL Lac objects. We find significant negative correlation which is consistent with the Fossati sequence.

3.4 Results for the Blazar Sample

Most of the blazars in our sample were well fit by a simple power law. Four BL Lac type objects were fit better by a broken power law with break energies below ∼10keV and steepening by ∼0.2. The average Γ for our sample was 2.1 with a variance of 0.15. The average Γ for FSRQs was 1.8 while the average for BL Lac objects was 2.3 with variances of 0.2 and 0.1 respectively. The distribution of Γ for the blazar sub-types is shown in Figure 3.12.

In addition to the lower photon index, the FSRQs also tend to be much more luminous than the BL Lacs. Figure 3.13 shows the X-ray 2–10 keV luminosity (L_{2-10}) versus the photon index for our sample of blazars. We found a weak correlation between these quantities with a Pearson correlation coefficient of −0.40, significant at the 99% level. This is consistent with the"Fossati sequence" (Fossati et al. 1998) which predicts that for higher luminosities the peak of the broadband emission humps would shift to lower energies. At lower luminosities the upper end of the Synchrotron hump dominates the X-ray band while at higher luminosities the lower end of the inverse Compton hump dominates. The means a softening of the X-ray portion of the SED and an increase in the photon index as luminosity decreases. Donato et al. (2001) published a large X-ray sample of blazars observed by *BeppoSAX* confirming this trend.

3.5 Tables for Chapter 3

Table 3.2: Full Survey Source List

Source Name	Type	z	PCA (ks)	HEX-A, B (ks)	W.A.
3C 111	BLRG/Sy1	0.0485	1092	127, 278	
3C 120	BLRG/Sy1	0.0330	2102	504, 629	
3C 382	BLRG/Sy1	0.0579	154	49, 49	
3C 390.3	BLRG/Sy1	0.0561	577	158, 184	
4U 0241+61	Sy1.2	0.0440	152	50, 49	
Ark 120	Sy1	0.0327	277		
Ark 564	NLSy1	0.0247	447		
Fairall 9	Sy1	0.0470	647		
IC 4329A	Sy1.2	0.0161	573	148, 177	(1)
IRAS 13349+2438	Sy1/NLSy1	0.1076	45		(2)
MCG–2-58-22	Sy1.5	0.0469	223	68, 68	
MCG–6-30-15	NLSy1.2	0.0077	1965	505, 555	(1)
MCG+8-11-11	Sy1.5	0.0205	2		
Mkn 110	NLSy1.5	0.0353	1283		
Mkn 279	Sy1.5	0.0305	180		
Mkn 335	NLSy1	0.0258	161		
Mkn 509	Sy1.2	0.0344	738	197, 224	
Mkn 590	Sy1.2	0.0264	32		
Mkn 766	NLSy1	0.0129	771		(1)
Mkn 79	Sy1.2	0.0222	1292		
MR 2251-178	Sy1/QSO	0.0640	597	57, 144	
NGC 3227	Sy1.5	0.0039	1050	303, 304	(3)
NGC 3516	Sy1.5	0.0088	1036	291, 290	(4)
NGC 3783	Sy1	0.0097	1563	204, 393	(4)
NGC 3998	Sy1	0.0035	328		
NGC 4051	NLSy1.5	0.0023	1972		(1)
NGC 4151	Sy1.5	0.0033	562	179, 179	
NGC 4593	Sy1	0.0090	1389	167, 326	(5)
NGC 5548	Sy1.5	0.0172	1012	287, 148	(6)
NGC 7213	Sy1.5/Radio	0.0058	692		

Table 3.2: Full Survey Source List

Source Name	Type	z	PCA (ks)	HEX-A, B (ks)	W.A.
NGC 7469	Sy1.2	0.0163	1097	243, 312	
PDS 456	Sy1/QSO	0.1840	361		
PG 0052+251	Sy1.2	0.1545	170		
PG 0804+761	Sy1	0.1000	382		(7)
PG 1202+281	Sy1.2	0.1653	27		
PG 1211+143	NLSy1	0.0809	131		
Pictor A	Sy1/LINER	0.0351	34		
PKS 0558-504	NLSy1	0.1370	932		
PKS 0921-213	FSRQ/Sy1	0.0520	92		
TONS180	NLSy1	0.0620	326		
Cen A	NLRG	0.0018	913	109, 197	
Circinus	Sy2/C-thick	0.0014	103	33, 32	
Cygnus A	Sy2/Radio	0.0561	72		
ESO 103-G35	Sy2	0.0133	163	50, 49	
IC 5063	Sy2	0.0113	69		
IRAS 04575-7537	Sy2	0.0181	49		
IRAS 18325-5926	Sy2	0.0202	332		
MCG–2-40-4	Sy2	0.0252	3		
MCG–5-23-16	Sy2/NELG	0.0085	180	55, 54	
Mkn 3	Sy2	0.0135	54	15, 15	
Mkn 348	Sy2	0.0150	484	68, 59	
NGC 1052	Sy2/Radio	0.0050	399		
NGC 1068	Sy1.9/C-thick	0.0038	54		
NGC 2110	Sy2/C-thick	0.0076	194	58, 58	
NGC 2992	Sy2	0.0077	70		
NGC 4258	Sy1.9/LINER	0.0015	1463		
NGC 4388	Sy2/C-thick	0.0084	98.4		
NGC 4507	Sy2	0.0118	145	46, 46	
NGC 4945	Sy2/C-thick	0.0019	998	208, 306	
NGC 526A	Sy2/NELG	0.0192	113	35, 34	
NGC 5506	Sy1.9	0.0062	697	202, 200	
NGC 6240	Sy2/C-thick	0.0245	113		

Table 3.2: Full Survey Source List

Source Name	Type	z	PCA (ks)	HEX-A, B (ks)	W.A.
NGC 6300	Sy2	0.0037	27		
NGC 7172	Sy2	0.0087	87	26, 26	
NGC 7314	Sy1.9	0.0048	252	73, 73	
NGC 7582	Sy2/C-thick	0.0053	185	43, 44	
1ES 0229+200	BLLAC	0.1400	279		
1ES 0414+009	BLLAC	0.2870	31		
1ES 0647+250	BLLAC	0.2030	42		
1ES 1101-232	BLLAC	0.1860	194	29, 29	
1ES 1218+304	BLLAC	0.1836	10		
1ES 1727+502	BLLAC	0.0554	20		
1ES 1741+196	BLLAC	0.0840	11		
1ES 1959+650	BLLAC	0.0470	229	64, 64	
1ES 2344+514	BLLAC	0.0440	112		
1H 0323+342	FSRQ	0.0610	105		
3C 273	FSRQ	0.1583	2378	429, 616	
3C 279	FSRQ	0.5362	2222	451, 635	
3C 454.3	FSRQ	0.8590	54	13, 13	
3C 66A	BLLAC	0.4440	162		
4C 29.45	FSRQ	0.7245	159		
4C 71.07	FSRQ	2.1720	269	0, 39	
BL Lac	BLLAC	0.0686	2311		
CTA 102	FSRQ	1.0370	66		
H 1426+427	BLLAC	0.1291	468		
Mkn 180	BLLAC	0.0453	15		
Mkn 421	BLLAC	0.0300	2230	475, 481	
Mkn 501	BLLAC	0.0336	728	153, 171	
NRAO 530	FSRQ	0.9020	136		
PG 1553+113	FSRQ	0.3600	119		
PKS 0528+134	FSRQ	2.0600	247		
PKS 0548-322	BLLAC	0.0690	13		
PKS 0829+046	FSRQ	0.1737	240		

Table 3.2: Full Survey Source List

Source Name	Type	z	PCA (ks)	HEX-A, B (ks)	W.A.
PKS 1510-089	FSRQ	0.3600	2091	260, 387	
PKS 1622-297	FSRQ	0.8150	123		
PKS 2005-489	BLLAC	0.0710	400	96, 105	
PKS 2126-158	FSRQ	3.2680	34		
PKS 2155-304	BLLAC	0.1160	902		
RGB J0710+591	BLLAC	0.1250	16		
S 50716+714	BLLAC	0.3000	656		

Note – Source names in bold indicate objects included in broad sample of 23 AGN. Combined HEXTE-A and B exposure times are given only for objects where those data were included in our spectral analysis. "NLRG," or "Radio" indicates the object is radio loud. "C-thick" indicates a known Compton-thick object. "NELG" indicates a Narrow Emission Line Galaxy. W.A. lists references for the warm absorber parameters we used: (1) McKernan et al. (2007), (2) Blustin et al. (2005), (3) Markowitz et al. (2009), (4) Netzer et al. (2003), (5) Steenburgge et al. (2003), (6) Steenburgge et al. (2005) and (7) Pounds et al. (2003)

Table 3.3: The 20–100 keV band

Source	Γ	F_{20-100} HEXTE-A (10^{-10} erg s^{-1})	F_{20-100} HEXTE-B (10^{-10} erg s^{-1})	% of Background A, B	χ^2/dof
3C 111	1.8±0.1	0.82	0.81	1.6, 1.6	48/47
3C 120	1.78±0.06	0.80	0.75	1.3, 1.4	62/47
IC 4329A	1.89±0.04	1.91	1.92	4.0, 4.5	140/49
Mkn 509	1.87±0.09	0.80	0.73	1.4, 1.5	51/37
MR 2251–178	1.8±0.2	0.70	0.71	0.9, 1.0	20/23
NGC 3227	1.77±0.08	0.76	0.76	1.2, 1.4	53/39
NGC 3516	1.8±0.1	0.89	0.91	1.1, 1.2	51/29
NGC 3783	1.82±0.05	1.19	1.29	1.9, 2.2	90/43
NGC 4151	1.84±0.02	4.45	4.58	6.2, 6.4	536/53
NGC 4593	1.76±0.09	0.70	0.66	1.4, 1.4	52/37
NGC 5548	1.79±0.08	0.78	0.79	1.1, 1.1	53/33
NGC 7469	1.8±0.2	0.47	0.51	0.7, 0.8	29/31
Cen A	1.78±0.01	6.02	7.38	9.9, 13.7	62/53
Circinus	1.72±0.07	2.02	2.16	2.6, 2.9	259/35
MCG–5-23-16	1.9±0.1	1.48	1.52	1.9, 1.9	56/35
NGC 4507	1.6±0.1	1.33	1.73	1.7, 1.7	40/35
NGC 4945	1.32±0.03	1.77	1.80	3.4, 3.9	894/53
NGC 5506	1.87±0.04	1.75	1.74	2.2, 2.3	194/37
NGC 7582	1.8±0.3	0.58	0.60	1.5, 1.5	30/13
1ES 1959+650	2.32±0.08	0.78	0.81	1.9, 2.2	47/45
3C 273	1.74±0.02	1.80	1.98	2.9, 3.5	79/53
3C 454.3	1.5±0.3	0.64	0.46	1.7, 1.4	9/20
Mkn 421	2.70±0.04	1.11	1.04	2.3, 2.2	47/41

Note – These are results for simple power-law fits to the 20–100 keV band only using data from both HEXTE clusters. Γ is tied between HEXTE-A and -B for all objects.

Table 3.4: Broad Sample Fitting Results

Source Name	Γ	R	$F_{2-10}{}^{A}$	$F_{20-100}{}^{A}$	$L_{2-10}{}^{B}$	$L_{20-100}{}^{B}$
3C 111	1.67±0.01	...	5.21	8.66	2.73×10^{44}	4.27×10^{44}
3C 120	1.82±0.03	0.24±0.06	5.30	7.52	1.16×10^{44}	1.40×10^{44}
IC 4329A	1.88±0.02	0.39±0.05	13.97	19.37	7.42×10^{43}	7.65×10^{43}
Mkn 509	1.75±0.02	0.15±0.05	5.77	8.75	1.32×10^{44}	1.81×10^{44}
MR 2251–178	1.63±0.02	...	4.46	6.25	3.78×10^{44}	5.32×10^{44}
NGC 3227	1.79±0.04	0.41±0.09	4.11	7.49	2.34×10^{42}	2.84×10^{42}
NGC 3516	1.82±0.04	0.31±0.09	4.45	8.80	1.02×10^{43}	1.24×10^{43}
NGC 3783	1.86±0.03	0.41±0.08	7.34	12.12	1.39×10^{43}	1.57×10^{43}
NGC 4151	1.90±0.02	0.7±0.1	16.92	43.48	5.14×10^{43}	4.64×10^{42}
NGC 4593	1.85±0.03	0.34±0.09	4.19	6.29	9.27×10^{42}	1.16×10^{43}
NGC 5548	1.72±0.02	0.13±0.04	5.97	8.57	3.88×10^{43}	4.94×10^{43}
NGC 7469	1.88±0.04	0.4±0.1	3.33	4.53	1.47×10^{43}	1.57×10^{43}
Cen A	1.83±0.01	...	28.42	66.01	8.59×10^{41}	1.08×10^{42}
Circinus	2.01±0.06	0.53±0.04	2.63	20.62	2.22×10^{41}	3.13×10^{41}
MCG–5-23-16	1.84±0.03	0.4±0.1	9.60	16.00	2.03×10^{43}	2.35×10^{43}
NGC 5506	1.93±0.03	1.2±0.1	10.65	16.88	1.01×10^{43}	9.70×10^{42}
NGC 4507	1.72±0.04	0.4±0.1	1.43	14.94	2.41×10^{43}	4.05×10^{43}
NGC 4945	1.71±0.03	0.24±0.05	0.61	19.89	1.15×10^{41}	4.02×10^{41}
NGC 7582	1.79±0.10	$3.3^{+1.6}_{-0.9}$	1.04	5.62	6.03×10^{41}	7.24×10^{41}
1ES 1959+650	2.12 ± 0.01^{C}	...	15.48	9.37	1.17×10^{45}	7.02×10^{44}
3C 273	1.69±0.01	0.07±0.03	11.90	19.92	7.23×10^{45}	1.15×10^{46}
3C 454.3	1.67±0.05	...	7.41	13.05	2.06×10^{47}	3.60×10^{47}
Mkn 421	2.79 ± 0.01^{C}	...	40.00	10.14	8.63×10^{44}	2.18×10^{44}

Note – All selected sources with type, best fit photon index (Γ) and Compton reflection strength (R), long-term average 2–10 keV and 20–100 keV observed fluxes and long-term average 2–10 keV and 20–100 keV unabsorbed, rest frame luminosities. Γ values for Mkn 421 and 1ES 1959+650 are for hard X-ray power law (above $\sim$8 keV). ^{A} ($10^{-11}\,\mathrm{erg\,cm^{-2}\,s^{-1}}$) ^{B} ($\mathrm{erg\,s^{-1}}$)

Table 3.5: Rollover Models

Source	Γ	A^1 (10^{-2})	$N_{\rm H}$ ($10^{22}\,{\rm cm}^{-2}$)	$\Gamma_{\rm SXPL}{}^2$	$A_{\rm SXPL}{}^2$ (10^{-2})	Fe Line E (keV)	σ (keV)	$I_{\rm Fe}$ (10^{-4}) (ph cm^{-2}s^{-1})	R	$E_{\rm roll}{}^3$ (keV)	χ^2/dof
MR 2251–178	1.56±0.03	$0.91^{+0.03}_{-0.07}$				$6.2^{+0.3}_{-0.6}$	0.8±0.6	0.8±0.5	<0.06	100^{+40}_{-30}	65.8/47
Circinus	1.2±0.2	$1.2^{+0.9}_{-0.6}$	920^{+120}_{-150}	2.5±0.4	1.1±0.4	6.42±0.01	0.20±0.04	5.2±0.1	1.1± 0.3	41^{+6}_{-10}	47.1/62
NGC 4945	1.0±0.1	$0.24^{+0.27}_{-0.05}$	468^{+30}_{-14}	$2.1^{+0.6}_{-0.1}$	0.5±0.2	6.5±0.1	0.4±0.2	0.8±0.2	<0.03	70^{+10}_{-10}	90.6/80

Note – Parameters for the best fit rollover models in sources where an improvement in fit was found.

Table 3.6: Seyfert 1's: Base Model Fit Parameters

Source Name	$\mathrm{Flux}_{2-10}{}^{A}$	Γ	N_{H} ($10^{22}\mathrm{cm}^{-2}$)	EW (eV)	R	FR	χ^2/dof
3C 111	49.1 ± 0.4	1.75 ± 0.02		90 ± 20	≤ 0.1	≤ 0.1	39/50
3C 120	37.9 ± 0.7	1.88 ± 0.03		190 ± 70	0.17 ± 0.07	0.2 ± 0.1	42/50
3C 382	44.4 ± 0.4	1.86 ± 0.04		105 ± 50	0.13 ± 0.10	0.1 ± 0.1	26/54
3C 390.3	29.4 ± 0.2	1.76 ± 0.04		100 ± 70	0.2 ± 0.1	0.2 ± 0.1	31/54
4U 0241+61	34.5 ± 0.2	1.74 ± 0.04		200 ± 40	0.3 ± 0.1	0.3 ± 0.2	67/54
Ark 120	34.5 ± 0.3	2.07 ± 0.05		240 ± 40	0.5 ± 0.2	0.5 ± 0.2	5/28
Ark 564	18.5 ± 0.3	2.69 ± 0.04		220 ± 120	-	-	6/20
Fairall 9	17.7 ± 0.2	2.00 ± 0.07		180 ± 50	0.5 ± 0.3	0.4 ± 0.3	5/28
IC4329A	102.6 ± 0.4	1.95 ± 0.02		100 ± 20	0.4 ± 0.1	0.3 ± 0.1	69/48
IRAS 13349+2438	4.0 ± 0.2	2.27 ± 0.19		460 ± 460	-	-	11/27
MCG–2-58-22	25.7 ± 0.2	1.70 ± 0.04		160 ± 30	≤ 0.2	≤ 0.2	47/54
MCG–6-30-15	41.6 ± 0.3	2.25 ± 0.05		190 ± 40	1.5 ± 0.3	1.2 ± 0.3	45/54
MCG+8-11-11	53.8 ± 0.9	1.70 ± 0.07		210 ± 60	≤ 0.3	≤ 0.3	15/27
Mkn 110	30.9 ± 0.2	1.80 ± 0.04		65 ± 20	0.14 ± 0.11	0.1 ± 0.1	34/28
Mkn 279	19.2 ± 0.3	1.89 ± 0.07		170 ± 60	≤ 0.5	≤ 0.4	15/28
Mkn 335	10.7 ± 0.2	2.11 ± 0.06		190 ± 70	-	-	37/21
Mkn 509	39.5 ± 0.2	1.87 ± 0.03		80 ± 20	0.2 ± 0.1	0.2 ± 0.1	46/54
Mkn 590	33.4 ± 0.5	1.75 ± 0.08		130 ± 70	≤ 0.5	≤ 0.5	16/27
Mkn 766	27.8 ± 0.1	2.33 ± 0.09		1900 ± 950	0.9 ± 0.4	0.7 ± 0.3	26/20
Mkn 79	20.3 ± 0.2	1.90 ± 0.07		200 ± 40	0.7 ± 0.3	0.6 ± 0.3	26/28
MR 2251–178	39.1 ± 0.3	1.76 ± 0.01		60 ± 40	≤ 0.0	≤ 0.0	42/53
NGC 3227	32.2 ± 0.2	1.80 ± 0.03		160 ± 30	0.3 ± 0.1	0.3 ± 0.1	33/54
NGC 3516	36.2 ± 0.3	1.85 ± 0.04		160 ± 40	0.8 ± 0.2	1.7 ± 0.2	43/53
NGC 3783	60.9 ± 1.0	1.89 ± 0.04		290 ± 80	0.3 ± 0.1	0.3 ± 0.1	52/42
NGC 3998	7.7 ± 1.0	2.04 ± 0.27		≤ 390	≤ 1.1	≤ 0.0	50/23
NGC 4051	21.1 ± 1.8	2.30 ± 0.08		140 ± 40	2.0 ± 0.8	1.6 ± 0.7	10/28
NGC 4151	164.4 ± 0.9	1.88 ± 0.01	21.2 ± 1.0	118 ± 88	1.3 ± 0.1	1.2 ± 0.1	$100/61^{B}$
NGC 4593	38.4 ± 0.3	1.85 ± 0.03		200 ± 30	0.3 ± 0.1	0.3 ± 0.1	51/54
NGC 5548	41.1 ± 0.2	1.89 ± 0.02		105 ± 25	0.3 ± 0.1	0.3 ± 0.1	46/54
NGC 7469	27.1 ± 0.3	1.94 ± 0.05		140 ± 50	0.6 ± 0.2	0.5 ± 0.2	47/44
PDS 456	7.0 ± 0.1	3.52 ± 0.10		580 ± 320	-	-	10/24
PG 0052+251	7.3 ± 0.1	1.89 ± 0.17		≤ 590	≤ 1.4	≤ 1.3	8/27
PG 0804+761	11.2 ± 0.2	2.00 ± 0.06		120 ± 60	≤ 0.3	≤ 0.2	8/28
PG 1202+281	5.9 ± 0.2	2.10 ± 0.14		200 ± 140	-	-	6/21
PG 1211+143	5.5 ± 0.1	1.99 ± 0.08		190 ± 90	-	-	14/28
Pictor A	19.8 ± 0.4	1.73 ± 0.05		110 ± 60	≤ 0.2	≤ 0.2	14/26
PKS 0558–504	14.8 ± 0.2	2.20 ± 0.07		≤ 105	≤ 0.5	≤ 0.4	27/19
PKS 0921–213	7.8 ± 0.2	1.66 ± 0.14		≤ 190	≤ 0.8	≤ 0.8	6/28
TONS180	7.4 ± 0.1	2.43 ± 0.23		360 ± 300	≤ 2.0	≤ 1.5	8/20

Note – Best fit parameters for Seyfert 1's with the base model. Listed are the 2–10 keV flux, photon index, column density above the Galactic, equivalent width of the Fe Kα line, the reflection strength as determined by PEXRAV, the flux ratio of the reflection to the continuum in the 15–50 keV range, and χ^2/dof. The "-" symbol represents a parameter which was unconstrained and/or not included in the modeling.

Table 3.7: Seyfert 2's: Base Model Fit Parameters

Source Name	$Flux_{2-10}{}^A$	Γ	$N_{\rm H}$ (10^{22}cm^{-2})	EW (eV)	R	FR	χ^2/dof
Cen A	280.7 ± 5.5	1.84 ± 0.01	16.2 ± 0.3	95 ± 10	≤ 0.01	≤ 0.04	134/52
Circinus	22.9 ± 0.8	1.57 ± 0.03	-	1520 ± 30	6.5 ± 0.6	6.8 ± 0.7	$786/53^B$
Cygnus A	78.7 ± 8.9	2.06 ± 0.09	7.1 ± 2.7	370 ± 70	≤ 0.1	≤ 0.1	11/26
ESO 103-G35	22.0 ± 0.3	1.83 ± 0.10	28.3 ± 2.1	290 ± 70	0.5 ± 0.2	0.5 ± 0.2	44/53
IC 5063	12.2 ± 0.2	1.65 ± 0.36	31.7 ± 11.3	180 ± 120	≤ 1.0	≤ 1.0	11/25
IRAS 04575-7537	21.7 ± 1.4	2.48 ± 0.22	3.6 ± 2.6	≤ 350	$1.5^{+2.9}_{-0.9}$	$1.1^{+2.0}_{-0.6}$	9/25
IRAS 18325–5926	21.5 ± 0.2	2.71 ± 0.23		820 ± 270	4.5 ± 3.3	3.1 ± 2.3	8/20
MCG–2-40-4	17.6 ± 0.7	1.69 ± 0.15	-	340 ± 220	≤ 0.8	≤ 0.8	16/27
MCG–5-23-16	89.4 ± 1.3	1.85 ± 0.04	3.7 ± 0.8	140 ± 20	0.3 ± 0.1	0.3 ± 0.1	40/52
Mkn 3	7.0 ± 1.6	1.43 ± 0.15	90.6 ± 7.3	$230, \pm 70$	0.4 ± 0.3	0.5 ± 0.4	$100/53^B$
Mkn 348	11.6 ± 0.2	1.51 ± 0.09	17.3 ± 2.1	125 ± 45	0.3 ± 0.2	0.4 ± 0.2	45/53
NGC 1052	5.9 ± 0.1	1.71 ± 0.29	13.6 ± 5.2	190 ± 90	≤ 1.6	≤ 1.6	41/24
NGC 1068	7.6 ± 5.6	1.60 ± 0.22	-	1880 ± 130	≤ 2.0	≤ 2.1	$27/21^B$
NGC 2110	37.5 ± 0.6	1.73 ± 0.06	6.0 ± 1.2	190 ± 40	≤ 0.2	≤ 0.2	30/53
NGC 2992	22.3 ± 2.0	1.78 ± 0.18	-	290 ± 90	≤ 0.8	≤ 0.7	12/27
NGC 4258	7.7 ± 1.5	1.80 ± 0.17	8.4 ± 3.9	≤ 250	≤ 0.4	≤ 0.4	6/27
NGC 4388	45.2 ± 1.8	1.09 ± 0.08	-	270 ± 30	≤ 0.1	≤ 0.1	79/20
NGC 4507	14.0 ± 3.0	1.77 ± 0.07	86.8 ± 2.9	150 ± 30	0.3 ± 0.1	0.3 ± 0.1	78/52
NGC 4945	4.4 ± 0.2	1.16 ± 0.02	-	-	19 ± 2	17 ± 5	$1488/53^B$
NGC 526A	39.5 ± 1.0	1.80 ± 0.08	4.6 ± 1.6	90 ± 40	0.4 ± 0.2	0.3 ± 0.2	47/53
NGC 5506	86.4 ± 0.4	1.98 ± 0.03	-	320 ± 50	0.8 ± 0.1	0.7 ± 0.1	84/53
NGC 6240	4.1 ± 2.1	1.45 ± 0.18	-	≤ 140	10^{+12}_{-4}	10^{+11}_{-4}	$36/27^B$
NGC 6300	6.2 ± 0.1	1.32 ± 0.46	14.9 ± 7.6	450 ± 120	≤ 4.3	≤ 4.2	8/27
NGC 7172	15.9 ± 0.6	1.66 ± 0.16	16.2 ± 3.4	180 ± 110	≤ 0.4	≤ 0.4	61/53
NGC 7213	18.9 ± 0.7	1.91 ± 0.10	-	220 ± 45	≤ 0.3	≤ 0.3	30/19
NGC 7314	34.6 ± 2.1	1.99 ± 0.10	-	200 ± 80	0.6 ± 0.2	0.6 ± 0.2	39/53
NGC 7582	10.5 ± 5.4	1.70 ± 0.10	13.3 ± 2.6	340 ± 70	2.7 ± 0.9	2.7 ± 0.0	$38/53\ ^B$

Note – Best fit parameters for Seyfert 2's with the base model. Listed are the 2–10 keV flux, photon index, column density above the Galactic, equivalent width of the Fe Kα line, the reflection strength as determined by PEXRAV, the flux ratio of the reflection to the continuum in the 15–50 keV range, and χ^2/dof. The "-" symbol represents a parameter which was unconstrained and/or not included in the modeling.

Table 3.8: Complex Models for Seyferts: Partial Covering and Scattered Emission

Source Name	Flux_{2-10}	Γ	N_{H} ($10^{22}\mathrm{cm}^{-2}$)	N_{H} PC ($10^{22}\mathrm{cm}^{-2}$)	f	τ	EW (eV)	R	χ^2/dof
NGC 4151	175 ± 24	1.90 ± 0.02	≤ 13.6	50^{+50}_{-10}	0.56 ± 0.20	-	299^{+251}_{-139}	1.0 ± 0.2	67/60
Circinus	23.2 ± 2.7	1.90 ± 0.06	-	430^{+60}_{-50}	0.65 ± 0.02	-	1779^{+171}_{-143}	5.8 ± 1.6	57/52
Mkn 3	7.6 ± 1.7	1.44 ± 0.10	-	130^{+4}_{-12}	-	0.05 ± 0.01	564^{+141}_{-141}	≤ 0.19	44/52
NGC 1068	7.6 ± 5.6	1.53 ± 0.14	-	1354^{+19714}_{-784}	$0.70^{+0.30}_{-0.40}$	-	≤ 4302	≤ 0.87	22/20
NGC 4388	47.5 ± 16.9	1.40 ± 0.13	-	92^{+8}_{-21}	$0.48^{+0.10}_{-0.07}$	257^{+37}_{-67}	≤ 0.20		25/19
NGC 6240	4.3 ± 2.2	1.65 ± 0.45	-	200^{+10}_{-80}	-	$0.17^{+0.13}_{-0.04}$	139^{+32}_{-139}	≤ 2.90	22/28
NGC 7582	10.4 ± 6.0	1.75 ± 0.12	16.5 ± 3.9	230^{+150}_{-120}	0.31 ± 0.15	-	324^{+74}_{-89}	$1.3^{+0.6}_{-0.4}$	38/51
	Γ_{SB}	A_{SB} (10^{-3})	Γ_{AGN}	A_{AGN} (10^{-3})	N_{H}	E_{roll}	EW (eV)	R	χ^2/dof
NGC 4945	$2.06^{+0.6}_{-0.1}$	$2.0^{+0.4}_{-1.0}$	0.88 ± 0.12	2.6 ± 0.8	425 ± 25	59 ± 7	1420 ± 120	≤ 0.1	39/51

Note – Best fit parameters for Seyferts requiring complex modeling. For sources requiring partial covering, the covering factor, f, is given. For sources with identified scattered nuclear emission from an extended medium around the AGN the optical depth, τ, is given. NGC 4945 also requires a high energy rollover modeled by HIGHECUT with a rollover energy, E_{roll}, defined as the energy at which the continuum is $1/e$ times the initial value. The "-" symbol represents a parameter which was unconstrained and/or not included in the modeling. Flux is in units of 10^{-12} erg cm^{-2} s^{-1}.

Table 3.9: Blazars: Power-Law Model Parameters

Source Name	$\mathrm{Flux}_{2-10}{}^{A}$	Γ	A (10^{-2})	χ^2/dof
1ES 0229+200	15.1 ± 0.8	1.88 ± 0.03	0.49 ± 0.02	37/25
1ES 0414+009	8.8 ± 1.9	2.68 ± 0.12	0.90 ± 0.19	14/22
1ES 0647+250	17.8 ± 2.4	2.67 ± 0.08	1.79 ± 0.25	19/21
1ES 1101–232	40.7 ± 1.3	2.51 ± 0.02	3.29 ± 0.10	$74/54^{B}$
1ES 1218+304	12.1 ± 2.0	2.53 ± 0.10	1.01 ± 0.17	8/16
1ES 1727+502	9.5 ± 1.4	2.00 ± 0.07	0.37 ± 0.05	11/23
1ES 1741+196	19.1 ± 3.3	2.15 ± 0.10	0.93 ± 0.16	6/17
1ES 1959+650	148.3 ± 1.9	2.12 ± 0.01	6.83 ± 0.09	$71/59^{B}$
1ES 2344+514	25.0 ± 1.2	2.15 ± 0.03	1.21 ± 0.06	30/28
1H 0323+342	15.3 ± 1.2	1.88 ± 0.04	0.50 ± 0.04	28/24
3C 273	98.5 ± 1.0	1.70 ± 0.00	2.43 ± 0.02	72/60
3C 279	9.1 ± 0.5	1.68 ± 0.03	0.22 ± 0.01	146/59
3C 454.3	66.7 ± 3.1	1.63 ± 0.02	1.47 ± 0.07	28/53
3C 66A	6.4 ± 1.0	2.73 ± 0.10	0.70 ± 0.11	14/15
4C 29.45	3.1 ± 0.5	1.74 ± 0.08	0.08 ± 0.01	27/24
4C 71.07	16.0 ± 7.7	1.53 ± 0.02	0.30 ± 0.14	45/37
BL Lac	11.2 ± 0.5	1.83 ± 0.02	0.34 ± 0.02	93/33
CTA 102	9.7 ± 1.3	1.81 ± 0.07	0.28 ± 0.04	30/28
H 1426+427	23.6 ± 0.7	1.92 ± 0.02	0.81 ± 0.02	18/28
Mkn 180	12.3 ± 2.7	2.70 ± 0.13	1.28 ± 0.28	8/14
Mkn 421	419.4 ± 5.6	2.70 ± 0.01	43.86 ± 0.58	$283/57^{B}$
Mkn 501	109.6 ± 1.1	2.00 ± 0.01	4.26 ± 0.04	$76/59^{B}$
NRAO 530	3.5 ± 1.0	2.24 ± 0.16	0.19 ± 0.05	8/14
PG 1553+113	14.5 ± 1.2	2.61 ± 0.05	1.36 ± 0.11	18/28
PKS 0528+134	4.1 ± 0.5	1.65 ± 0.06	0.09 ± 0.01	21/28
PKS 0548–322	32.9 ± 3.0	2.15 ± 0.05	1.59 ± 0.15	12/28
PKS 0829+046	3.3 ± 0.8	2.11 ± 0.14	0.15 ± 0.03	22/17
PKS 1510–089	6.7 ± 0.4	1.35 ± 0.03	0.09 ± 0.01	111/59
PKS 1622–297	8.4 ± 0.6	2.07 ± 0.04	0.36 ± 0.03	29/28
PKS 2005–489	56.0 ± 0.9	2.46 ± 0.01	4.25 ± 0.07	40/54
PKS 2126–158	8.4 ± 1.0	1.66 ± 0.07	0.19 ± 0.02	12/25
PKS 2155–304	33.2 ± 0.6	2.68 ± 0.01	3.40 ± 0.07	24/19
RGB J0710+591	40.9 ± 3.4	2.18 ± 0.05	2.07 ± 0.17	25/32
S5 0716+714	3.9 ± 0.8	2.51 ± 0.11	0.32 ± 0.06	17/13

Note – Best fit parameters for blazars fit with the simple power law model. The normalization of the power law, A, is defined as ph $\mathrm{keV^{-1}\,cm^{-2}\,s^{-1}}$ at 1 keV.

Table 3.10: Blazars: Broken Power-Law Model Parameters

Source Name	Γ_1	Γ_2	A (10^{-2})	E_{break} (keV)	χ^2/dof
1ES 1101-232	2.31 ± 0.20	2.56 ± 0.06	2.49 ± 0.63	4.6 ± 1.5	55/52
1ES 1959+650	1.99 ± 0.07	2.14 ± 0.01	5.70 ± 0.52	4.9 ± 0.6	34/57
Mkn 421	2.41 ± 0.09	2.75 ± 0.01	26.01 ± 3.81	6.6 ± 0.4	73/55
Mkn 501	1.97 ± 0.02	2.02 ± 0.01	4.04 ± 0.11	6.9 ± 1.2	55/57

Note – Best fit parameters for blazars with the broken power law model. The normalization, A is defined as ph keV^{-1} cm^{-2} s^{-1} at the break energy. All show significant improvement in the fit over a simple power law, though 1ES 1101-232 has a break energy very close to the edge of the bandpass and should be treated with caution.

Table 3.11: Other AGN in the *RXTE* Archive

Source Name	Type	PCA Exposure (ks)	$Flux_{2-10}$ (10^{-12} erg cm^{-2} s^{-1})	Γ
Seyfert 1's				
H 0147-537	QSO	83.3	2.7 ± 0.1	1.9 ± 0.2
H 0707-495	NLSy1	7.8	4.3 ± 1.7	3.5 ± 0.5
LBQS 2212–1759	BALQSO	18.3	$1.4^{+0.1}_{-0.4}$	2.3 ± 0.5
PG 1116+215	Sy1	51.1	3.5 ± 0.1	1.83 ± 0.11
PG 1416–129	Sy1.2	22.4	3.7 ± 2.4	1.5 ± 0.3
PG 1440+356	NLSy1	27.9	$3.2^{+0.1}_{-0.3}$	2.8 ± 0.3
PG 1700+518	BALQSO	27.4	< 0.2	-
RHS 03	Sy1	7.0	8.2 ± 6.3	1.9 ± 0.2
RHS 15	Sy1	9.8	2.6 ± 0.2	1.0 ± 0.2
RHS 17	Sy1	9.9	7.5 ± 1.6	1.6 ± 0.2
RHS 54	Sy1	7.4	$1.8^{+0.2}_{-0.6}$	1.2 ± 0.5
RHS 56	NLSy1	10.2	5.8 ± 0.8	2.2 ± 0.2
RHS 61	Sy1	8.9	4.8 ± 1.7	1.9 ± 0.3
TON1542	Sy1	90.9	3.8 ± 0.1	2.0 ± 0.1

Table 3.11: Other AGN in the *RXTE* Archive

Source Name	Type	PCA Exposure (ks)	Flux_{2-10} (10^{-12} erg cm^{-2} s^{-1})	Γ
Seyfert 2's				
Arp 220	Sy2/ULIRG	0.9	< 1.5	-
E 253-G3	Sy2	1.7	3.7 ± 3.7	0.9 ± 0.6
IRAS F00521–7054	Sy2	1.5	$4.2^{+0.4}_{-2.1}$	1.6 ± 0.5
IRAS F01475–0740	Sy2/ULIRG	3.0	< 1.3	-
IRAS F03362–1642	Sy2	1.8	< 1.3	-
IRAS F04385–0828	Sy2	1.9	$4.7^{+0.5}_{-2.8}$	1.6 ± 0.4
IRAS F05189–2524	Sy2/ULIRG	1.4	< 3.3	$1.9^{+0.9}_{-0.8}$
IRAS F08572+3915	Sy2/ULIRG	3.4	< 2.7	1.9 ± 0.7
IRAS F19254–7245	Sy2	1.8	< 1.5	-
MCG–3-34-63	Sy2	1.8	1.8 ± 1.8	-
NGC 1320	Sy2	3.4	< 0.9	-
NGC 1386	Sy2	2.5	5.8 ± 2.3	2.7 ± 1.0
NGC 3281	Sy2/C-thick	11.4	8.0 ± 2.4	2.6 ± 1.5
NGC 3660	Sy1.8	3.2	< 2.0	$1.8^{+0.9}_{-0.8}$
NGC 5347	Sy2	3.2	< 1.8	$1.7^{+1.0}_{-0.9}$
NGC 6251	Sy2	148	$3.2 \pm$	2.38 ± 0.23
NGC 6394	Sy2	23.8	< 1.9	-
NGC 6890	Sy1.9	2.5	1.1 ± 0.3	0.9 ± 1.3
TOL 1238–364	Sy2	1.7	< 1.4	$2.9^{+3.1}_{-1.7}$
Blazars				
0420-014	BLLAC	1.0	¡2.8	-
1ES 0806+524	BLLAC	39.4	$5.6^{+0.3}_{-0.8}$	2.8 ± 0.2
3C 446	BLLAC	40.5	¡1.5	2.0 ± 0.6
4C 38.41	FSRQ	65.5	$1.7^{+0.2}_{-0.5}$	1.45 ± 0.30
H 2356-309	BLLAC	2.2	8^{+2}_{-7}	2.4 ± 0.5
O J287	BLLAC	116.8	< 0.2	-
PG 1424+240	BLLAC	32.0	$2.6^{+0.1}_{-0.4}$	3.6 ± 0.5
PKS 0235+164	BLLAC	247.5	$1.6^{+0.3}_{-0.8}$	2.5 ± 0.3

Table 3.11: Other AGN in the *RXTE* Archive

Source Name	Type	PCA Exposure (ks)	Flux_{2-10} (10^{-12} erg cm^{-2} s^{-1})	Γ
PKS 0332-403	FSRQ	18.8	$3.6^{+0.3}_{-0.6}$	2.5 ± 0.4
PKS 0348–120	FSRQ	93.6	< 0.1	-
PKS 0405–385	FSRQ	1.9	< 0.2	-
PKS 0537-286	QSO	23.7	$4.1^{+0.1}_{-1.3}$	1.3 ± 0.2
PKS 0537-441	BLLAC	19.3	$3.6^{+0.4}_{-1.5}$	2.8 ± 0.5
PKS 2255-282	FSRQ	5.4	$8.0^{+0.3}_{-0.7}$	1.67 ± 0.14
RGB J0152+017	BLLAC	31.1	6.4 ± 0.4	$2.47^{+0.19}_{-0.18}$
RHS 53	BLLAC	9.2	$3.7^{+0.3}_{-0.5}$	1.74 ± 0.23
W Com	BLLAC	23.7	< 1.8	1.7 ± 0.7

Note–*RXTE* archival AGN which were not included in our main sample with object NED type, PCA exposure time, 2–10 keV flux and Γ where it could be constrained. Note that the errors given are purely statistical and do not reflect systematic uncertainties in the background. Thus some of these sources may seem to have Γ constrained to within 10% such that they could be included in the sample, however due to low flux or very short exposure the background systematics are large enough that they were not included. "-" indicates an unconstrained parameter. ULIRG is an ultra luminous infrared galaxy and BALQSO is a broad absorption line quasar.

3.6 Acknowledgements

Chapter 3, in part, is a reproduction of material as it appears in the Astrophysical Journal 2011, Rivers, Markowitz & Rothschild, ApJ, 2011a; and, in part, has been submitted for publication to the Astrophysical Journal 2012, Rivers, Markowitz & Rothschild.s

4 An Eclipse of Centaurus A

Cen A is one of the closest and consequently one of the brightest AGN in our sky. High resolution data from infrared and X-ray observatories (such as *Spitzer* and *Chandra*) have revealed many details about the structure of its prominent jets as well as the core of the nucleus. Cen A has proved to be an excellent laboratory for studying the properties of blazar jets, however it also displays certain X-ray properties characteristic of a Seyfert galaxy, likely due to its orientation. For example, X-ray spectroscopy shows a prominent Fe line at 6.4 keV originating in cool material far from the central nucleus (Evans et al. 2004) and strong absorption in the line of sight. Broad optical emission lines have never been detected in this source, marking it as a Seyfert 2. A search for hidden broad lines through polarized scattered light by Alexander et al. (1999) ruled out the existence of a hidden broad line region (BLR).

Between the launch of the *RXTE* in 1996 and 2009 February, Cen A was observed 13 times, each an extended exposure of $\sim$10–100 ks. Spectral analysis on these data in the 3–100 keV band revealed a longterm average photon index of $\Gamma = 1.83 \pm 0.01$, an equivalent H column density of $N_{\rm H} = 16.9 \pm 0.3 \times 10^{22}\,{\rm cm}^{-2}$, and also confirmed the lack of a Compton reflection hump in this source. Rothschild et al. (2011) analyzed the individual Cen A observations, examining both spectral and temporal characteristics of this source. From these analyses it was discovered that for three observations between 2003 March and 2004 February, the column density of cold material along the line of sight to the nucleus increased by $\sim$60%, from 16 $\times 10^{22}\,{\rm cm}^{-2}$ to 26 $\times 10^{22}\,{\rm cm}^{-2}$. From this it was inferred that a clump of material may have passed through the line of sight at a distance commensurate with the molecular torus. Such an event is consistent with clumpy torus models such as that developed by Nenkova et al. (2008a; 2008b). However there were only three data points in this interval and therefore the physical parameters of the inferred clump such as size, number density, and shape, were loosely constrained at best.

Similar short-term increases and decreases in $N_{\rm H}$ have been seen previously in a number of AGN, notably MCG–6-3015 (McKernan & Yaqoob 1998), NGC 4051 (Guainazzi et al. 1998), NGC 3227 (Lamer et al. 2003), NGC 3516 (Turner et al. 2008), and NGC 1365 (Risaliti et al. 2009). McKernan & Yaqoob (1998) posited that a small clump of material was occulting a complex source for $\sim$ 100 ks, causing changes in the measured covering fraction of the absorber. Risaliti et al. (2009) analyzed a 60 ks *XMM-Newton* observation of NGC 1365, finding very rapid changes in $N_{\rm H}$ on the order of only a few hours. From the short duration of these events they inferred that the material must be quite close to the central nucleus. Further analysis performed by Maiolino et al. (2010) with a 300 ks *Suzaku* observation confirmed these rapid variations and attributed them to comet-shaped BLR clouds transiting the line of sight on timescales of $\sim$50–100 ks. Note that most of these did not have the advantage of continuous monitoring over timescales of days to months, however Lamer et al. (2003) was able to fit a β density profile to explain the smooth increase and decrease in $N_{\rm H}$ for NGC 3227 over about 300 days as seen with *RXTE* monitoring.

A sustained monitoring campaign of Cen A with *RXTE* began on 2010 January 1, with $\sim$1 ks snapshots every 2 days. One goal of this observing campaign was to better quantify variation in the column density in this source and to search for additional evidence of transits by discrete clumps of material, with the ability to place better constraints on their physical characteristics. To that end we have analyzed the *RXTE* observations of Cen A from the monitoring campaign, beginning 2010 January 1 up through 2011 April 20.

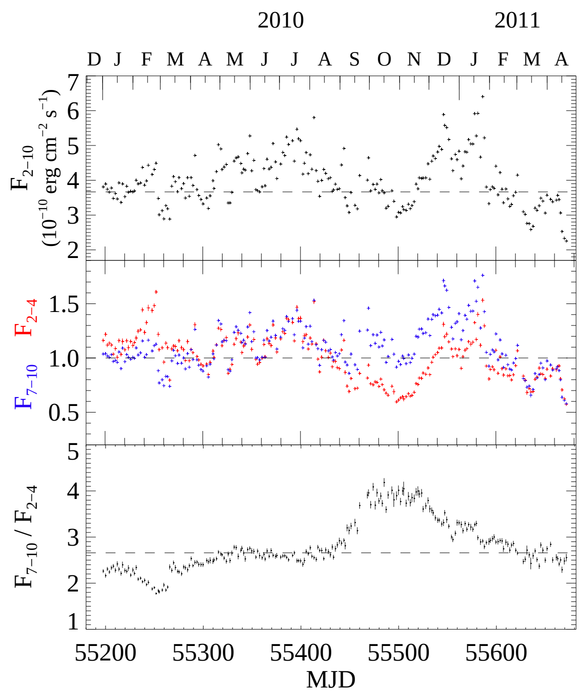

Figure 4.1: Light curves for the monitoring campaign from 2010 January 1 up through 2011 April 20. The top panel shows the 2–10 keV flux light curve. The middle panel shows 2–4 and 7–10 keV fluxes normalized to their respective means. The bottom panel shows the F_{7-10}/F_{2-4} ratio.

4.1 Time Resolved Spectral Analysis

We analyzed 228 $\sim$1 ks snapshots of Cen A taken with the *RXTE*-PCA. The 2–10 keV flux light curve is shown in Figure 4.1 along with fluxes in the 2–4 and 7–10 keV ranges. The ratio F_{7-10}/F_{2-4} can indicate variations in N_H for Compton-thin sources which are independent of variations in the shape of the power-law continuum. There was a clear temporary increase in this ratio between MJD 55440 and 55600 that can be inferred to be a temporary increase in N_H caused by a cloud or clump of material passing through the line of sight to the nucleus. To confirm this we performed time-resolved spectral fitting.

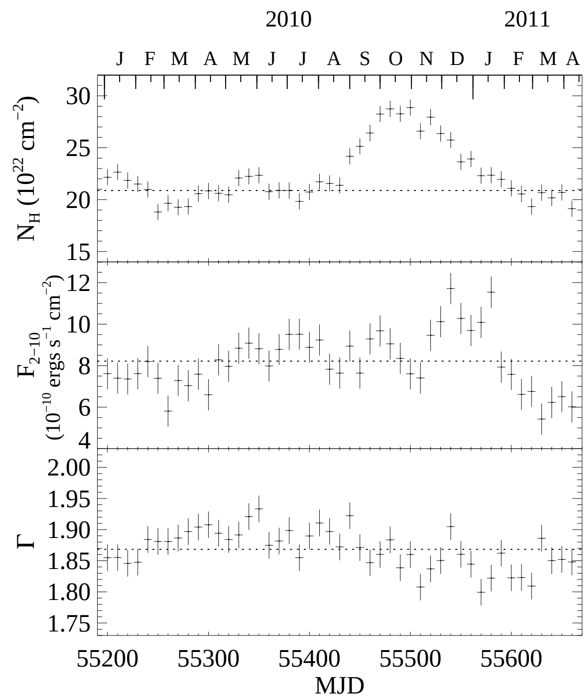

Figure 4.2: Time resolved spectral parameters from 2010 January through 2011 April. The top panel shows the column density along with a dotted line indicating the average value for the first 200 days of 20.8 $\times 10^{22}\,\mathrm{cm}^{-2}$. The middle panel shows the unabsorbed 2–10 keV flux, and the bottom panel the photon index, both with dotted lines indicating the average values for each. Note that the photon index is consistent with maintaining a constant value of 1.87 $\pm$0.03 throughout the monitoring.

We analyzed PCA spectra in 10 day intervals with total exposures of 3–6 ks, including data from 3–30 keV in all time bins. The base model consisted of a

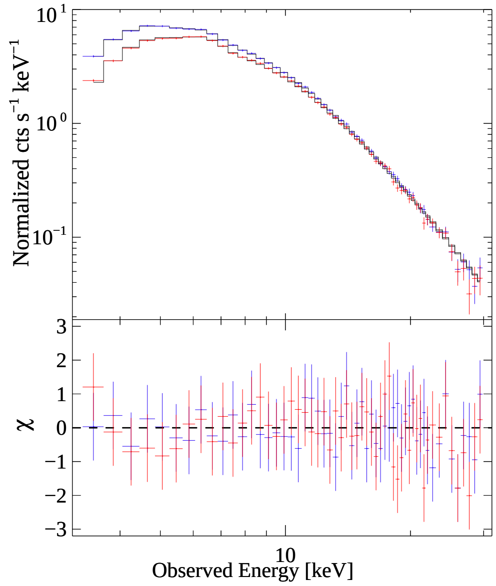

Figure 4.3: Two sample spectra with data and best-fit residuals. Blue corresponds to an N_{H} of 20.7 $\times 10^{22}\,\mathrm{cm}^{-2}$ (MJD 55355–55365). Red corresponds to an N_{H} of 28.9 $\times 10^{22}\,\mathrm{cm}^{-2}$ (MJD 55495–55505).

power law with a fixed Galactic absorption column of 8.09 $\times 10^{20}\,\mathrm{cm}^{-2}$ (Kalberla et al. 2005), an additional cold absorber with a free column density, and an Fe line modeled with a Gaussian. Results from this fitting are shown in Figure 4.2 and example spectra with models and best-fit residuals are shown in Figure 4.3. Reduced χ^2 values were close to 1 in all cases.

It is clear that N_{H} increased significantly for ~ 6 months between 2010 August and 2011 February, rising from ~ 20 $\times 10^{22}\,\mathrm{cm}^{-2}$ to a maximum of 27 $\times 10^{22}\,\mathrm{cm}^{-2}$. The average column density in the 7 months preceding this event was 20.9 $\times 10^{22}\,\mathrm{cm}^{-2}$. The photon index values were consistent with a constant $\Gamma = 1.87 \pm 0.03$ through this 16 month period. Fe line parameters (which are not shown here) were poorly constrained but showed no evidence for strong variability. We tried applying the CABS model to test whether the slight fluctuations in the unabsorbed 2–10 keV flux were due to extra scattering by the increased amount of material in the line of sight. This model is more commonly used for Compton-thick sources to model the attenuation of the power law by scattering, however since the changes in N_{H} were less than $10^{23}\,\mathrm{cm}^{-2}$, including this model did not affect the relative magnitude of the fluctuations and we did not use it in our final analysis.

The most likely scenario to explain this increase is that a clump of material passed through the line of sight to the source over the course of about 6 months. In order to explore the properties of this clump we fit a number of possible geometries to the time resolved N_{H} values using IDL version 6.3. Uncertainties on spectral fit parameters were calculated using a point-to-point variance method (Vaghan & Edelson 2001; Markowitz et al. 2003) at the 1σ level for all parameters. This method was appropriate for our analysis since the normal method tends to overestimate errors due to the background modeling for short observations such as ours.

We tested three density profiles for the increase in N_{H} above a constant baseline which was left free: a sphere of uniform density; a β profile as used by Lamer et al. (2003) to fit a similar occultation observed in NGC 3227 given by the equation,

$$N_{\mathrm{H}}(r) = N_{\mathrm{H\ center}} \times \sqrt{1-(r/R_{\mathrm{c}})^2} \tag{4.1}$$

where R_c is the core radius (Dapp & Basu 2009); and a linear-density sphere with a maximum central density and a density profile described by the equation,

$$\rho(r) = \rho_{\mathrm{center}} \times \frac{(R-r)}{R} \tag{4.2}$$

where R is the outer radius of the spherical clump. Figure 4.4 shows the data, models and fit residuals for all three models. The linear-density sphere gave the best fit with $\chi^2/\mathrm{dof} = 73/43$. The β model gave $\chi^2/\mathrm{dof} = 96/43$ and the uniform sphere gave an unacceptable fit with $\chi^2/\mathrm{dof} = 160/43$. For the linear-density sphere we found that the occultation lasted a total of 170 days with a maximum column density of 8.4 $\times 10^{22}\,\mathrm{cm}^{-2}$ above a baseline of 20.9 $\times 10^{22}\,\mathrm{cm}^{-2}$. The core radius crossing time (FWHM) for the β model was 60 days with a maximum column density of 10.3 $\times 10^{22}\,\mathrm{cm}^{-2}$ above a constant baseline level of absorption of 19.0 $\times 10^{22}\,\mathrm{cm}^{-2}$.

We also tested for cometary tails as seen by Maiolino et al. (2010), testing for asymmetry in the ingress and egress durations, however these did not improve the fit. From visual inspection it is clear that the Cen A occultation is fairly symmetrical with a smooth, gradual increase and decrease in the column density whereas a comet-like shape would be appropriate for a rapid increase and slow decrease. Consequently, this model is inappropriate for this source.

4.2 Implications for a Clumpy Torus

Of the other AGN with similar short term increases or decreases in N_{H}, many have posited that these clouds are part of the BLR rather than constituents of the torus. The low density of the clumps observed in Cen A combined with the lack of detected broad lines in this source (Alexander et al. 1999) make this a very unlikely scenario. Therefore we conclude that the transiting clump(s) that have been seen in this source must arise from the dusty torus.

The clumpy torus model of Nenkova (Nenkova et al. 2008a; Nenkova et al. 2008b) predicts a small number of clumps along the line of sight to the nucleus making up the total observed column density. This is borne out in our observation. The ratio of the baseline column density to the average increase caused by the clump is ~ 5. We can therefore assume that the number of clouds along the line of sight is $\lesssim 5$ since some of the baseline absorption column may be dust free and reside inside the inner radius of the dusty torus. For example, the very short transits seen by Risaliti et al. (2009) must come from inside the dust sublimation radius. Assuming a viewing angle to the equatorial plane of $62.^{\circ}6$ and an angular distribution of clouds of 60° (Ramos Almeida et al. 2009) we calculate that the average number of clouds along an equatorial ray is $\lesssim 14$. This is consistent with Rothschild et al. (2011) as well as the predicted number of clumps from Nenkova et al. (2008b) which is no more than 10–15 clumps along an equatorial ray.

Assuming that all of these clouds have an average column density of $4 \times 10^{22}\,\mathrm{cm}^{-2}$ this would imply a total column density along the equator of $\sim 6 \times 10^{23}\,\mathrm{cm}^{-2}$ which is just on the verge of being Compton-thick. This is reasonable given that no Compton reflection signal has ever been detected in this source.

The distance of the dusty torus in Cen A from the central illuminating

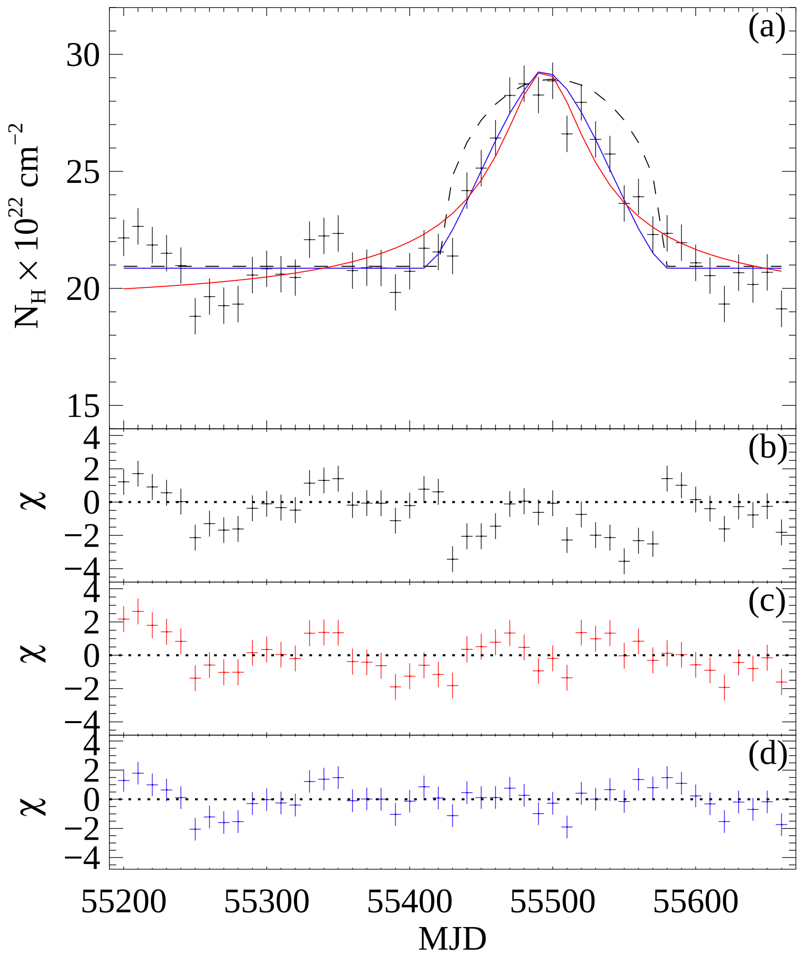

Figure 4.4: Three model fits to the N_{H} profile. Panel (a) shows the data with three models: a uniform sphere (black dashed line), a β model profile (blue line), and a linear-density sphere with maximum density at the center falling linearly with radius (red line). Panel (b) shows fit residuals to the uniform sphere model, panel (c) shows residuals to the β model, and panel (d) shows residuals to the linear-density sphere model.

source derived from infrared measurements by Meisenheimer et al. (2007) was 0.1–0.3 pc. For a bolometric luminosity of 10^{43} erg s^{-1} (Whysong & Antonucci 2004), Nenkova et al. (2008b) calculated an inner dust sublimation radius of 0.04 pc. We can place limits on the radius of the torus by following the calculations of Lamer et al. (2003) which use the information that the obscuring material is completely cold with an ionization parameter $\lesssim 1$ and assuming Keplerian motion. Their equation (3) gives a relationship between the radius of the material and the ionizing luminosity ($L_{\rm ion}$) of the source:

$$R \simeq 4 \times 10^{16}\, M_7^{1/5} \left(\frac{L_{42}\, t_{\rm days}}{N_{22}\, \xi} \right) \tag{4.3}$$

Where M_7 is the mass of the black hole which has been measured at $\mathrm{M}_{BH} = 6 \times 10^7$ $M_\odot$ (Cappellari et al. 2009; Neumayer et al. 2010), $L_{42} = L_{\rm ion}/10^{42}$ where $L_{\rm ion} \approx 3 \times 10^{42}$ erg s^{-1} is the ionizing radiation at 13.6 keV, $t_{\rm days}$ is the crossing time of the event, and N_{22} is the maximum column density of the clump. Assuming ξ=1 erg cm s^{-1} gives a minimum distance to the torus of ∼0.1 pc, consistent with the values found from infrared measurements. We adopt an inner radius of 0.1 pc and an outer radius of 0.3 pc.

Using parameters determined by the linear-density sphere model (this model gives a better fit to the data than the other models, though it is a purely empirical model) we can calculate the size of the clump and quantify the density profile. To begin we adopted the assumptions made in Rothschild et al. (2011) for Keplerian motion at 0.1–0.3 pc around the 6×10^7 M_{BH} black hole and calculated a clump velocity of ∼930–1600 km/s. Combining this with the measured 170 day transit we found a linear-density sphere with a diameter of 1.4–2.4 $\times 10^{15}$ cm with a central number density of $\mathrm{n_H}$ = 1.8–3.0 $\times 10^7$ cm^{-3}. The total mass of this clump can be approximated as 2–5 $\times 10^{28}$ g or about 3–10 times the mass of the Earth.

For comparison, the occultation (if indeed it was a single absorption event) inferred by Rothschild et al. (2011) lasted between 1 and 4 years with an increase in column density of ∼6 $\times 10^{22}$ cm^{-2}. Assuming a single uniform sphere it was found that the clump would have an inferred length of 3–12 $\times 10^{15}$ cm and a number density of 1–3 $\times 10^7$ cm^{-3}.

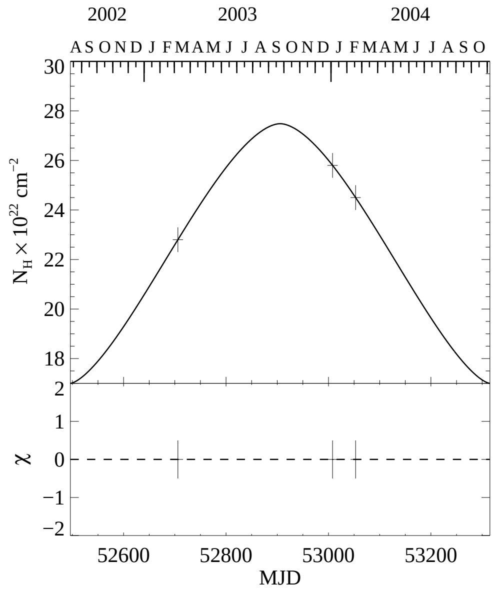

Figure 4.5: Fitting the linear-density sphere to the 2003–2004 increase in N_{H}. The solid line represents a single clump occulting the source with data–fit residuals shown in the lower panel.

Fitting this occultation event with a single linear-density sphere model we found a length of $7{\times}10^{15}$ cm and a central density of $8 \times 10^{6}\,\mathrm{cm}^{-3}$. The best fit model with residuals is shown in Figure 4.5; notice that with only three data points we needed to assume the baseline column density rather than leave it as a free parameter as we did with the more recent event. For this baseline we have chosen the longterm average value given in Rivers et al. (2011) of $16.9\times10^{22}\,\mathrm{cm}^{-2}$. This is somewhat larger and more diffuse than the more recent clump by a factor of 2–3, however this can easily be explained by inherent variation in clump sizes within the torus. Alternatively two or three much smaller, more dense clumps could adequately fit these three data points with similar characteristics to the more recent event, however with so few data points it is impossible to place constraints on such a scenario.

4.3 Acknowledgements

Chapter 4, in full, is a reproduction of material as it appears in the Astrophysical Journal 2011, Rivers, Markowitz & Rothschild, ApJ, 2011c.

5 The Geometry of MCG –2-58-22

MCG –2-58-22 is an X-ray bright Seyfert 1.5 active galactic nucleus (AGN) located at a redshift of $z = 0.04686$. Past X-ray observations of this source performed with *EXOSAT*, *ASCA*, *XMM-Newton* and *BeppoSAX* have revealed the following spectral components in addition to the primary X-ray power law: a soft excess, Fe emission lines, and a Compton reflection hump. Importantly, there has been no evidence for X-ray absorption by gas along the line of sight in excess of the Galactic column, indicating that in the X-ray band this AGN is a "bare nucleus". This combination makes MCG –2-58-22 an interesting target of study, since the lack of significant X-ray absorption provides a clean view of the nucleus with a relatively simple spectrum to model, while the presence of strong reflection components allows us to place constraints on the physical geometry of the circumnuclear material surrounding the AGN.

Ghosh & Soundararajaperumal (1992) analyzed *EXOSAT* data obtained in 1984 that revealed the highly variable soft excess below about 2 keV. They modeled this component with a steep power law in addition to their continuum power law. *ASCA* data covering 2.5–10 keV with good CCD resolution were analyzed by Weaver et al. (1995). They modeled the spectrum using a hard X-ray power law ($\Gamma = 1.75 \pm 0.05$) with Galactic absorption and confirmed the need for a soft excess, as well as an Fe Kα emission line which was unresolved. Weaver, Gelbord & Yaqoob (2001) analyzed two additional *ASCA* observations of MCG –2-58-22, tracking the Fe line flux over a time scale of years and showing large variation in the flux of the underlying continuum. However large uncertainties precluded definitive conclusions about the variation of the Fe line parameters.

A more recent analysis by Bianchi et al. (2004) using simultaneous data from *XMM-Newton* and *BeppoSAX* covered a much broader energy range than previous observations (0.5–200 keV). Unfortunately only 7 ks of good EPIC-pn data were obtained for the source, providing only loose constraints in the Fe K bandpass (the Fe Kα line was unresolved with $\sigma <$ 340 eV and an equivalent width, EW, of 45^{+85}_{-24} eV). They were able to loosely constrain the Compton reflection hump with $R = 0.4 \pm 0.3$ and $\Gamma = 1.72^{+0.08}_{-0.06}$.

In this chapter we present an in-depth analysis of a single 140 ks long-look *Suzaku* observation of MCG –2-58-22 with good energy resolution and effective area around 5–7 keV for detailed analysis of the Fe K complex (Mitsuda et al. 2007). Our goals for this observation were to study the Fe K emission, constrain the Compton hump, confirm the bare nucleus, and study the soft excess, all of which *Suzaku* is capable of doing well. This information can then be used to explore possibilities for the geometry of the circumnuclear material including the Fe line emitting gas and we improve upon parameter values in the literature for the Compton hump and Fe K emission lines.

5.1 Details of the Observation

Suzaku observed MCG –2-58-22 on 2009 November 27 beginning at 22:49 UT (Observation ID 704032010). Data were processed with version 2.4.12.27 of the *Suzaku* pipeline and typical screening criteria were applied.

After screening, the good exposure time per XIS was 138.9 ks. Data from the two front-illuminated CCDs were summed to create a single co-added FI spectrum after it was confirmed that the two spectra were consistent. Data were ignored above 12 keV (10 keV for BI) where the effective area of the XIS begins to drop dramatically. Data were ignored below 1.0 keV (0.7 for BI which has a larger effective area at low energies) due to time-dependent calibration issues of the instrumental O K edge at 0.5 keV, and between 1.5 and 2.4 keV due to large calibration uncertainties for the Si K complex and Au M edge arising from the

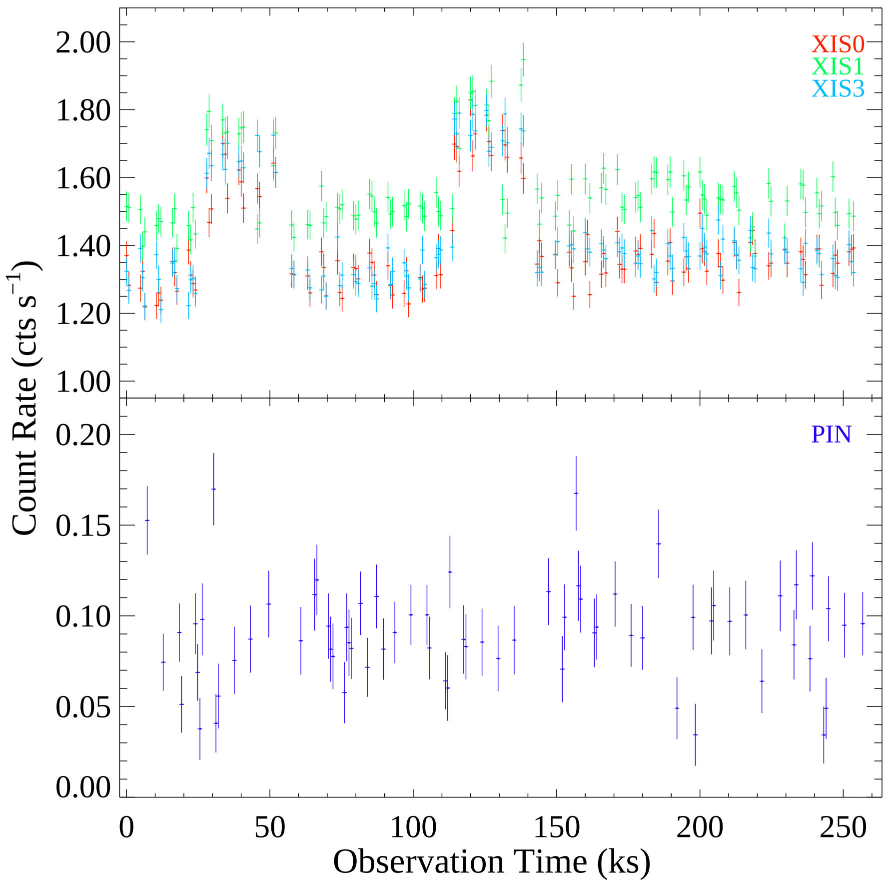

Figure 5.1: The lightcurve over the duration of the observation. Bins are 800 s. The XIS count rates are in the 2–10 keV range while the PIN count rates are in the 20–50 keV range. The increases in flux seen in the XIS around 30–50 ks and 110–140 ks are small (only about 20%) and flux-resolved spectroscopy did not reveal significant change in the shape of the spectrum during these episodes.

detector mirror system. These issues are not fully understood at the time of this writing. Average 2–10 keV rates were 1.410±0.002 and 1.521±0.003 counts s^{-1} per XIS for FI and BI respectively. Figure 5.1 shows the XIS lightcurves for the duration of the observation.

Fitting the ^{55}Fe calibration source spectra in XSPEC with a model comprised of three Gaussian components (Mn Kα_1, Kα_2 and Kβ) yielded the following results for the Mn Kα_1 line energy (expected value of 5.899 keV): 5.886 keV (FI) and 5.890 (BI), showing that the energy calibration has a systematic uncertainty of $\sim$10 eV for both the FI the BI. Additionally, these lines had an average width of 30 eV, which we will take as instrumental broadening in excess of that modeled by the response matrix, and have subtracted this value in quadrature from all measured line widths.

Net PIN spectra were extracted and deadtime-corrected for a net exposure time of 98.0 ks. We excluded PIN data below 13 keV due to thermal noise and above 60 keV where the effective area of the detector falls significantly. The average 13–60 keV rate was 0.202±0.002 counts s^{-1}. Figure 5.1 shows the PIN lightcurve for the duration of the observation.

5.2 Spectral Fitting

All fits included absorption by the Galactic column with $N_{\rm H,\,Gal}=2.70\times10^{20}$ cm^{-2} (Kalberla et al. 2005).

5.2.1 The Fe K Bandpass

We began our analysis with a preliminary study focused on the Fe K bandpass. We used data from 4.5–8.5 keV from the FI spectrum only because of its excellent response and effective area in this energy range. We analyzed the Fe K complex, including the Fe Kα and Kβ lines and the Fe K edge, and investigated the possibility of emission from ionized Fe, namely Fe XXV or XXVI (the latter was reported by Bianchi et al. 2004 with a 2σ detection).

As a first step we fit a simple power law with Galactic absorption. Model–

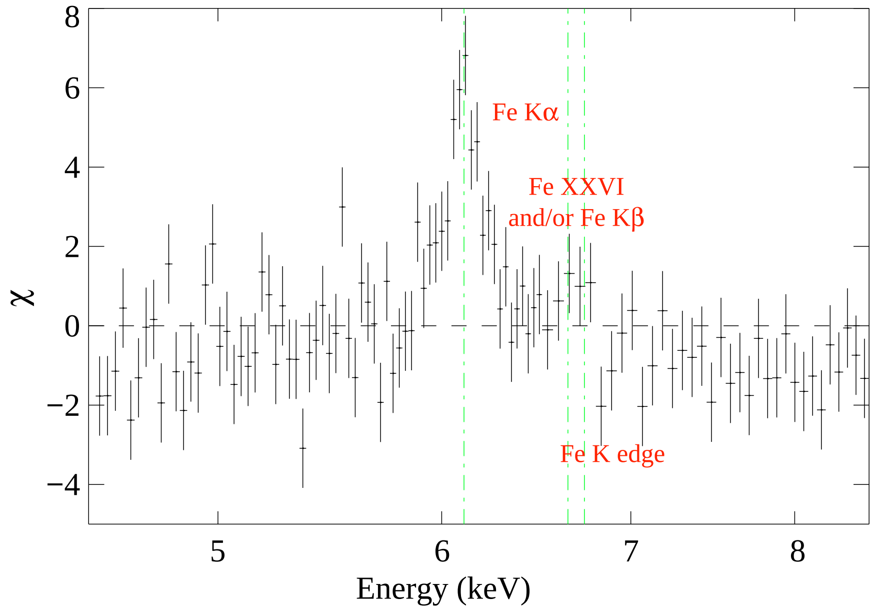

Figure 5.2: Data–model residuals for a simple power law fit over the Fe K band from 4.5–8.5 keV using the FI XIS data only. Dashed lines show expected locations (*from left to right*) of the energy centroids of the Fe Kα, XXVI, and Kβ lines. Note that these are the observed energies ($z = 0.04686$).

data residuals for the simple power law are shown in Figure 5.2. This yielded a poor fit with χ^2/dof = 322/100 and obvious residuals around 6.4 keV (rest frame energy), the location of the Fe Kα line. Fitting the line with a Gaussian component provided a much better fit with χ^2/dof = 117/97. Visual inspection then revealed additional residuals around 7.1 keV (the location of the Kβ line and Fe K edge).

We then added an edge component to model additional Fe K shell absorption in excess of the Galactic column and/or the Fe K edge associated with Compton reflection. We fixed the edge energy at 7.11 keV and left the optical depth (τ) free. χ^2/dof dropped to 108/96, indicating a significant detection of the edge at a confidence level of $\sim$99.4% according to an F-test [1].

Assuming an origin in neutral or lowly-ionized gas, an Fe Kβ line should be present in addition to the Fe Kα line. We added a Gaussian emission line with its energy centroid frozen at 7.056 keV (degeneracy with the Fe K edge at

[1]Note that an F-test is inappropriate to perform in this case (see Protassov et al. 2002), however it can give a rough approximation of the significance.

7.11 keV and lack of sufficient line strength to provide good constraints led to our freezing the parameter at its expected value), its width tied to that of the Kα line and its normalization left free. The fit improved, with χ^2/dof dropping to 103/95 with a normalization of 15$\pm$12% of the Kα normalization, consistent with that expected for cold/neutral gas. An F-test[3] indicates that this is a 2σ detection at the $\sim$96.4% confidence level.

In some AGN, contributions to the total observed Fe K emission profile can arise from material which is ionized, either by collisional- or photo-ionization. Using *XMM-Newton*-EPIC data, Bianchi et al. (2004) found a degeneracy between the parameters of the Kβ line and those from a possible Fe XXVI emission line. They reported a 2σ detection of the Fe XXVI line when the Kβ line was not included and with all the parameters of the line left free. When we allowed the energy of the Kβ line to be free to vary we found an energy centroid of 7.0$\pm$0.1, consistent with both the Kβ and Fe XXVI line energies. χ^2/dof was 102/95 (not a significant improvement) and the normalization was 18$\pm$14% of the Kα normalization. Freezing the line energy at 6.966 keV, the weighted average of the Fe XXVI doublet, provided a fit virtually identical to the one presented above. Fitting both lines simultaneously with energies frozen at their expected values and widths tied to that of the Kα line gave χ^2/dof =102/94 with a normalization of 13^{+18}_{-11} % for Fe XXVI and an upper limit of 26% for Kβ (both percentages are with respect to the Kα normalization). We therefore cannot rule out the that the source may contain both emission lines and that we are simply unable to deblend them. For simplicity, in all further models described in this paper we have included only the Kβ line with frozen or tied parameters.

We also tested for the presence of Fe XXV (using a Gaussian component with energy centroid fixed at 6.70 keV), however χ^2/dof did not improve and only an upper limit to the normalization was obtained ($\lesssim 6\times10^{-6}$ ph cm^{-2}s^{-1}). Final parameters for the Fe K complex model fit including the Kα line, Fe K edge and Kβ line are listed in Table 1 as the "Fe K Band" model, including the Fe Kα energy centroid (E), intensity (I), width (σ), and EW.

We also tested the "DISKLINE" model for the emission lines in place of the more phenomenological Gaussian model. DISKLINE models the Doppler broadening of an emission line associated with the inner region of an accretion disk (Fabian et al. 1989). The diskline parameters were not well constrained, giving a very large inner radius ($R_{in} \gtrsim 20\ R_S$, where R_S is the Schwarzchild radius) and a narrow profile. It did not improve the fit over a simple Gaussian. Next we tried the addition of a broad DISKLINE (R_{in} constrained to around 3 R_S and energy fixed at 6.4 keV) to a narrow Gaussian line with energy and width fixed at the values found with the Gaussian fit (see Table 1). We obtained an upper limit to the DISKLINE normalization of $\lesssim 2\times10^{-5}$ ph cm^{-2}s^{-1} and an EW of $\lesssim$35 eV. It is thus possible that a weak broad line exists in this source and that we are simply unable to detect it; however combining the weakness of this feature with the lack of ionized emission indicates that most if not all of the Fe line flux comes from material that is not close in to the central black hole.

It is possible that such a weak broad line would be degenerate with the Compton shoulder, a feature which could arise if there is a significant amount of Compton-thick material. Additionally, by visual inspection we see a shallow shelf-like shape in the residuals on the low-energy side of the emission line when σ is set to $\lesssim$30 eV. We tested this by modeling a moderately broad Gaussian in addition to the narrow Fe Kα line in the "Fe K Band 2" model with an energy centroid fixed at 6.34 keV (Matt 2002). This resulted in an improvement in χ^2/dof of only 2/1, which is not a significant detection but indicates that the Compton shoulder should be tested for in future observations.

5.2.2 Broadband Fitting

Next we fit the broadband spectrum of MCG –2-58-22 covering the range from 0.7–60 keV. We used the XIS FI, XIS BI, and PIN spectra. We included an instrumental cross-normalization constant in our fits with the PIN constant set to 1.16 (this is the expected value for XIS-nominal pointing and leaving the parameter free caused degeneracy with the Compton reflection component in our models) and the BI constant left free relative to the FI spectrum (values were typically around ~1.05). The broadband data are shown in Figure 5.3a. Figure

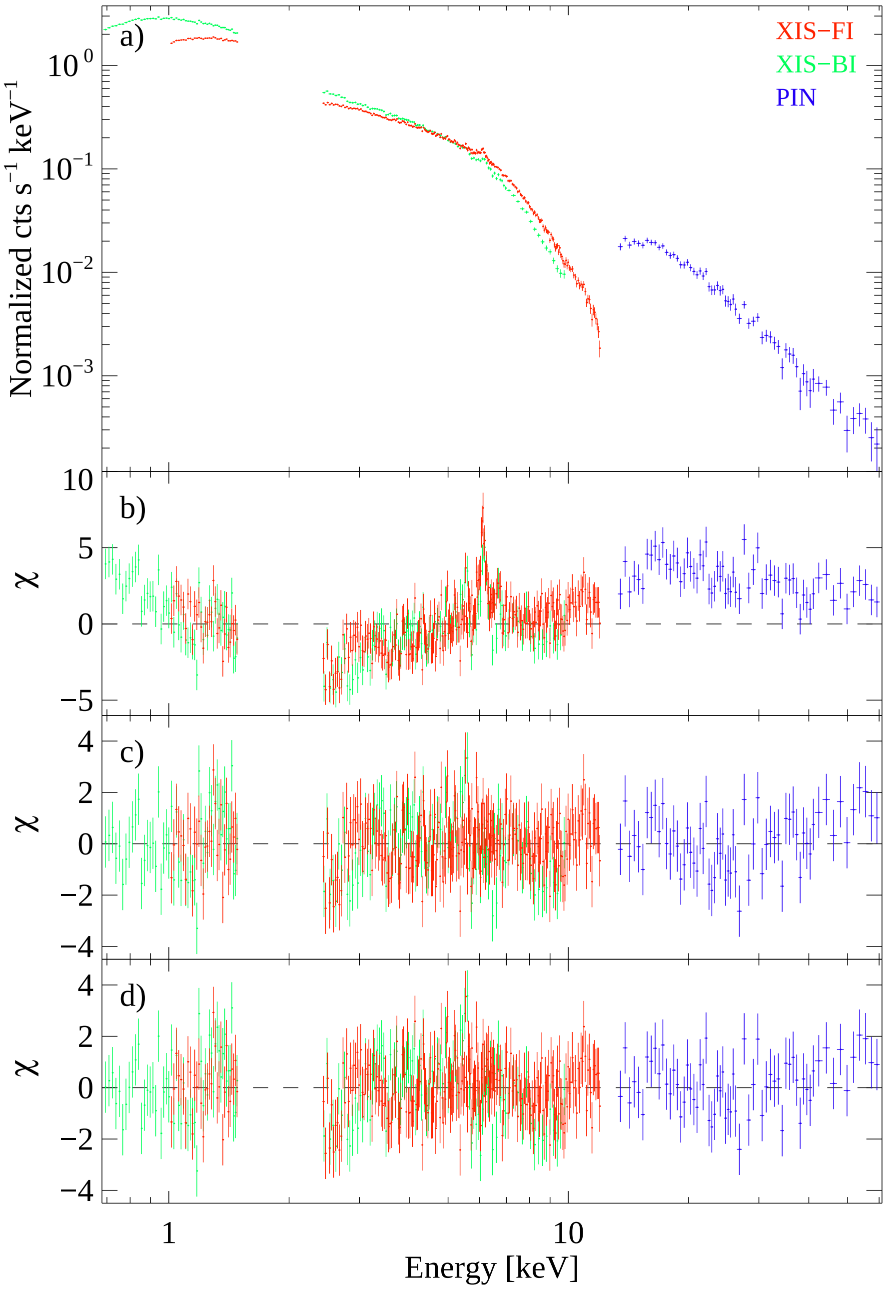

Figure 5.3: Spectral fitting for MCG −2-58-22 from 0.7–50 keV. Panel a) shows the data from the XIS FI and BI, and the PIN. Panel b) shows the data–model residuals for a simple absorbed power law. Panel c) shows the data–model residuals for our best-fit disk/slab geometry model including the iron lines, soft excess and Compton hump in addition to the continuum. Panel d) shows the data–model residuals for our best fit torus geometry model utilizing MYTorus. It is obvious that the fits shown in panels c) and d) are virtually identical though the modelling is quite different.

5.3b shows residuals to a simple power law fit in which we can clearly see the need for modeling the Fe K complex, Compton reflection peaking around 20–30 keV, and a soft excess below ~ 1 keV.

We began by modeling the soft excess with a simple power law in addition to the continuum power law and modeling the Compton reflection hump using PEXRAV (Magdziarz & Zdziarski, 1995). Best fit parameters for this model are listed under "Broadband 1" in Table 1 and data–model residuals are shown in Figure 5.3c. We did not find the need for additional cold absorption with an upper limit to the column density of 2.5×10^{20} cm^{-2} in excess of the Galactic. We also tested for the presence of warm absorption using an XSTAR table but found it unnecessary for a good fit. The Compton reflection hump and Fe K edge were well fit by the PEXRAV model and Fe line parameters were very similar to those found from narrow band fitting, including the upper limit to a relativistically broadened DISKLINE component. The observed 2–10 keV flux was $F_{2-10}=5.0 \pm 0.1 \times 10^{-11}$ ergs cm^{-2} s^{-1} and the intrinsic luminosity, calculated using the cosmology-corrected luminosity distance given by NED, and correcting for Galactic absorption was $L_{2-10}=2.30\pm0.05 \times 10^{44}$ ergs s^{-1}. Figure 5.4 shows historical values of the flux of this source in the 2–10 keV range.

We also tried a (phenomenological) blackbody emission component to model the soft excess. Parameters are listed in Table 1 under "Broadband 2". Both the blackbody and power law models fit the data reasonably well, but in both cases parameters were difficult to constrain due to calibration issues with the O K edge below about 1 keV. For simplicity we adopt Broadband 1 as our best-fit model for the discussion in Section 4.

Bianchi et al. (2004) tested for high energy cut offs in their sample finding model-dependent values of $E_c \sim 200$ keV with error bars of 50–800 keV. Extending up to only 60 keV, our data are not highly sensitive to a high energy cut off or rollover. Utilizing the "CUTOFFPL" model in XSPEC we found a lower limit to the rollover energy of 500 keV.

Table 5.1: Model Parameters

Model	Γ	A^1 (10^{-2})	E (keV)	I^2 (10^{-5})	σ (eV)	EW (eV)	τ	R	$\Gamma_{\rm soft}$	$A_{\rm soft}{}^1$ (10^{-3})	χ^2/dof
Fe K Band	1.68±0.05	1.15 ±0.08	6.40±0.02	2.8 ±0.6	60 ±30	50±10	0.05±0.02				103/95
Broadband 1	1.80±0.02	1.30±0.02	6.40±0.02	2.4 ±0.3	$<$ 65	40±10		0.69±0.05	3.0±0.6	$0.14^{+0.16}_{-0.07}$	604/464
									$k_{\rm B}T$ (keV)	$A_{\rm bbody}{}^3$	
Broadband 2	1.83±0.01	1.37±0.01	6.40±0.02	2.4 ±0.3	$<$ 60	41±5		0.76±0.07	0.18 ±0.02	2.2 ±0.5	611/464

Note – Best fit parameters for models in the Fe K bandpass and broad band spectrum. "Fe K Band 1" is a model fit over the energy range 4.5–8 keV using only XIS1 (as described in Section 3.1) including the primary power law, Fe Kα and Kβ lines as Gaussians and the Fe K edge ("ZEDGE" in XSPEC). The Broadband models were fit over the energy range 0.7–50 keV using FI and BI XIS data as well as the PIN. Broadband 1 includes the continuum, Gaussian Fe emission lines, the Compton hump modeled with PEXRAV, and the soft excess modeled with a power law as described in Section 3.2. Broadband 2 differs from Broadband 1 in the use of a blackbody ("BBODY") to model the soft excess. We adopt the parameters of the best fit to the Broadband 1 model for the discussion in Section 4.

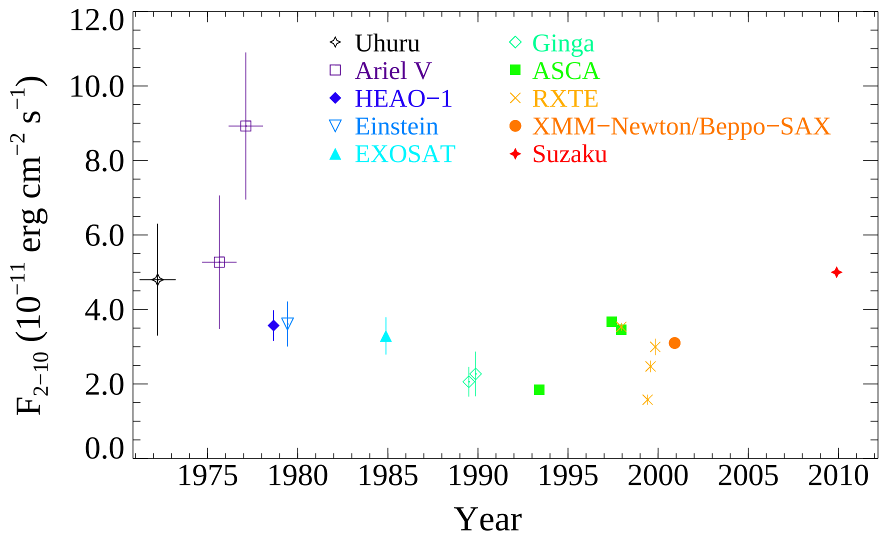

Figure 5.4: Historical values for the 2–10 keV flux. From left to right this source has been observed by *Uhuru* (Cooke et al. 1978), *Ariel-V* (Marshall, Warwick & Pounds 1981), *HEAO-1* (Griffiths et al. 1979), *Einstein* (Turner et al. 1991), *EXOSAT* (Ghosh & Soundararajaperumal 1992), *Ginga* (Nandra & Pounds 1994), *ASCA* (Weaver et al. 1995), *RXTE*, simultaneously by *XMM-Newton*/*BeppoSAX* (Bianchi et al. 2004), and most recently by *Suzaku* (this paper).

5.2.3 Applying a Self-Consistent Model

As our knowledge of AGN improves, so too should the sophistication of our modeling. Self-consistent models should be able to simultaneously model absorption and reflection by circumnuclear material, combining the Fe line, Compton reflection hump and column density along the line of sight. We have applied the model "MYTorus" (Murphy & Yaqoob 2009) to our spectrum of MCG –2-58-22 which assumes the circumnuclear material is a donut shape of uniform density and includes all three of the components listed above.

The MYTorus model was derived from Monte Carlo simulations of a dusty torus of uniform density surrounding an illuminating supermassive black hole. Relevant parameters to the model include the following: $N_{\rm H,\ Tor}$, the column density of the material in the torus (not necessarily in the line of sight); θ_{incl}, the inclination angle of the torus, with 0° corresponding to a face-on view, 90° corresponding to edge-on, and with the torus intersecting the line of sight for angles larger than 60° (the assumed half-opening angle); the photon index (Γ) and the normalization

Table 5.2: Model Parameters for MYTorus

Γ	A_{PL}[1] (10^{-2})	$N_{H,\,Tor}$ $(10^{24}\,cm^{-2})$	A_L	σ (eV)	Γ_{soft}	A_{soft}[1] (10^{-3})	χ^2/dof
1.70±0.01	1.13±0.03	$3.6^{+1.3}_{-0.8}$	0.75 ±0.14	<70	2.5±0.3	$0.4^{+0.4}_{-0.2}$	623/465

Note – Best fit parameters for the self-consistent MYTorus model with θ_{incl} fixed at 30° as discussed in Section 3.3.

(A_{PL}) of the illuminating power law; the width (σ) of the Fe Kα line (the material is assumed to be cold and the energy is not a free parameter); and with additional parameters A_S and A_L, the normalization factors of the Compton hump and Fe line respectively, to be used when the amount observed for either is significantly different from that expected by the model due to differences in covering factors, abundances, etc., from those assumed. We also included an additional power law for the soft excess.

We found a reasonably good fit (χ^2/dof = 623/465, very similar to the broadband fit χ^2 values given in Table 1) with θ_{incl} fixed at 30° (there was no significant improvement in fit with this parameter free). Since there is no extra absorption in MCG –2-58-22, the value obtained for $N_{H,\,Tor}$ is driven primarily by the strength of the Compton reflection hump and Fe line. When A_L was free to vary there was an improvement in χ^2 of 9 for 1 less degree of freedom. We obtained a value for A_L 0f 0.75±0.14, that is the amount of material creating the Fe line was about 75% of that creating the Compton hump, possibly due to an underabundance of Fe or geometrical effects not taken into account by the model (it should also be noted that the upper uncertainty on A_L is consistent with the lower uncertainty on $N_{H,\,Tor}$). Testing for an additional relativistically broadened Fe line yielded an upper limit to the normalization of $\lesssim 1.5\times10^{-5}$ ph cm^{-2}s^{-1} and an EW of $\lesssim$30 eV. Our best fit parameters are listed in Table 5.2 and data–model residuals are shown in Figure 5.3d.

5.3 Results

5.3.1 The Fe K Complex

Focusing on the Fe K band we found the need for both Fe Kα and Kβ emission lines as well as an Fe K shell absorption edge (in broadband fits this edge was modeled sufficiently by the edge associated with the Compton reflection hump in both PEXRAV and MYTORUS). From the value of the emission line width found in our best-fit broadband model we calculated the velocity full width at half maximum ($v_{\rm FWHM}$) of the emitting material to be $< 7100\ {\rm km\,s^{-1}}$. This is consistent with values obtained for the optical Hβ broad emission line of around 6400–8500 ${\rm km\,s^{-1}}$ (Osterbrock 1977; Kollatschny & Dietrich 2006; Winter et al. 2010) and is a significant improvement on previous upper limits set by Weaver et al. (1995) and Bianchi et al. (2004) of $\lesssim 30{,}000\ {\rm km\,s^{-1}}$. Using a black hole mass estimated from optical luminosity and line widths to have a value of $10^{8.4}\ M_{\odot}$ (Bian & Zhao 2003; Winter et al. 2010) and assuming Keplerian motion of the emitting material, we estimated the radius of the emitting region to be $\gtrsim 45$ lt-days or roughly 1200 $R_{\rm S}$.

We also tested for a broad line and Compton shoulder. According to de la Calle Pérez et al. (2010), roughly $\gtrsim 1.5\times10^{5}$ counts in the 2–10 keV band at CCD resolution provide good enough statistical quality to significantly detect a broad line. In the combined FI XIS we have $\sim 4\times10^{5}$ counts, and our upper limit on the EW of a broad line places us in the lower part of the EW range of detected broad lines in the FERO sample of Seyferts observed with *XMM-Newton*, wherein significant detections of broad lines with EW's in the range of 50–250 eV were reported. We conclude that a very strong broad line ($\gtrsim 50$ eV) does not exist in MCG–2-58-22 or else our observation would have been sufficient to significantly detect it; if there does exist a broad line in this source, then it must be very weak.

We would expect to see a Compton shoulder given the presence of Compton-thick material, however we did not obtain a significant detection. It should also be noted that the Compton shoulder is included in the MYTORUS model automatically, based on the strength of the Fe line and the column density of the torus.

5.3.2 Reflection and Geometry of the Circumnuclear Material

This source also shows a very prominent Compton hump around 20–30 keV (see Figure 5.3b). This feature, arising from Compton scattering of high energy photons off Compton thick material in the vicinity of the black hole, is often associated with the Fe line emission seen in AGN, since the same Compton thick material that produces the Compton hump also produces Fe K emission. By knowing the (model-dependent) relationship between the strength of the Compton hump (R) and the expected Fe line EW, we can test if Compton thick gas is capable of accounting for the entire observed Fe line flux.

Based on calculations done by George and Fabian (1991) for a disk geometry, we found that the expected Fe line EW for our value of R (assuming an inclination of 30^{o} and solar abundances) is $\sim 80\pm6$ eV. In our broadband fits we see a considerably milder Fe line flux with an EW closer to 40 eV, about half of the expected value. We found a similar, though less robust result using MYTorus, with $A_{\rm L}$ = 0.75$\pm$14 and EW = 47$\pm$6 eV (calculated from the flux of the line) which assumes a "donut-like" geometry, in this case a Compton-thick torus out of the line of sight to the nucleus. In both cases we have found a lower than expected Fe line EW, possibly due to an underabundance of Fe. This makes it unlikely that there is significant contribution to the Fe line flux from Compton thin material in the vicinity of the black hole. This is in contrast to many Seyferts; for example the sample of Rivers et al. (2011), which utilized the pexrav disk reflection model, found that on average only $\sim$30% of the Fe line flux in Seyferts is associated with the Compton reflection component, implying the presence of substantial amounts of Compton-thin material and/or supersolar abundances of Fe. However other samples of Seyferts observed with *BeppoSAX* and *XMM-Newton* (Perola et al. 2002; Bianchi et al. 2004) were shown to have values of EW and R consistent with the Fe line and reflection hump arising in the same material assuming a slab (disk) geometry and a torus geometry respectively. In all cases uncertainties have been quite large and further investigation is warranted.

5.3.3 Optical Obscuration and X-ray Absorption

We have confirmed that MCG –2-58-22 is unabsorbed in the X-ray band, a fact which is interesting considering its optical classification as a Seyfert 1.5 (Winkler 1992; Winter et al. 2010). Standard unification schemes would suggest that it should have less obscuration in the X-ray band than a typical Seyfert 2 but *more* than a typical Seyfert 1. However this is not the case, as we have obtained a very low upper limit on column density in excess of the Galactic. The question then, is whether there is material in the line of sight to the optical emission from this AGN that is *not* in the line of sight to the X-ray emitting region.

Optical reddening from dust can be characterized by the visual extinction ($A_{\rm v}$), which we calculated from the flux ratio of Hα to Hβ, using the observed values of Winkler (1992) and assuming the intrinsic value of the Balmer decrement to be 2.87 (Osterbrock 1989). We found $A_{\rm v} \sim 1.97$ mag. From this value we calculated the inferred column density of gas using the relation of Predehl & Schmitt (1995), $N_{\rm H} = (1.79 \times 10^{21}\ {\rm cm}^{-2})\, A_{\rm v}$, and assuming the Galactic gas/dust ratio holds. We inferred a column density of $\sim 3.55{\times}10^{21}$ cm^{-2}, an order of magnitude higher than our upper limit on the observed X-ray absorption column (in excess of the Galactic) of $2.5{\times}10^{20}$ cm^{-2}. Therefore, assuming the X-ray absorbing gas and optical absorbing dust track each other, the dust obscuring the optical broad line region is most likely *not* in the line of sight to the X-ray emitting regions. The inferred column density is also far too low to be associated with the dusty torus out of the line of sight which must be Compton-thick in order to produce the strong reflection component that we see (MYTorus gives a column density of $3.6^{+1.6}_{-0.9}\ {\times}10^{24}$ cm^{-2}).

Since the X-ray emitting region is theorized to be very close in to the central black hole, it seems unlikely that this dust is in the form of an extended cloud in the host galaxy lying far (kiloparsecs) from the black hole that just happens to have a hole in the right place to produce a bare nucleus in the X-rays. The dust must be distinct, however, from the Compton-thick torus, given the low inferred column density and evidence that we are viewing the AGN more or less face on. One possible explanation for this set of constraints is that there is clumpy material in the line of sight and it happens that none of the clumps are obscuring the X-ray emitting region (see, e.g., Nenkova et al. 2008a), only the optical broad line region. If future X-ray monitoring discovers a sudden, short-term increase in $N_{\rm H}$, this scenario may be supported. Another explanation is that the material is commensurate with the broad line region, thus obscuring only this region.

5.4 Acknowledgements

Chapter 5, in full, is a reproduction of material as it appears in the Astrophysical Journal 2011, Rivers, Markowitz & Rothschild, ApJ, 2011b.

6 The Disappearing Soft Excess in Mkn 590

The Seyfert 1.2 galaxy Mkn 590 (also known as NGC 863) is an excellent candidate to explore the nature of circumnuclear material in AGN. It is a relatively X-ray bright, reverberation-mapped object with a well determined black hole mass ($M_{\rm BH} = 4.90^{+0.97}_{-0.99} \times 10^7\, M_\odot$; Vestergaard & Peterson 2006). It was observed in 2004 by *XMM-Newton* and *Chandra* (Longinotti et al. 2007), showing narrow Fe K emission lines from neutral Fe, and possibly from He-like Fe and H-like Fe. Those authors modeled a Compton reflection hump, which, along with the strong neutral Fe line and lack of relativistic line broadening, suggested emission from a distant cold torus. However, lacking coverage above 10 keV, they could provide only weak constraints on the CRH strength. The *RXTE* spectrum contained only ~30 ks of good exposure time, also yielding extremely poor constraints on R (Table 3.6). *BeppoSAX* did not observe this source.

Longinotti et al. (2007) ruled out reflection from an ionized disk as the source of the soft excess, because it did not fit the ionized emission lines well. They concluded that the marginally detected Fe XXV and XXVI emission lines could originate in photo-ionized, optically-thin gas in an extended medium. Such emission lines are commonly seen in the X-ray spectra of Seyferts 2's, but not Seyfert 1-1.5's, however they are usually limited to emission lines at soft X-rays, not ionized Fe K lines. Importantly, Longinotti et al. (2007) found no evidence for an ionized absorber lying along the line of sight, which can adversely affect modeling of continuum emission components (e.g., Reeves et al. 2004, Turner et al. 2005). The only soft X-ray emission line was from O VIII, which they also

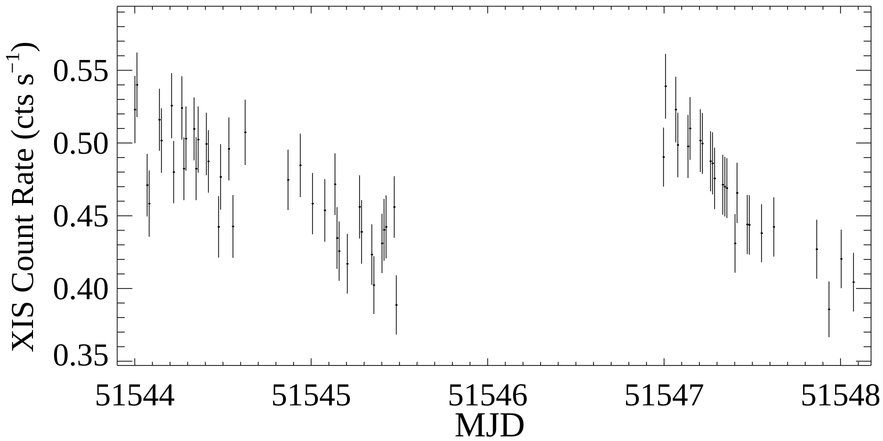

Figure 6.1: Background subtracted 2–10 XIS light curve for the 2011 January 23–26 *Suzaku* observation averaged between all three working XIS CCD's.

attributed to photo-ionized circumnuclear gas. In other words, Mkn 590 has a relatively clean line of sight to the nucleus and can be considered a "bare nucleus" like the Seyfert 1's Ark 120 (Vaughan et al. 2004) or MCG–2-58-22 (Weaver et al. 1995).

Mehdipour et al. (2011) observed a similar source, Mkn 509, several times over a period of ∼100 days with *XMM-Newton* and discovered that variations in the soft excess were not correlated with variations in the 2–10 X-ray power law, but were correlated with variations in the UV flux. This suggests that the soft excess does not arise from reflection processes off ionized material (see, e.g., Ross & Fabian 2005). Instead, one possibility is that the soft excess is created through thermal Comptonization of optical/UV photons from the disk at a location separate from the hard X-ray continuum with a lower temperature and/or optical depth causing a softer spectrum.

In this chapter we will analyze and discuss results from an observation by the *Suzaku* observatory performed in 2011 January. Our goals with this observation were to take advantage of *Suzaku*'s broadband coverage to better constrain the form of the hard X-ray spectrum, including the hard X-ray behavior above 10 keV, and to search for long-term spectral variability between the 2004 and 2011 observations.

6.1 Spectral Analysis

Suzaku observed Mkn 590 on 2011 January 23 but was interrupted by a TOO trigger. The observation was continued on 2011 January 26. Data for the two observation windows were added after we confirmed that there was no significant change in flux or spectral shape between the two observations. The total good exposure time per XIS was 102 ks. We co-added data from the two front-illuminated CCDs once we had confirmed that the spectra were consistent with each other and data were grouped with a minimum of at least 50 counts per bin. We used data in the range from 0.7–12 keV, including additional Gaussians in the fitting procedures between 1.5 and 2.4 keV to account for the calibration issues in this range (see below). Average 2–10 keV rates were 0.442 ± 0.002 and 0.538 ± 0.002 counts s^{-1} per XIS for FI and BI respectively. Figure 6.1 shows the average XIS light curve for the duration of the observation.

We extracted net PIN spectra which were then deadtime corrected for a net exposure time of 86 ks. Data were grouped manually but with a minimum of at least 200 counts per bin. We excluded PIN data below 15 keV due to thermal noise and above 45 keV where the source became too faint to detect above the background.

We began by fitting the broad spectrum (XIS+PIN) from 0.7 keV to 45 keV with a power law absorbed by a Galactic column of $N_{\rm H,\,Gal} = 2.65 \times 10^{20}\,{\rm cm}^{-2}$ (Kalberla et al. 2005). We included a fixed constant factor of 1.16 between the XIS-FI and PIN data as well as a free constant between the FI and BI data (expected to be very close to 1). We left the photon index free between the FI and BI due to instrumental flattening in the BI, however in all cases the values were consistent with each other. We also included three narrow Gaussians to account for residuals associated with the instrumental Si K complex and Au M edge. For the XIS-FI data a Gaussian with a negative normalization at 1.85 keV and a positive Gaussian at 2.26 keV accounted for these residuals. For the XIS-BI data three positive Gaussians at 1.49, 1.79 and 2.26 keV accounted for the residuals (see, e.g., Suchy et al. 2011). These energies were fixed for our fitting. The *Suzaku* spectrum is shown in Figure 6.2.

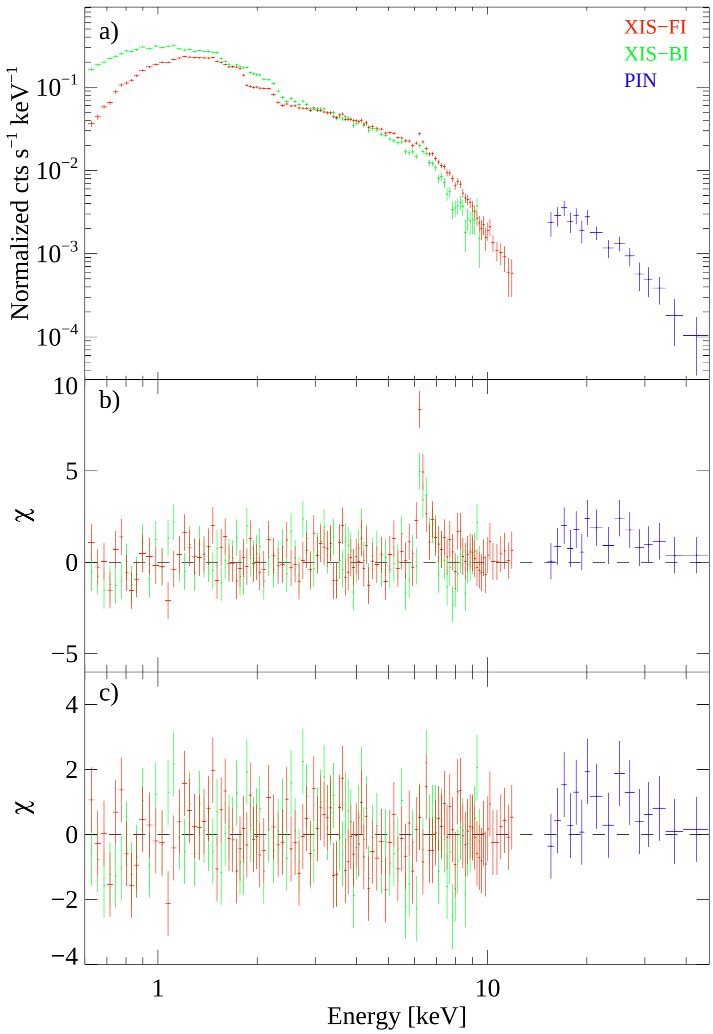

Figure 6.2: *Suzaku* XIS and PIN data for the January 2011 observation. Panel a) shows the data; b) residuals to a simple power law plus Galactic absorption; c) residuals to the best fit model with Fe Kα and Compton reflection modeled (but no soft excess component).

Residuals at 6.4 keV clearly showed the need for a neutral Fe line and broad residuals in the PIN data indicated the presence of Compton reflection (Figure 6.2b). We added a Gaussian to model the Fe Kα line and a PEXRAV component to model reflection with the photon index and normalization tied to that of the incident power law with the reflection strength, R, as the only free parameter (cos$i$ fixed at 0.45 and all abundances set to solar). Note that the systematic uncertainty in the PIN background did not contribute significantly to the total uncertainty on R ($\Delta R_{\rm Sys} < 0.01$). The addition of these components yielded a good fit with χ^2/dof =198/218. Parameters for this model are listed in Table 6.1 as our "basic" model. We measured a 2–10 keV flux of 6.8×10^{-12} erg cm^{-2} s^{-1}, corresponding to a luminosity of $L_{2-10} = 8 \times 10^{42}$ erg s^{-1} assuming a luminosity distance of 105 Mpc.

We found no evidence for the presence of absorption in excess of the Galactic column nor a soft excess below 2 keV. The latter is a surprising result since Longinotti et al. (2007) found clear evidence of a soft excess in their 2007 *XMM-Newton* data. They found $\Delta\chi^2$/dof=$-49/2$ for a blackbody with kT=156^{+14}_{-12} eV and $\Delta\chi^2$/dof=$-53/3$ for a soft X-ray power law with Γ=1.89$\pm$0.03. Adding a soft excess component to our model did not improve the fit and yielded an upper limit to the normalization of a soft power law of 3^{-5} ph keV^{-1} cm^{-2} s^{-1} at 1 keV ($\Gamma \sim 2.5$) or using the blackbody model BBODY, an upper limit to the normalization of 3×10^{-7} (with kT fixed at 156 keV) corresponding to a blackbody luminosity of $L \leq 3 \times 10^{40}$ erg s^{-1} (see XSPEC user's guide for details on the BBODY normalization).

6.1.1 Simultaneous Fitting of *Suzaku* and *XMM-Newton* Data

Searching for the source of this discrepancy we re-reduced the 2007 *XMM-Newton* data and analyzed the EPIC-pn spectrum between 0.6 and 10 keV. The EPIC-pn camera (Strüder et al. 2001) was operated in small window mode with medium filter in place in order to prevent possible photon pile-up. The data were reduced with version 11.0.0 of the XMM-Newton Science Analysis Software

Table 6.1: Parameters for Best-fit Models

Model	Basic	Basic (Γ Untied)		Basic + Soft Excess	
Data	XIS+PIN	XIS+PIN	EPIC-pn	XIS+PIN	EPIC-pn
Γ	1.67±0.01	1.71±0.01	1.82±0.01	1.67±0.01	-
$A_{\rm PL}(10^{-4})$	16.6±0.1	16.4±0.1	-	16.4±0.1	-
Γ_{SXPL}				3.0±0.3	-
$A_{SXPL}(10^{-4})$				<0.1	2.9±0.5
Fe Kα Line E (keV)	6.43±0.02	6.43±0.02	-	6.43±0.02	-
.... $I_{\rm Fe}(10^{-5})$	1.0±0.2	0.8±0.2	0.9±0.2	1.0±0.2	1.2±0.2
.... σ (eV)	<80	<60	-	<60	-
.... EW (eV)	120±25	90±20	120±30	110±15	130±20
Fe Kβ Line E (keV)	$7.0^{+0.1}_{-0.4}$	7.03±0.04		7.02±0.04	
.... $I_{\rm Fe}10^{-5})$	0.25±0.15	<0.2	0.4±0.1	0.17±0.15	0.5±0.2
.... EW (eV)	30±20	<20	60±15	25±20	70±30
R	0.3±0.2	1.3±0.2	-	0.8±0.2	-
χ^2/dof	199/218	550/437	-	478/435	-

Note – Parameters from our best-fit models. The first column gives parameters to our best fit model of *Suzaku* data only consisting of a power law with Galactic absorption, an Fe Kα line and Compton reflection. The next column gives the results of fitting *Suzaku* and *XMM-Newton* data simultaneously with the basic model from the first column with Γ and overall normalization untied between the two observations. The next column shows the same data set but with Γ tied and a power law soft excess component with normalization untied between the two observations. A dash indicates a tied parameter.

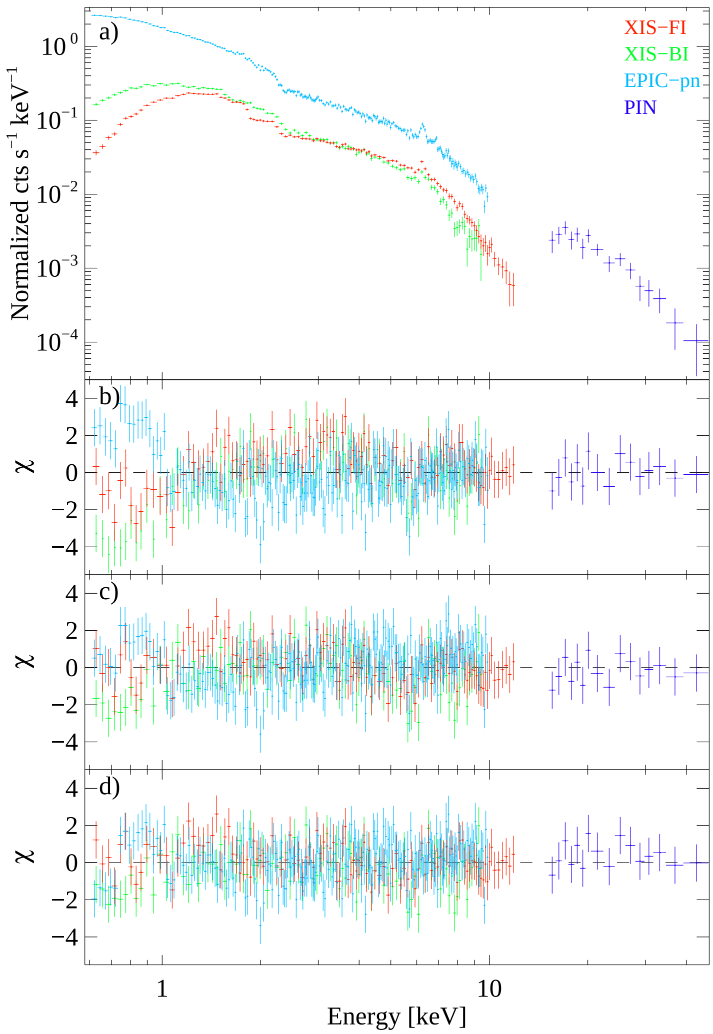

Figure 6.3: Fitting *Suzaku* and *XMM-Newton* data together. Panel a) shows data from the *Suzaku* XIS and PIN and from the EPIC-pn; b) shows residuals to our basic fit with no soft excess modeled and Γ tied between the two data sets; c) shows residuals to the basic model with Γ untied; d) shows residuals to the basic model plus a soft excess power law component (normalization untied).

(SAS), following the standard data reduction steps. The good exposure time after screening was 69 ks for the EPIC-pn. The radius of the source area was chosen to be 40 arcseconds and the background was extracted from the areas with no source photon contamination. We used the SAS tool `epatplot` to check for the presence of photon pile-up, finding none. While we have used more recent calibration files, model fitting resulted in values consistent with those of Longinotti et al. (2007). We found that the 2–10 keV flux of the source in 2004 was very similar to our 2011 observation (7.5×10^{-12} erg cm^{-2} s^{-1}). We therefore decided to try fitting the *XMM-Newton* and *Suzaku* data simultaneously. The combined data set and residuals to the models we applied are shown in Figure 6.3.

We applied our best fit "basic" model derived from the *Suzaku* spectrum (power law with Galactic absorption plus Compton hump and Fe lines, with no soft excess) to both spectra simultaneously, allowing for a free constant renormalization factor between the XIS and EPIC-pn, but otherwise keeping all spectral parameters (including Γ) tied. It was not significant to leave the Fe line normalization untied. This yielded a poor fit with χ^2/dof = 782/438 and confirmed that a spectral change had indeed taken place between the two observations. Residuals for this fit are shown in Figure 6.3b and a clear divergence can be seen between the two observations. We next untied the photon index between the two observations. This yielded an acceptable fit with χ^2/dof = 550/437. We also fit a model with the photon index tied as before, but including an additional power law to model the soft excess with its normalization free between the two observations. This yielded an improved fit with χ^2/dof = 478/435. Parameters for both of these fits are listed in Table 6.1. Results using a blackbody soft excess model were qualitatively similar with the blackbody temperature tied between the data sets yielding a best fit kT of 180$\pm$10 eV, a normalization for the EPIC-pn data of $(7.9\pm0.7)^{-6}$ corresponding to a luminosity of $(8\pm1)^{41}$ erg s^{-1} and for *Suzaku* an upper limit of 3^{-7} or blackbody luminosity of $L \leq 3 \times 10^{40}$ erg s^{-1}, as expected from previous fits.

6.1.2 Fe K Complex Analysis

Next we focused on the mid-X-ray range (4–10 keV) in order to examine the Fe complex in more detail, using only the XIS-FI data since it has the best sensitivity in this range. We began with the model from the broad fitting, freezing the continuum and Compton reflection parameters since these parameters are best determined from the broad fit. Note that the Fe edge at 7.11 keV is included in the PEXRAV model and that the depth was therefore a fixed quantity in these fits. We noticed residuals around 7 keV which could indicate the presence of an Fe XXVI emission line arising in highly ionized material or an Fe Kβ line arising in mostly neutral material. We added a Gaussian component with σ tied to that of the Fe Kα line and found a best fit energy centroid of $7.03^{+0.05}_{-0.12}$ keV and an intensity of $\leq 3.6^{-6}$ ph cm^{-2} s^{-1} or $\sim$40% of the Fe Kα line. The improvement in fit when adding this component was $\Delta\chi^2$/dof$= -6/3$, which is not a substantial improvement, however it is consistent with the presence of either Fe XXVI or a Kβ line. Adding an Fe Kβ line with energy frozen at 7.056 keV and intensity equal to 13% that of the Fe Kα line resulted in an upper limit to a Fe XXVI of 2.8×10^{-6} ph cm^{-2} s^{-1}. Testing for the additional presence of Fe XXV emission did not reveal a significant detection; the upper limit to the line intensity was 9^{-6} ph cm^{-2} s^{-1}. We tested for an additional broad Fe Kα line but found only an upper limit for the normalization of 4.4×10^{-6} ph cm^{-2} s^{-1} and an $EW \lesssim 70$ eV using the DISKLINE model in XSPEC with $R_{\rm in}$, and β as free parameters (however their values were poorly constrained by the fit since the normalization of the line was consistent with 0).

6.2 Results

The *Suzaku* spectrum of Mkn 590 shows many components typical to Seyferts, including a moderate photon index and a strong narrow Fe Kα line. We found an upper limit to the width of the Fe Kα line of $\sigma <$ 80 eV corresponding to a FWHM velocity of $v_{\rm FWHM} <$ 8900 km s^{-1}, assuming $\frac{3}{4}v^2_{\rm FWHM} = \langle v^2_{\rm disp}\rangle$ (Netzer 1990). Assuming Keplerian motion this corresponds to a distance of $\gtrsim$0.0026 pc or

3.1 lt days. This is consistent with results from Longinotti et al. (2007) who found a resolved Kα line with a FWHM velocity of 4000^{+2000}_{-2700} km s^{-1}. Both of these results are consistent with measurements of the Hα line width of 2000 km s^{-1} (Stirpe 1990), however it remains unclear if the Fe emission is associated with the BLR. We also measured a line at $\sim$7.0 keV which is likely Fe Kβ emission from neutral or at most moderately ionized Fe, however we cannot rule out a contribution from Fe XXVI.

We measured the strength of the Compton reflection component in this source, however the amount of reflection we measure is highly dependent on the model chosen. In the best fit to the *Suzaku* data we found a relatively low value for R, however residuals for the PIN data are consistently above the line in this fit. This could indicate that there is a stronger reflection component, but increasing the value manually leads to significant residuals between 5 and 10 keV in the XIS, particularly for the BI. Allowing the PIN normalization to be free reduced the value of R to $\leq$0.1 but with a normalization constant of 1.65 between the PIN and the XIS, much higher than calibration by the instrument team allows it should be. We conclude that it is likely the Compton reflection strength in this source is in the range R=0.2–1 based on the basic fit to the *Suzaku* data and the soft excess model fit to the combined data. A more sensitive hard X-ray detector or a longer integration time would be required to give more definitive results.

6.2.1 The Soft X-ray Conundrum

The flux of the source measured in January 2011 was very similar to the *XMM-Newton* measurement from 2004. Given the similarity in flux level for these two observations, we did not expect significant deviation in the spectral characteristics of the source. However it was clear that no soft excess was detected in the *Suzaku* data. If indeed a soft excess was detected in the *XMM-Newton* observation then it has weakened by at least a factor of $\sim$30 in seven years, while the 2–10 keV flux has remained relatively constant. If instead the *XMM-Newton* observation captured the source in a softer state, then Γ has hardened by ~ 0.10, a significant change given that the source is at a virtually identical flux level. Sobolewska &

Papadakis (2009) analyzed 9 Seyferts with longterm monitoring data from *RXTE*, and measured flux, observed Γ and in most cases Fe line EW. Their Figure 8 shows that on average a change in Γ of 0.1 in a particular source would be accompanied by a change in the 2–10 keV flux by a factor of 1.5–2. This is not to say that this source is not variable. Mkn 590 was monitored over the course of ∼1 year between 2000 and 2001 by *RXTE* which observed a range of 2–10 keV fluxes of 1–5 $^{-11}$ erg cm^{-2} s^{-1} (Markowitz & Edelson 2004). However *Swift*-BAT measured an average flux corresponding to F_{2-10} ∼6 $^{-12}$ erg cm^{-2} s^{-1} (Tueller et al. 2010), similar to both the *Suzaku* and *XMM-Newton* observations.

We have looked into the possibility of contamination by sources in the field of view such as from an ultra-luminous X-ray source (ULX) or background AGN. Longinotti et al. (2007) found two serendipitous sources in the *XMM-Newton* field of view but neither was close enough (each around 190") to contaminate either the *XMM-Newton* or *Suzaku* data. The 2004 *Chandra* ACIS data revealed a third source only 7" offset from Mkn 590, however the flux of this source was only 3 $^{-14}$ erg cm^{-2} s^{-1} in the 0.3–10 keV band or roughly 1.4 $^{-14}$ erg cm^{-2} s^{-1} in the 0.3–2 keV range. Longinotti et al. (2007) note that the source is at the same luminosity distance as Mkn 590 of 105 Mpc then this source would have a luminosity of $L_{0.3-10} \sim 4.3^{40}$ erg s^{-1}, consistent with a ULX at a distance of ∼3.6 kpc from the AGN. This is two orders of magnitude lower than the flux of the AGN and about fifty times lower than that of the soft component detected in the *XMM-Newton* data in the 0.3–2 keV range. It therefore seems most likely that the variability we have observed is intrinsic to the AGN and is simply an unexplained facet of the soft excess.

A weakening or strengthening of the soft excess has been seen in other AGN, however in most cases it also involved a change in flux state. For example, Markowitz & Reeves (2009) reported that NGC 4593 had a soft excess that weakened by a factor of 20 between an *XMM-Newton* observation and a *Suzaku* observation 5 years later which caught the source in a low hard X-ray flux state. However, it has been observed that variations in the soft excess can be independent of those in the hard power-law (e.g., Edelson et al. 2002), suggesting the possibility of independent physical mechanisms at work. We can rule out blurred reflection from an ionized medium (such as the REFLION model from Ross & Fabian 2005) as a source of the soft excess in this case since our *Suzaku* data clearly show reflection but no soft excess. A simple blackbody soft excess component provides a good fit to the *XMM-Newton* data, however this model has been shown to clash with theoretical predictions for disk temperatures (e.g. Gierliński & Done 2006).

A recent *XMM-Newton* monitoring campaign of Mkn 509 by Mehdipour et al. (2011) revealed a variable soft excess that correlated with the optical-UV flux but not with the flux of the 2–10 keV power law flux. Medhipour et al. (2011) were able to successfully apply models describing the soft excess as being produced by thermal Comptonization by a warm (0.2 keV) optically thick ($\tau \sim 17$) corona surrounding the inner regions of the disc. This is an important result that may reveal a long sought-after link between the X-ray spectral properties of a source and the optical/UV thermal accretion disk emission and could explain the extreme behavior in Mkn 590. If a soft excess was present in the past and has recently vanished, then we would expect to see a significant drop in the UV flux of this source if this link exists. Unfortunately there was no optical/UV observation simultaneous with the *Suzaku* observation. Future monitoring of this source with simultaneous UV and X-ray instruments would be required to confirm or exclude this hypothesis.

Further monitoring would also add to the small but growing number of observations tracking variations in the soft excess that are independent of variations displayed by the hard X-ray coronal power law. Mehdipour et al. (2011) found a variability range of 1–1.7^{44} erg s^{-1} for Mkn 509 over the course of 36 days. Mkn 590 and NGC 4593 have both shown much larger changes, factors of 20–50, on a scale of years. Turner et al. (2001) reported a decrease by a factor of nearly 3 in the soft excess of the NLSy1 Ark 564 across a 35-day *ASCA* campaign. During this time the hard power-law varied strongly on timescales of hours but on average varied by a factor of only 1.7 across the whole campaign. Edelson et al. (2002) noted a qualitatively similar trend for the NLSy1 Ton S180 with systematic trends on timescales of days–weeks in the soft band independent of variations exhibited above 2 keV. It should be noted that since both Ark 564 and Ton S180 are narrow line Seyferts they are likely in a different luminosity regime (relative to Eddington) and may be experiencing different physical processes, particularly with regards to the Compton up-scattered component of the soft excess (Done et al. 2012) and direct comparison with these objects should be done with caution. Nevertheless, understanding how the soft excess varies over a range of timescales could help pin down the source of this feature. Further investigations which calculate the variability amplitude on multiple timescales would be greatly beneficial, but would require sustained spectral monitoring with instruments sensitive enough in the soft band to give precise measurements of the soft excess luminosity.

6.3 Acknowledgements

Chapter 6, in full, is a reproduction of material as it appears in the Astrophysical Journal 2012, Rivers, Markowitz & Rothschild, ApJ, 2012.

7 Summary of Results

AGN have been studied closely for many decades, but their environments, evolution and even many of the physical processes that produce the high-energy photons in these objects are not yet fully understood. I have endeavored to understand aspects of AGN geometry and high energy emission processes through X-ray spectral investigations. Taking advantage of the broad bandpass and large quantity of data in the *RXTE* archive I constructed two samples of AGN for investigation into the prevalence of high energy rollovers and Compton reflection humps, and into properties of the different classes of AGN. I have supplemented this work with observations of individual objects which has allowed me to perform more intense investigations into properties of the location, geometry and nature of circumnuclear material in these objects.

7.1 Individual Objects

7.1.1 The Clumpy Absorber in Cen A

A sustained monitoring campaign by *RXTE* observed an occultation event in Cen A in detail from ingress to egress. A discrete clump of material, likely associated with a clumpy torus, transited the line of sight to the central illuminating source for 170 days between 2010 August and 2011 February with a maximum increase in $N_{\rm H}$ of 8.4 $\times 10^{22}\,{\rm cm}^{-2}$. Assuming the clump of material was roughly spherical with a linear density profile and assuming a distance from the central nucleus of 0.1–0.3 pc (from infrared measurements) we found that the clump had a linear dimension of 1.4–2.4 $\times 10^{15}$ cm with a central number density of $n_{\rm H}$ = 1.8–

$3.0 \times 10^7\,\mathrm{cm}^{-3}$, in good agreement with previous results. Two occultation events seen in ~ 10 years indicate that clumps of material are indeed transiting our line of sight and evidence suggests that they are part of a clumpy, Compton-thin torus, the characteristics of which are consistent with the model proposed by Nenkova et al. (2008a; 2008b).

7.1.2 The Circumnuclear Material in MCG–2-58-22

A long-look *Suzaku* observation of MCG –2-58-22 confirmed that it is extremely unabsorbed in the X-ray band (an upper limit of 2.5×10^{20} cm^{-2} in excess of the Galactic column), despite significant reddening seen in the optical band and lack of substantial optical broad lines (MCG –2-58-22 is a Seyfert 1.5). These results led the conclusion that while no absorbers are in the line of sight to the central region of the AGN, it is possible that clumps of material may be obscuring lines of sight to the region(s) where the optical line emission is produced.

The excellent resolution of the XIS CCDs around $\sim$ 5–7 keV gave a detailed picture the Fe K complex. A narrow ($v_{\mathrm{FWHM}} < 7100$ km s^{-1}) Fe Kα emission line constrained the locating of the emitting material to much further out than has been done with previous observations. No significant broad Fe line was detected, such as would be expected from the inner portions of a radiatively efficient accretion disk. Since there is such a clean line of sight to the nucleus, this region cannot be simply obscured or out of the line of sight, implying that the inner disk may be truncated or radiatively inefficient. From the limits on the Fe line v_{FWHM} I have calculated a minimum inner radius of $\gtrsim 1200\ R_{\mathrm{S}}$. Comparing the Fe line EW to the CRH strength indicated that both components likely arise in the same Compton-thick material without any contribution from additional Compton-thin circumnuclear material. A disk/slab geometry (PEXRAV) for the Compton-thick material gave a reflection strength $R = 0.69 \pm 0.05$ with a photon index of $\Gamma = 1.80 \pm 0.02$.

I successfully applied the new MYTORUS model for Compton reflection to MCG –2-58-22, which assumes that the reflecting material is in the form of a torus of uniform density rather than in the form of a flat disk, as has typically been done with more established models, such as PEXRAV. I attempted to apply the MY-

Torus model to our *RXTE* sample, but the model's assumption that the torus has a uniform density leads to a steep change in the line-of-sight absorption at the edge of the donut-shaped torus, causing all Compton-thin sources to have inclination angles close to 60° (the opening angle assumed in the model). Most sources also required additional Fe line emission from Compton-thin material. For the majority of our sources this led to two parameters, angle and torus density, characterizing only one measurable quantity, the flux of the CRH, leading to degeneracy between these two physical quantities.

7.1.3 The Disappearing Soft Excess in Mkn 590

I analyzed a long-look *Suzaku* observation of the Seyfert 1.2 Mkn 590 with the aim of measuring the Compton reflection strength, Fe K complex properties, and soft excess emission which had been observed previously in this source. The Compton reflection strength was measured to be in the range 0.2–1.0 depending on the model used. A moderately strong Fe Kα emission line was detected with an equivalent width of $\sim$ 120 eV and an Fe Kβ line was identified with an equivalent width of $\sim$ 30 eV, although contribution from ionized Fe emission at this energy could not be ruled out. Surprisingly, there was no evidence for soft excess emission. Comparing these results with a 2004 observation from *XMM-Newton*, we found that either the soft excess has decreased by a factor of 20–30 in 7 years or else the photon index has steepened by 0.10 (with no soft excess present), while the continuum flux in the range 2–10 keV has varied only minimally (10%). This result could support recent claims that the soft excess is independent of the hard X-ray continuum.

7.2 The Archival Surveys

I have analyzed data for all AGN in the *Rossi X-ray Timing Experiment* (*RXTE*) archive in order to explore the geometry of circumnuclear material around SMBHs and characterize their X-ray spectra. Two surveys, one broad band survey with 23 AGN and one full spectral survey with 100 AGN, improve upon previous surveys of the hard X-ray energy band in terms of accuracy and sensitivity, particularly with respect to confirming and quantifying the amount of Compton-reflection in these sources. Thanks to the combination of the longevity of the *RXTE* mission, the sustained monitoring campaigns on many AGN, and the simultaneous operation of the PCA and HEXTE instruments in the 3–200 keV energy range, broadband X-ray spectra with long integration times, high sensitivity, and moderately good spectral resolution were obtained. Although the HEXTE instrument is sometimes overlooked due to its low sensitivity on short timescales, this work has demonstrated that HEXTE can indeed yield spectra out to at least 100 keV for 23 AGN with a sufficient combination of brightness and exposure time and out to at least 50 keV for an additional 18 sources. The fact that many of the spectra presented here are long-term averaged spectra means the ambiguity inherent in single-epoch spectral fitting caused by variability of the source is eliminated. These spectra may serve as baselines for future missions and can be combined with broadband data to create SEDs for future analysis. With information about abundances of the different types of AGN and X-ray luminosity functions, the stacked spectra could be combined to find the AGN contribution to the CXB. Average spectral parameters and distributions within different types of Seyferts could also be used to fine-tune current CXB models.

Long-term averaged values for Γ were generally consistent with previous results for individual objects; averages by AGN classification were also consistent with previous surveys. Unsurprisingly, I found that the Fe line complex was necessary to model in all Seyfert spectra. Using a single gaussian to model this component I found typical equivalent widths around 100–200 eV, roughly consistent with previous results. There was tentative evidence for high-energy rollovers in the spectra of only three objects, Circinus, NGC 4945, and MR 2251–178, while for the remaining objects no rollover below 200 keV was indicated.

Roughly 85% of Seyferts in both samples showed significant contribution from the CRH. Comparing the strength of the CRH with the amount of Fe emission seen, allowed me to estimate the ratio of Compton-thick to Compton-thin material in AGN, with the average being around 40%, though there was large object to object variation.

There was no significant correlation between Γ and L for the Seyferts in the full sample, however a positive correlation between Γ and L for blazars was in agreement with the Fossati sequence and the luminosity dependence of the broad band SED hump peak energies. The BL Lac objects tended to have higher values of Γ than the FSRQs (averages of 2.3 and 1.8, respectively) as expected since FSRQs tend to be brighter and have lower peak frequencies. This is consistent with inverse Compton emission processes where higher fluxes of scattered photons cool the Comptonizing electrons.

7.3 Conclusion

The paradigm of AGN unification has been shifting slowly over the past two decades. The models proposed by Antonucci & Miller (1985), and iconically illustrated by Urry & Padovani (1995), have been tested, modified, and refined. What remains firmly intact is the central engine of AGN emission: an accretion disk surrounding a supermassive black hole with the addition of large-scale jet emission orthogonal to the disk in the case of blazars and other radio-loud AGN.

The similar distributions of Γ for type 1 and 2 Seyferts in the full *RXTE* sample supports the idea that they are intrinsically the same. However, the distribution of CRH strengths showed no difference between types 1 and 2, which we would expect under classical unification schemes with reflection off a disk and obscuration by a torus, where inclination angle is the primary difference between the two types. This does not conclusively prove that all of the reflection is arising in the torus, but is strongly indicative that not all the reflection arises in the accretion disk. The NLSy1's in the full sample showed significantly higher photon indices than the normal Seyfert 1's. Two of the Seyfert 2's in the sample had very soft X-ray spectra, similar to NLSy1's and could be in a similar accretion regime. This is also consistent with a common central engine for all Seyferts, but with the differences between types being dependent on accretion rate and the geometry of the circumnuclear material, as well as viewing angle.

The broad range of the brightest 23 *RXTE* AGN was necessary to test for the presence of rollovers in the continuum, however only one source clearly required a rollover. Spectroscopy up to 100 keV was sufficient to constrain the rollover in Seyferts to $\gtrsim$225 keV in 20 out of 23 sources, corresponding to an electron temperature of $k_B T_e \gtrsim 75$ keV for the corona surrounding the disk, the putative source of the high energy photons. Rollovers below 200 keV seem to be much rarer than expected from previous work (e.g., Perola et al. 2002) and true broad band SEDs stretching into the MeV range will be needed to search for rollovers at these higher energies. Once we find the rollovers in AGN we can begin to test Comptonization models for the corona as is done in GBH spectra. Results for the blazars in the full sample were consistent with the Fossati sequence and support models of blazar high energy emission as inverse Comptonization processes.

The biggest changes to the iconic picture have occurred as our knowledge of the torus structure has grown. It seems clear that the torus can be characterized as clumpy in at least some cases, supported by strong evidence from infrared observations and our own observations of clumps of distant material occulting the central illuminating source in Cen A. Additionally, we have shown that overly simplistic Compton reflection hump models such as a flat disk or uniform doughnut need to be replaced by more detailed models that portray the characteristics of matter in the environment of SMBHs in a more realistic fashion. From our *RXTE* samples we found that $\sim$85% of Seyferts showed a significant CRH, and that an average of 40% of the Fe Kα line flux arises in reflection off Compton-thick material. This implies that, while Compton-thick material is commonly found in the vicinity of the black hole, a significant amount of Compton-thin material is also common and must be taken into account when modeling the Fe line self-consistently with the CRH. More complex models of the CRH and sensitive hard X-ray spectrometers are needed to progress further in our understanding of the geometry of the Compton-thick circumnuclear material.

The soft excess remains something of a mystery, not yet fully integrated into our picture of AGN. It may be blurred fluorescent lines from reflection off ionized Compton-thick material in the vicinity of the black hole. Alternatively, it may come from absorption by partially ionized disk winds where the velocity of the winds causes the smearing of the lines. If it can be shown that it varies with UV emission (as seen by Mehdipour et al. 2011) in multiple cases then we must accept that it may be the high energy tail of optical-UV disk emission. Simultaneous monitoring with UV and X-ray instruments for several sources could confirm or reject this hypothesis.

Overall, my results are consistent with the picture of all AGN sharing a common engine. The differences in observed properties between the classes of AGN are likely based on mass, accretion rate, the presence and beaming angle of jets, and the geometry of the circumnuclear material. I conclude that the unified picture of AGN remains intact, but a more complex reflecting geometry such as a combined disk and (possibly clumpy) torus is likely a more accurate picture of the Compton-thick material and we should work toward using more realistic models.

7.4 Acknowledgements

Chapter 7, in part, has been submitted for publication to the Astrophysical Journal 2012, Rivers, Markowitz & Rothschild. The dissertation author was the primary investigator and author of this material.

References

[1] Abdo, A.A., et al. 2010, ApJ, 716, 30

[2] Akiyama, M., Ueda, Y., Ohta, K., Takahashi, T., & Yamada, T., 2003, ApJS, 148 275

[3] Alexander, D.M., Hough, J.H., Young, S., Bailey, J.A., Heisier, C.A., Lumsden, S.L., & Robinson, A., 1999, MNRAS, 303,17

[4] Anders, E. & Grevesse, N., 1989, Geochimica et Cosmochimica Acta 53, 197

[5] Arnaud, K. 1996, in *Astronomical Data Analysis Software and Systems*, Jacoby, G., Barnes, J., eds., ASP Conf. Series Vol. 101, p.17

[6] Antonucci, R.R.J. & Miller, J.S., 1985, ApJ, 297, 621

[7] Antonucci R., 1993, ARA&A, 31, 473

[8] Bian, W. & Zhao, Y., 2003, MNRAS, 343, 164

[9] Bianchi, S., Matt., G., Balestra, I., Guainazzi, M.& Perola, G.C. 2004, A&A, 422, 65

[10] Bianchi, S. et al. 2005, MNRAS, 357, 599

[11] Bird, A.J., et al., 2007, ApJS, 170, 175

[12] Blustin, A.J., et al., 2007, A&A, 466, 107

[13] Boldt, E., 1987, Proc. IAU Symp. 124, Observational Cosmology (Dordrecht: Reidel), 611

[14] Cappellari, M., Neumayer, N., Reunanen, J., van der Werf, P. P., de Zeeuw, P. T., & Rix, H.-W. 2009, MNRAS, 394, 660 Crummy, J., Fabian, A.C., Gallo, L., Ross, R. R., 2006, MNRAS, 365, 1067

[15] Dadina, M. 2007, A&A, 461, 1209

[16] Dapp, W.B. & Basu, S., 2009, MNRAS, 395, 1092

[17] de la Calle Pérez, I. et al. 2010, A&A, 524, 50

[18] Donato, D., Ghisellini, G., Tagliaferri, G., & Fossati, G. 2001, A&A, 375, 739

[19] Done, C., Davis, S.W., Jin, C., Blaes, O. & Ward, M. 2012, MNRAS, 420, 1848

[20] Edelson, R. & Nandra, K. 1999, ApJ, 514, 682

[21] Edelson, R., Turner, T.J., Pounds, K., Vaughan, S., Markowitz, A., Marshall, H., Dobbie, P. & Warwick, R. 2002, ApJ, 568, 610

[22] Elitzur, M. & Shlosman, I. 2006, ApJ, 648, L101

[23] Elvis, M., et al. 1994, ApJS, 95, 1

[24] Evans, D.A., Kraft, R.P., Worrall, D.M., Hardcastle, M.J., Jones, C., Forman, W.R., & Murray, S.S. 2004, ApJ, 612, 786

[25] Fabian, A.C., Rees, M.J., Stella, L., White, N.E., 1989, MNRAS, 238, 729

[26] Fossati, G., Maraschi, L., Celotti, A., Comastri, A., & Ghisellini, G. 1998, MNRAS, 299, 433

[27] Fowler, W.A. & Hoyle, F. 1963, RGOB, 67, 301

[28] Frontera, F., et al. 2001, ApJ, 546, 1027

[29] Fukazawa, Y., et al. 2009, PASJ, 61, 17

[30] George, I.M. & Fabian, A.C. 1991, MNRAS, 249, 352

[31] Ghosh, K.K. & Soundararajaperumal, S., 1992, ApJ, 398, 501

[32] Giebels, B., et al., 2002, ApJ, 571, 763

[33] Gierliński, M. & Done, C. 2006, MNRAS, 371, L16

[34] Gilli, R., Comastri, A. & Hasinger, G. 2007, A&A, 463, 79

[35] Gondek, D., et al. 1996, MNRAS, 282, 646

[36] Grandi, P., Guainazzi, M., Mineo, T., et al., 1997, A&A, 325, L17

[37] Gruber, D.E., Blanco, P.R., Heindl, W.A., Pelling, M.R., Rothschild, R.E., & Hink, P.L., 1996 A&AS, 120C, 641

[38] Grupe, D., Beuermann, K., Mannheim, K., & Thomas, H.-C., 1999, A&A, 350, 805

[39] Guainazzi et al. 1998, MNRAS, 301, 1

[40] Haardt, F., Maraschi, L. & Ghisellini, G., 1994, ApJ, 432, 95

[41] Ho, L.C., Filippenko, A.V., Sargent, W.L.W., & Peng, C.Y. 1997, ApJS, 112, 391

[42] Itoh, T., et al., 2008, PASJ, 60S, 251

[43] Jahoda, K., Markwardt, C.B., Radeva, Y., Rots, A.H., Stark, M.J., Swank, J.H., Strohmayer, T.E., & Zhang, W., 2006, ApJS, 163, 401

[44] Jorstad, S.G., et al., 2010, ApJ, 715, 362

[45] Kalberla, P.M.W., Burton, W.B., Hartmann, Dap, Arnal, E.M., Bajaja, E., Morras, R., & Pöppel, W.G.L., 2005, A&A, 440, 775

[46] Kalemci, E., Tomsick, J.A., Buxton, M.M., Rothschild, R.E., Pottschmidt, K., Corbel, S., Brocksopp, C., & Kaaret, P., 2005, ApJ, 622, 508

[47] Kataoka, J., Tanihata, C., Kawai, N., Takahara, F., Takahashi, T., Edwards, P.G. & Makino, F. 2002, MNRAS, 336, 932

[48] Kembhavi, A.K. & Narlikar, J.V., 1999, *Quasars and Active Galactic Nuclei; An Introduction*, Cambridge University Press, Cambridge, U.K

[49] Khachikian, E.Y. & Weedman, D.W., 1974, ApJ, 192, 581

[50] Kollatschny, M.Z. & Dietrich, M., A&A, 454, 459

[51] Koyama, K. et al. 2007, PASJ, 59, 23

[52] Lamer, G., Uttley, P. & M^{c}Hardy, I.M. 2003, MNRAS, 342, L41

[53] Lira P., Ward M.J., Zezas, A., & Murray, S.S. 2002, MNRAS, 333, 709

[54] Longinotti, A.L. et al. 2007, A&A, 470, 73

[55] Madejski, G., Życki, P., Done, C., Valinia, A., Blanco, P., Rothschild, R.E. & Turke, B. 2000, ApJ, 535, L87

[56] Maiolino, R., Risaliti, G., Salvati, M., Pietrini, P., Torricelli-Ciamponi, G., Elvis, M., Fabbiano, G., Braito, V., & Reeves, J., 2010, A&A, 517, 47

[57] Magdziarz, P. & Zdziarski, A., 1995, MNRAS, 273, 837

[58] Marconi, A., Risaliti, G., Gilli, R., Hunt, L. K., Maiolino, R., & Salvati, M. 2004, MNRAS, 351, 169

[59] Markoff, S., et al. 2005, ApJ, 635, 1203

[60] Markowitz, A. & Edelson, R. 2004, ApJ, 617, 939

[61] Markowitz, A. & Reeves, J.N. 2009, ApJ, 705, 496

[62] Matt, G., 2002, MNRAS, 337, 147

[63] McKernan, B. & Yaqoob, T. 1998, ApJL, 501, 29

[64] McKernan, B., Yaqoob, T. & Reynolds, C.S. 2007, MNRAS, 379, 1359

[65] Mehdipour, M. et al. 2011, A&A, 534A, 39

[66] Meisenheimer, K. et al. 2007, A&A, 471, 453

[67] Merloni, A., Heinz, S., & di Matteo, T. 2003, MNRAS, 345, 1057

[68] Mitsuda, K., et al. 2007, PASJ, 59, 1

[69] Murphy, K.D. & Yaqoob, T. 2009, MNRAS, 397, 1549

[70] Nandra, K. 2006, MNRAS, 368, 62

[71] Nandra, K., O'Neill, P.M., George, I.M. & Reeves, J.N., 2007, MNRAS, 382, 194

[72] Nandra, K. & Pounds, K. A., 1994, MNRAS, 268, 405

[73] Nenkova, M., Sirocky, M. M., Ivezić, Ž, & Elitzur, M. 2008a, ApJ, 685, 147

[74] Nenkova, M., Sirocky, M., Nikutta, R., Ivezić, Ž., & Elitzur, M. 2008b, ApJ, 685, 160

[75] Netzer, H. 1990, in Active Galactic Nuclei, Saas-Fee Advanced Course 20, ed. T. J.-L. Courvoisier & M. Major (Berlin : Springer), 57

[76] Netzer, H. et al. 2003, ApJ, 599, 933

[77] Neumayer, N., Cappellari, M., van der Wert, P., Reunanen, J., Rix, H.-W., de Zeeuw, T., & Davies, R. 2010, The Messenger, 139, 36

[78] Osterbrock, D. E., 1977, ApJ, 215, 733

[79] Osterbrock, D. E., 1989, *Astrophysics of Gaseous Nebulae and Active Galactic Nuclei*, (Mill Valley, CA: Univ. Science Books)

[80] Patrick, A.R., Reeves, J.N., Porquet, D., Markowitz, A.G., Braito, V. & Lobban, A.P., MNRAS, 426, 2522

[81] Peterson, B.M., 1997, *An Introduction to Active Galactic Nuclei*, Cambridge University Press, Cambridge, U.K

[82] Perola, G.C., Matt, G., Cappi, M., Fiore, F., Guainazzi, M., Maraschi, L., Petrucci, P.-O. & Piro, L., 2002, A&A, 389, 902

[83] Pounds, K., Done, C., & Osborne, J.P. 1995, MNRAS, 277, 5

[84] Pounds, K.A., King, A.R., Page, K.L., O'Brien, P.T. 2003, MNRAS, 346, 1025

[85] Poutanen, J. & Svensson, R. 1996, ApJ, 470, 249

[86] Predehl, P. & Schmitt, J.H.M.M., 1995, A&A, 293, 889

[87] Ramos Almeida, C., et al. 2011, ApJ, 731, 92

[88] Reeves, J.N., Nandra, K., George, I.M., Pounds, K.A., Turner, T.J. & Yaqoob, T. 2004, ApJ, 602, 648

[89] Reeves, J.N., et al. 2007, PASJ, 59S, 301

[90] Reynolds, C.S., 1997, MNRAS, 286, 513

[91] Ricci, C., Walter, R., Courvoisier, T.J.-L. & Paltani, S. 2011, A&A, 532, 102

[92] Risaliti, G. et al. 2009, MNRAS, 393, L1

[93] Rivers, E., Markowitz, A., Duro, R., & Rothschild, R., ApJ, 2012, 759, 63

[94] Rivers, E., Markowitz, A. & Rothschild, R., 2011a, ApJS 193, 3

[95] Rivers, E., Markowitz, A. & Rothschild, R., 2011b, ApJ, 732, 36

[96] Rivers, E., Markowitz, A. & Rothschild, R., 2011c, ApJ, 742, L29

[97] Rothschild, R., Markowitz, A., Rivers, E., Suchy, S., Pottschmidt, K., Kadler, M., Müller, C., & Wilms, J. 2011, ApJ, 733, 23

[98] Rothschild, R.E., et al. 1998, ApJ, 496, 538

[99] Ross, R.R. & Fabian, A.C., 2005, MNRAS, 358, 211

[100] Sako, M., Kahn, S.M., Paerels, F., & Liedahl, D.A. 2000, ApJ, 543, 115

[101] Schurch N.J., Warwick, R.S., Griffiths, R.E., Sembay, S., Ptak, A.F., 2003, MNRAS, 345, 423

[102] Sobolewska, M.A., & Papadakis, I.E., 2009, MNRAS, 339, 1597

[103] Steenbrugge, K.C., et al. 2003, A&A, 408, 921

[104] Steenbrugge, K.C., et al. 2005, A&A, 434, 569

[105] Stirpe, G.M., 1990, A&AS, 85, 1049

[106] Strüder, L. et al. 2001, A&A, 365, 18

[107] Suchy, S., et al. 2011, ApJ, 733, 15

[108] Takahashi, T., et al. 2007, PASJ, 59, 35

[109] Takahashi, H., et al., 2008, PASJ, 60S, 69

[110] Titarchuk, L., 1994, ApJ, 434, 570

[111] Tueller, J., et al., 2010, ApJS, 186, 378

[112] Tueller, J., Mushotzky, R.F., Barthelmy, S., et al. 2008, ApJ, 681, 113

[113] Turner, T.J., Kraemer, S.B., George, I.M., Reeves, J.N. & Bottorff, M.C. 2005, ApJ, 618, 155

[114] Turner, T.J., Reeves, J.N., Kraemer, S.B. & Miller, L. 2008, A&A, 483, 161

[115] Turner, T.J., Romano, P., George, I.M., Edelson, R., Collier, S., Mathur, S., & Peterson, B.M., 2001, ApJ, 561, 131

[116] Urry, C.M., 1998, Advances in Space Research, Volume 21, 89

[117] Urry, C.M. & Padovani, P., 1995, PASP, 107, 803

[118] Vaughan, S. et al. 2004, MNRAS, 351, 193

[119] Vaughan, S., Edelson, R., Warwick, R.S., Malkan, M.A., & Goad, M.R., 2001, MNRAS, 327, 673

[120] Verner, D. A., Ferland, G. J., Korista, K. T., & Yakovlev, D. G. 1996, ApJS, 465, 487

[121] Vestergaard, M. & Peterson, B. 2006, ApJ, 641, 689

[122] Weaver, K.A., Gelbord, J. & Yaqoob, T., 2001, ApJ, 550, 261

[123] Weaver, K.A., Nousek, J., Yaqoob, T., Hayashida, K., & Murakami, S. 1995, ApJ, 451, 147

[124] Weedman, D.W. 1976, ApJ, 208, 30

[125] Whysong, D., & Antonucci, R. 2004, ApJ, 602, 116

[126] Wilms, J., Allen, A., & McCray, M. 2000, ApJ 542, 914

[127] Wilms, J., Nowak, M.A., Pottschmidt, K., Pooley, G.G., & Fritz, S., 2006, A&A, 447, 245

[128] Winkler, H., 1992, MNRAS, 257, 677

[129] Winter, L.M., Lewis, K.T., Koss, M., Veilleux, S., Keeney, B., & Mushotzky, R.R., 2010, ApJ, 710, 503

[130] Winter, L.M., Mushotzky, R.F., Reynolds, C.S., & Tueller, J. 2009, ApJ, 690, 1322

[131] Yamaoka, K., Uzawa, M., Arai, M., Yamazaki, T., & Yoshida, A. 2005, ChJAS, 5, 273

[132] Yaqoob, T. & Padmanabhan, U. 2004, ApJ, 604, 63

[133] Zdziarski, A.A., Poutanen, J. & Johnson, W.N. 2000, ApJ, 542, 703